ABSTRACT

Title of Document: INTENSE TERAHERTZ GENERATION VIA TWO-COLOR LASER FILAMENTATION

Taek Il Oh, Doctor of Philosophy, 2013

Directed By: Professor Kiyong Kim
Institute for Research in Electronics and Applied Physics

The main focus of this dissertation is intense terahertz (THz) generation using two-color laser mixing in air plasma. In this scheme, the fundamental and second harmonic of an ultrashort pulsed laser are combined and focused into air to create a gaseous plasma, which produces an intense THz pulse in the far field. To understand the generation process, we have developed a two-dimensional (2-D) plasma current model. Using this model, we have simulated the conditions for optimal THz generation and verified them experimentally. A full control of THz output is demonstrated by varying the phases and polarization states of the input laser pulses.

We have studied how the generated THz energy scales with various focal lengths and input laser energies up to 60 mJ. For high enough energy inputs, the resulting THz saturates. This arises from inefficient laser energy coupling into the plasma, which results from plasma-induced laser defocusing in filamentation. We have overcome the saturation effect by elongating the filaments and achieved 7 μJ of

THz energy with 60 mJ laser energy. This provides a conversion efficiency of 10^{-4} from optical to THz energy.

In addition, we have investigated high-power THz generation in two-color laser filamentation with terawatt (TW) lasers including a 0.5 TW, 1 kHz repetition (rep) rate system, as well as, 2 TW and 30 TW systems, both operating at 10 Hz rep rate. In particular, our 1 kHz rep rate THz source can provide high-energy (>1 μJ), high-average power (>1 mW), intense (>1 MV/cm), and broadband (0.01~60 THz) THz radiation via two-color filamentation in air. Based on our observed scaling law, a ~30 TW laser can produce >0.1 mJ of THz radiation with multi-gigawatt (GW) peak power in ~1.5 m long filamentation.

We have also studied various THz detection methods covering a broad range of THz frequency bands. We observe our THz source produces extremely broad electromagnetic (EM) radiation ranging from radio-micro waves to infrared frequencies, confirmed by our complementary THz detection methods. This source could be a useful tool for broadband linear and nonlinear THz spectroscopy.

INTENSE TERAHERTZ GENERATION VIA TWO-COLOR LASER FILAMENTATION

By

Taek Il Oh

Dissertation submitted to the Faculty of the Graduate School of the
University of Maryland, College Park, in partial fulfillment
of the requirements for the degree of
[Doctor of Philosophy]
[2013]

Advisory Committee:
Professor Howard M. Milchberg, Chair
Professor Kiyong Kim, Co-chair
Professor Thomas M. Antonsen, Jr.
Professor Edo Waks
Professor Ichiro Takeuchi

Dedication

This work is dedicated to my wife, Hyejin, and our daughters, Yoona and Suah.

Acknowledgements

First, I would like to give special thanks to my advisor, Prof. Kiyong Kim. This dissertation work would not be possible without his mentorship. He has trained and guided me with many research skills and ideas and also provided a wonderful research environment throughout my Ph.D. years. It has been my pleasure to work with him.

Prof. Howard Milchberg deserves acknowledgment for his insight and efforts in our collaboration. In addition, as a co-advisor, he has also guided me through the completion of this work as well as provided much administrative assistance.

I would also like to express my gratitude to my co-workers, especially Yong Sing, Yungjun, Jeff, Vijay, Dongkyu, and Dongwen, and also our previous lab members, Dr. Jane Lee, Inhyuk Nam, and Dongyoul Lee for helpful discussions and comments in many experiments, and Eric and Nihal for their contributions in operating their high power laser system.

Finally, I want to mention all my loving family here. Without their care, sacrifice, and understanding, I couldn't finish this dissertation successfully. Special thanks to my wife, Hyejin, and our daughters, Yoona and Suah. I also am very grateful to my parents, parents in law, and my brother, Chaeseok Oh, Youngsoon Kwak, Eunsook Lee, Youngdon Kwon, Taekseung Oh, and Younghee Jung.

Table of Contents

List of Tables

List of Figures

Chapter 1 : Introduction and overview

1.1 Introduction to high power laser systems

Since the first Ruby laser was demonstrated by Maiman at Hughes Research Laboratories in 1960 [1], the rapid progress on lasers has provided incredible benefits to scientific research and industrial areas. We continue to discover how surprisingly small and powerful lasers can be. On a daily basis, many of us are using very compact lasers such as diode lasers in DVD/CD players and laser pointers. As a laser spans from millimeter-size to football field size like the National Ignition Facility, the laser power varies from ~1 mW to 100 kW in continuous wave (CW). When we include pulsed lasers, it can provide much higher peak power.

Surprisingly, over the last several decades, the record peak power has increased by more than ten orders of magnitude [2]. Starting from free running CW lasers, the Q-switching, mode-locking and chirped pulse amplification (CPA) techniques have made huge breakthroughs in increasing laser peak power [3]. In parallel, broadband gain media have been studied and applied for mode-locking and CPA techniques. For example, titanium-doped sapphire (Ti:sapphire) crystals, researched by Moulton as a gain medium at 660 - 986 nm have been utilized as a main driver in femtosecond (1 fs = 10^{-15} s) laser development [4].

Such progress has led to achieving petawatt (10^{15} W) scale laser power in various laboratories around the world [5]. And now even many university laboratories have tabletop-size terawatt (1 TW= 10^{12} W) or sub-TW laser systems which can

provide extremely strong electric fields, far exceeding the atomic Coulomb field seen by electrons in the ground state of atoms. For instance, laser intensities of 3×10^{16} W/cm^2 routinely achieved by sub-TW laser pulses focused within tens of micrometers can provide ~5×10^9 V/cm. Nowadays such laser intensities ($10^{16} \sim 10^{18}$ W/cm^2) are readily obtained with compact tabletop laser systems.

As a result of the laser development, many new scientific areas of discovery are now open to us—ultrafast optical science, attosecond science, laser fusion, direct laser acceleration, and laser-based THz science which is of interest in this dissertation.

1.2 Introduction to terahertz (THz) science

1.2.1 THz science

Terahertz (1 THz = 10^{12} Hz) science is a study of electromagnetic radiation covering the region of the spectrum between infrared and microwave: typically, 30 μm ~ 3 mm in wavelength or 0.1 ~ 10 THz in frequency as shown in Fig. 1.1. For instance, 1 THz corresponds to 300 μm in wavelength, 4.1 meV in photon energy, and 1 picosecond (1 ps = 1×10^{-12} s) in period. Traditionally, THz is known as too high frequency to be generated by solid-state devices; the wavelength is too long for any thermal devices to emit the radiation effectively. Because of this lack of adequate THz sources, this region has been dubbed as the THz gap [6] [7]. To resolve this, there have been two approaches for practical THz generation, up-conversion and down-conversion. In the microwave communities, efforts have been made to up-convert the frequency from multi-GHz to THz. On the other hand, photonics scientists have been struggled with achieving THz frequencies by down-conversion for many decades.

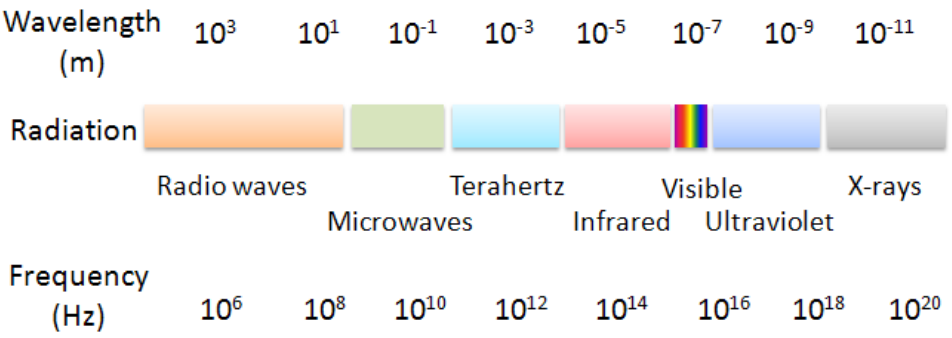

Figure 1.1 Electromagnetic radiation from radio waves to X-rays in wavelength and frequency (adapted and redesigned from BRLABS [8]).

1.2.2 THz application

Various THz applications can be found from pure science to industry [9]. For instance, many molecules have rotational and vibration absorption spectra at THz frequencies, and hence broadband THz time domain spectroscopy (THz-TDS) techniques provide a convincing tool for chemical scientists [10] [11]. Another interesting field is non-invasive THz imaging, as THz can propagate through papers and plastics without ionizing materials unlike X-ray [12]. For security purposes, one can develop a detection system which can image inside of postal boxes or envelopes and even identify unknown materials by using THz spectroscopic finger prints [13] [14]. In addition, THz pump-probe experiment and nonlinear THz study can provide a material's unique properties such as the transient dielectric constant [15–18]. As shown in the examples above, the generation of intense THz radiation is of considerable interest in many academic and industrial areas [19–23].

1.2.3 Conventional femtosecond laser techniques for THz pulse generation

Despite a wide range of applications and needs, there have not been many suitable sources for THz study. However, there has been notable progress in developing tabletop THz pulse sources by utilizing femtosecond lasers. Examples include ultrafast photoconductive antenna and optical rectification in nonlinear crystals, which are two widely adopted techniques in the THz community.

First, in the photoconductive antenna scheme, an ultrashort laser pulse illuminates onto the gap between two electrodes deposited on a semiconductor substrate such as LT-GaAs and InP. This rapidly generates photo-carriers [24] as shown in Fig. 1.2. The photo-excited carriers (electrons and holes) are then accelerated by the external biased field (V_{DC} in Fig. 1.2), and this current surge emits THz radiation in the far field.

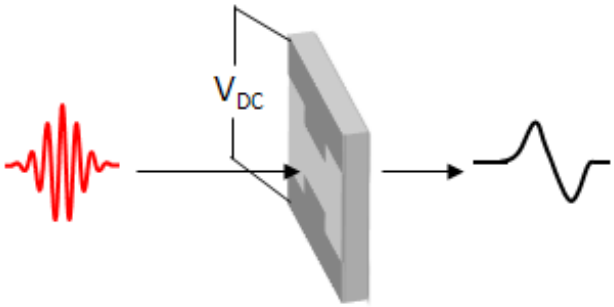

Figure 1.2 THz generation using a biased photoconductive antenna illuminated by an ultrashort pulse.

In this scheme, the generated THz field is typically described by [25],

$$E_{THz} = \frac{1}{4\pi\varepsilon_0}\frac{A}{c^2 z}\frac{\partial J(t)}{\partial t}, \qquad (1\text{-}1)$$

where *A* is the gap area illuminated by the laser source and *z* is the distance from the source to the detection point. As shown in Eq. (1-1), the THz yield depends on the substrate properties and electrode size/design. Although there have been interesting reports on maximizing the THz yield using large area photoconductors, the output is relatively small compared to other methods including optical rectification or two-color laser mixing in air [26] [27].

The other method widely used with femtosecond lasers is optical rectification in non-centrosymmetric crystals such as ZnTe, GaP, and GaSe. The process can be described by the second order nonlinear susceptibility, expressed by [7] [28],

$$P_2^{nl} = \chi_2 \frac{E_0^2}{2}[\cos(\omega_1 - \omega_2)t + \cos(\omega_1 + \omega_2)t] \quad (1\text{-}2)$$

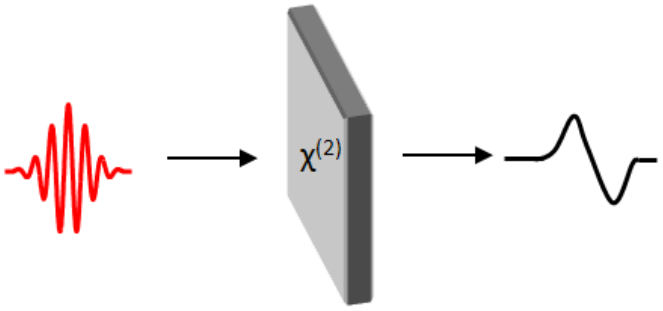

Figure 1.3 THz generation by ultrashort laser pulse in a nonlinear crystal via optical rectification.

The first term in Eq. (1-2) is related to THz radiation. Optical rectification process is considered as a difference frequency mixing between two spectral components (ω_1 *and* ω_2) within a broadband femtosecond pulse. Here the effective nonlinear coefficient, $\chi^{(2)}$, and phase matching condition in the crystal determine the overall THz yield [17]. In particular, lithium niobate ($LiNbO_3$) crystals with tilted

pulse front excitation provides extremely high THz energy, 125 μJ per pulse (current record), using this optical rectification process [29].

1.3 THz generation using two-color laser mixing in plasma

Compared to ultrafast photoconductive antennas in semiconductors or optical rectification in nonlinear crystals, two-color laser mixing provides intense and broadband THz pulses [30]. For example, optical rectification in $LiNbO_3$ crystals provides radiation spectra only up to 1.5 THz despite its intense radiation [29]. By contrast, two-color laser mixing is reported to provide ultra-broadband radiation up to 200 THz [30] . The source also produces extremely low frequency radiation (<0.01 THz). Basically, this produces electromagnetic (EM) radiation ranging from radio-microwave to near infrared frequencies. This provides an attractive characteristic for broadband spectroscopic studies, and thus strong THz pulse generation via ultrafast, two-color laser focusing in air has attracted considerable attention for broadband THz spectroscopy, THz imaging, and nonlinear THz studies [30–54].

1.3.1 Mechanisms of laser induced ionization

As our femtosecond laser readily ionizes ambient air molecules, it is useful to describe some basics of photoionization mechanisms before discussing our photocurrent model for THz pulse generation. Figure 1.4 shows two dominant

ionization processes, multiphoton and tunneling ionization at laser intensities of 10^{12} - 10^{15} W/cm^2.

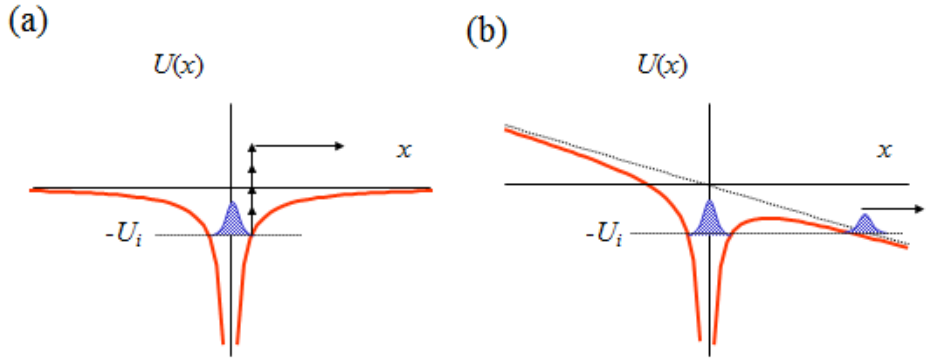

Figure 1.4 Laser induced ionization in (a) multiphoton and (b) tunneling models where U_i is the ionization potential energy of the atom (courtesy: K. Kim [55]). In multiphoton ionization, multiple photons are simultaneously absorbed to excite bound electrons to a continuum state. In the case of tunneling ionization, the bound electrons tunnel through the Coulomb barrier suppressed by an external electric field and then become freed.

Conventionally, photoionization process can be characterized by the Keldysh parameter γ_k, described by [55],

$$\gamma_k = \sqrt{U_i / 2U_p} = \sqrt{\frac{t_i}{T}} \qquad (1\text{-}3)$$

where U_i is the ionization potential energy of an atom or ion, U_p is the laser ponderomotive potential energy, $U_p = e^2E^2 / 4m_e\omega^2$, t_i is the ionization time and T is the laser oscillation period given by $T = 2\pi/\omega$ [56,57]. For $\gamma_k >> 1$, the ionization is dominated by the multiphoton process whereas the tunneling process is dominant for $\gamma_k < 1$. In terms of laser intensity, the multiphoton process is responsible for relatively low laser intensities $<10^{12}$ W/cm^2, whereas tunneling ionization is responsible for

~10^{14} W/cm^2. For our laser system providing intensities of 10^{13} ~10^{15} W/cm^2, tunneling ionization is found to be the dominant ionization process.

1.3.2 Photocurrent model for THz radiation in two-color mixing

In the two-color THz generation scheme, an ultrashort laser's fundamental and its second harmonic pulses are focused together in air, which radiates THz pulses. Two competing models have been proposed to explain the generation mechanism, four-wave mixing [31] and the photoionization process [34]. Analogous to optical rectification in nonlinear crystals, the four wave mixing process can be seen as an effect by the third order nonlinearity in air $\chi_3(\Omega = \omega + \omega - 2\omega)$ [31]. On the other hand, one can view the same process as a photocurrent surge, similar to the previous photoconductive antenna scheme.

Here we introduce and describe the photocurrent model and its simulation results [47–49]. A femtosecond laser pulse's fundamental (ω) and its second harmonic (2ω) pulses co-propagate and co-focus to ionize air molecules. The combined laser field E_L at the focus can be expressed as,

$$E_L = E_\omega(t)\cos(\omega t) + E_{2\omega}(t)\cos(2\omega t + \theta), \tag{4-1}$$

where $E_\omega(t)$ and $E_{2\omega}(t)$ are the amplitudes of the fundamental and the second harmonic fields, respectively, θ is the relative phase between $E_\omega(t)$ and $E_{2\omega}(t)$ at the focus. At the focal volume, tunneling ionization occurs by the combined laser field,

and the ionization rate can be simplified as for a hydrogen atom in a static DC field [58],

$$w(t) = 4\omega_a \left(\frac{E_a}{E_L(t)} \right) \exp\left(-\frac{2}{3} \frac{E_a}{E_L(t)} \right), \tag{2-4}$$

where $E_L(t) = |\boldsymbol{E}_L|$ is the combined laser field amplitude at the focus, $E_a = 5.14 \times 10^9$ V/cm is the atomic field, and $\omega_a = 4.134 \times 10^{16}$ s^{-1} is the atomic frequency. In our simulation, we used the Ammosov-Delone-Krainov (ADK) tunneling ionization rate [56] instead of Eq. (2-4). Although the ADK model has been introduced mainly for noble gases, it also works well for structureless atomic-like molecules such as neutral N_2 (the primary constituent gas of atmospheric air).

Once we know the electron density, one can calculate the local plasma current density given by [49]

$$J(t) = -\int e v_d(t, t') dN_e(t'), \tag{4-2}$$

where $dN(t')$ is the density of free electrons produced by the laser field in the interval between t' and $t' + dt'$, and $v_d(t, t')$ is the drift velocity of those electrons at t.

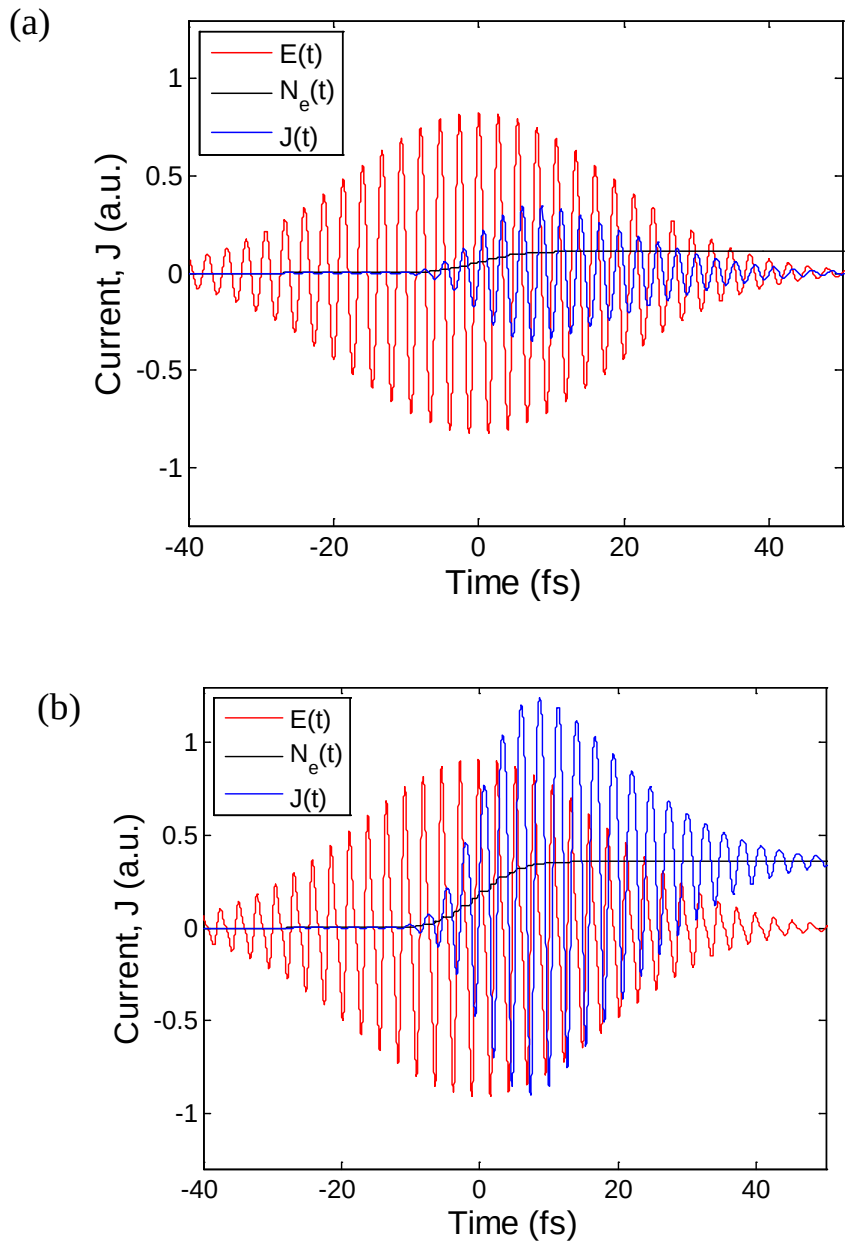

Figure 1.5 Simulation results of the free electron density (black line) and photocurrent (blue line) induced by a femtosecond laser pulse (red line) for (a) single-color with $I_\omega = 1 \times 10^{14}$ W/cm^2 and (b) two-color mixing with $I_\omega = 9 \times 10^{13}$ W/cm^2 and $I_{2\omega} = 1 \times 10^{13}$ W/cm^2 and $\theta = \pi/2$.

For example, Figure 1.5 shows the simulated electron density (black line) and plasma current (blue) induced by a femtosecond laser pulse (red line) for single-color and two-color mixing cases. We use $I_\omega = 10^{14}$ W/cm^2 for single-color ionization and

$I_\omega = 9 \times 10^{13}$ W/cm^2, $I_{2\omega} = 1 \times 10^{13}$ W/cm^2 and $\theta = \pi/2$ (relative phase) for two-color ionization. Note that single color ionization provides simply an oscillating current (see Fig. 1.5(a)) with a net current of zero. By contrast, two-color ionization yields a directional net current whose magnitude is greatly sensitive to the relative phase between the fundamental and second harmonic fields. In this case, we used $\theta = \pi/2$ (see Fig. 1.5(b)). This directional current surge which occurs on the timescale of the laser envelope (or photoionization) emits THz radiation $E_{\mathrm{THz}} \propto dJ(t)/dt$ in the far field [47–50]. For laser pulse duration of <100 fs, this process can generate electromagnetic radiation from 1-10 THz.

1.4 Summary of dissertation

The main focus of this dissertation is intense terahertz (THz) generation using two-color laser mixing in air. This chapter introduces THz science and conventional tabletop THz pulse sources and also describes the photocurrent model for two-color laser based THz radiation.

In chapter 2, the one-dimensional plasma current model is expanded to two-dimensional (2-D) to take into account two-color laser fields with arbitrary polarization. Using the 2-D model, the conditions for optimal THz generation have been simulated and experimentally verified. Here, various laser parameters such as the relative phase of two-color laser pulses, the azimuth and tilt angle of the BBO (Beta Barium Borate) crystal, and the input laser pulse duration have been adjusted. A

full control of terahertz output is demonstrated and explained in the context of the 2-D photocurrent model.

In chapter 3, output THz yield versus laser energy is tested. We present our recent study on THz energy scaling and saturation in two-color mixing with using various focal length lenses and input laser energies up to 60 mJ. With a high power laser, THz yield saturation has been observed via transverse fluorescence imaging. We overcome the saturation effect by elongating the filaments and achieve 7 μJ of THz energy.

Chapter 4 covers macroscopic effects in filamentation which govern THz output energy yields and radiation profiles in the far field. We investigate high-power THz generation in two-color laser filamentation with terawatt (TW) lasers including a 0.5 TW, 1 kHz repetition (rep) rate system, as well as, 2 TW and 30 TW systems operating both at 10 Hz rep rate.

Chapter 5 introduces various broadband THz detection methods. We find that THz radiation from two-color mixing in air provides extremely broad EM radiation. Here we characterize the radiation spectra at a broad range of frequencies covering radio-micro waves to infrared frequencies by complementary THz detection methods.

Chapter 6 gives a conclusion and outlook for intense THz generation via two-color laser mixing. Lastly, Appendix A details the laser system used in this dissertation, including a newly developed high-repetition-rate laser system enabled by cryogenic cooling.

Chapter 2 : Two-dimensional plasma current and optimized terahertz generation in two-color photoionization

2.1 Introduction to two-color photoionization for THz generation

Recently, THz generation via two-color laser mixing in air [30–54] has attracted a considerable amount of interest due to its capability of producing broadband and high-power THz pulses [47–49]. In this scheme, an ultrashort pulsed laser's fundamental (ω) and its second harmonic (2ω) pulses are co-focused in air to ionize air molecules. From the laser-ionized plasma, strong THz pulse emission is observed. The nonlinearity responsible for such THz generation originates from rapid tunneling ionization and subsequent electron motion in a symmetry-broken electric field [47–49]. This photocurrent model [47–49] can explain the microscopic origin of the third order nonlinearity $\chi^{(3)}$ (generally all high order nonlinearities $\chi^{(n)}$) in THz generation via two-color photoionization.

In our previous studies [47–49], the plasma current model was simulated in the situation where ω is polarized in the same direction of 2ω polarization. Experimentally, this can be achieved by splitting off the orthogonally polarized 2ω pulse (type-I phase matching) and rotating its polarization to be parallel to the ω pulse polarization with a half-wave plate, and finally combining the two-color pulses with beam splitter for THz generation. This scheme was previously demonstrated in Ref [35] and is useful for individually controlling laser parameters and/or polarizations of 2ω and ω pulse. However, the scheme is very sensitive to any phase

change due to mechanical vibration or air turbulence occurring in the split and combined beam path. For example, less than a few μm vibrations can effect a phase shift of ~2π, which can greatly affect the THz output.

Because of its phase instability in the aforementioned splitting system, most two-color photoionization experiments adopt an all-in-line second harmonic and THz generation arrangement as shown in Fig. 2.1(a). In this scheme, the BBO (Beta Barium Borate) crystal needs to be azimuthally oriented such that the incoming ω field has a component parallel to the 2ω field polarized in the extraordinary (ê) axis of the BBO crystal. In this case, the fundamental pulse becomes elliptically polarized after passing through the crystal whereas the second harmonic remains polarized along the extraordinary axis. This setting invokes two-dimensional (2-D) transverse electron currents for THz generation [38]. Previously, it was shown that the polarization and power of THz radiation are sensitive to the phase difference between the fundamental and second harmonic fields and also the azimuthal angle of BBO [37,38].

In chapter 2, we develop a 2-D plasma current model to include full laser experimental parameters, which can ultimately control output THz yields and polarization. We also compare our 2-D model simulation results with experimental data in finding conditions for maximum THz generation.

2.2 Transverse 2-D photocurrent model and simulation

Starting from 1-D photocurrent model [47–49], we expand it to two-dimensional by taking into account of transverse 2-D laser fields as shown in Fig. 2.1(b). When a fundamental laser pulse passes through a birefringent BBO crystal, its amplitude can be decomposed into two orthogonal fields, $E_{\omega o}$ and $E_{\omega e,}$ polarized along the ordinary (ô) and extraordinary (ê) axes of the crystal, respectively. Here the second harmonic pulse produced by type-I phase matching is polarized along the ê axis.

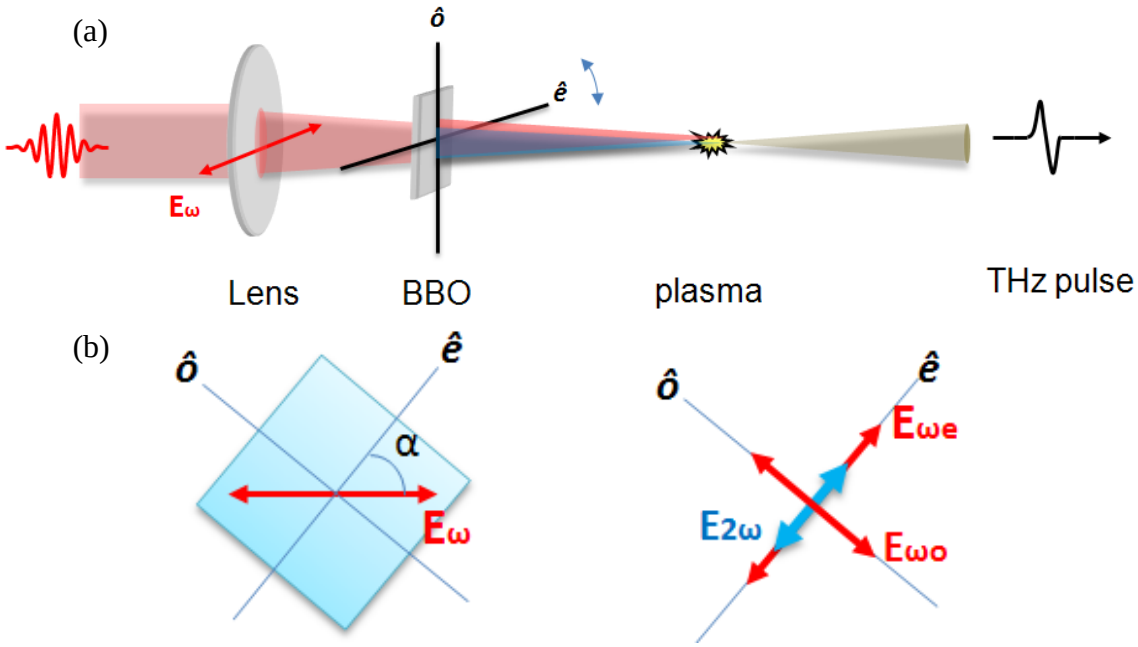

Figure 2.1 (a) Schematic of all-in-line second harmonic and THz generation. (b) Vector diagram for fundamental (E_{ω}) and its second harmonic ($E_{2\omega}$) generation before the BBO crystal and at the front end of plasma filament. **ô** and **ê** represent the ordinary and extraordinary axes of the BBO crystal, respectively. $E_{\omega o}$ and $E_{\omega e,}$ polarized along the ordinary (**ô**) and extraordinary (**ê**) axes of the crystal.

Each field along the ordinary (ô) and extraordinary (ê) axes can be calculated by

$$
\begin{aligned}
E_{\omega o} &= E_{\omega} \sin(\alpha), \\
E_{\omega e} &= E_{\omega} \cos(\alpha), \\
E_{2\omega} &= d_{eff} (E_{\omega})^2 \sin^2(\alpha),
\end{aligned}
\tag{2-1}
$$

where E_{ω} and $E_{2\omega}$ are the amplitudes of the fundamental (ω) and the second harmonic (2ω) fields, d_{eff} is the effective conversion coefficient of the BBO crystal from ω to 2ω, and α is the angle between the incoming ω polarization (horizontal axis) and the $\hat{\mathbf{e}}$ axis [see Fig. 2.1(b)]. Then the combined laser field at the focus is expressed as

$$
E_L = E_{\omega e} \cos(\omega t)\hat{\mathbf{e}} + E_{\omega o} \cos(\omega t + \varphi)\hat{\mathbf{o}} + E_{2\omega} \cos(2\omega t + \theta)\hat{\mathbf{e}}, \tag{2-2}
$$

with

$$
\varphi = \omega(n_{\omega e} - n_{\omega o}) l / c, \quad \theta = \omega(n_{\omega} - n_{2\omega}) d / c + \theta_0, \tag{2-3}
$$

where φ is the phase retardation between $E_{\omega e}(t)$ and $E_{\omega o}(t)$, the projection components of the ω field after passing through the BBO crystal of thickness l, $n_{\omega o}$ and $n_{\omega e}$ is the refractive index of the BBO crystal along the $\hat{\mathbf{o}}$ and $\hat{\mathbf{e}}$ axis, respectively. Also, θ is the relative phase between $E_{\omega e}(t)$ and $E_{2\omega}(t)$ as used in the previous reports [47–49] , c is the speed of light in vacuum, d is the distance between the plasma and BBO crystal, n_{ω} and $n_{2\omega}$ is the refractive index of air at ω and 2ω frequency, respectively, and θ_0 is the phase difference right after the BBO crystal. In practice, θ can be varied by changing the distance to plasma, d [47] , and φ can be controlled by tilting the angle of the BBO crystal and thus varying the optical path length l in the BBO crystal (see Sec. 2.3 for details).

From the 2-D laser field in Eq. (2-2), one can calculate the quasi-DC tunneling ionization rate given by [58] ,

$$w(t) = 4\omega_a \left(\frac{E_a}{E_L(t)} \right) \exp\left(-\frac{2}{3} \frac{E_a}{E_L(t)} \right), \qquad (2\text{-}4)$$

where $E_L(t) = |\boldsymbol{E}_L|$ is the combined laser field amplitude at the focus, $E_a = 5.14 \times 10^9$ V/cm is the atomic field, and $\omega_a = 4.134 \times 10^{16}$ s^{-1} is the atomic frequency. In our simulation, we used the Ammosov-Delone-Krainov (ADK) tunneling ionization rate [56]. Although the ADK model has been introduced mainly for noble gases, it also works well for structureless atomic-like molecules such as neutral N_2 (the primary constituent gas of atmospheric air). From the ionization rate equation, the time-varying electron density $N_e(t)$ can be computed with multiple degrees of ionization taken into account [49]. Here we ignore collisional ionization, plasma recombination, and electron attachment to neutral molecules, which is a valid assumption because those events occur much more slowly compared to the pulse duration <50 fs considered here [59].

Once the electron density is estimated from the ADK ionization rate, the plasma current density can also be obtained as

$$J(t) = -\int ev(t,t')dN_e(t') \quad \text{and} \quad v(t) = -(e/m_e)\int_{t'}^{t} E_L(t)dt, \qquad (5)$$

where $dN_e(t')$ is the change of electron density in the interval between t' and $t' + dt'$, and $v_e(t, t')$ is the velocity of those electrons at t. Now, one can consider 2-D transverse current density given by $\boldsymbol{J}_\perp = J_o\hat{\mathbf{o}} + J_e\hat{\mathbf{e}}$, where J_o and J_e is the current density component along the $\hat{\mathbf{o}}$ and $\hat{\mathbf{e}}$ axis, respectively. This current density is the origin of THz radiation and its yield is expressed by the derivative of the current density as $\boldsymbol{E}_{\mathrm{THz}} \propto d\boldsymbol{J}_\perp(t)/dt$. Here, the two orthogonal current densities (J_o and J_e) are always in phase in which θ and φ do not change over the entire pulse duration, and

this makes the far-field THz radiation linearly polarized. Here, the THz polarization angle is determined by the relative strength between J_o and J_e.

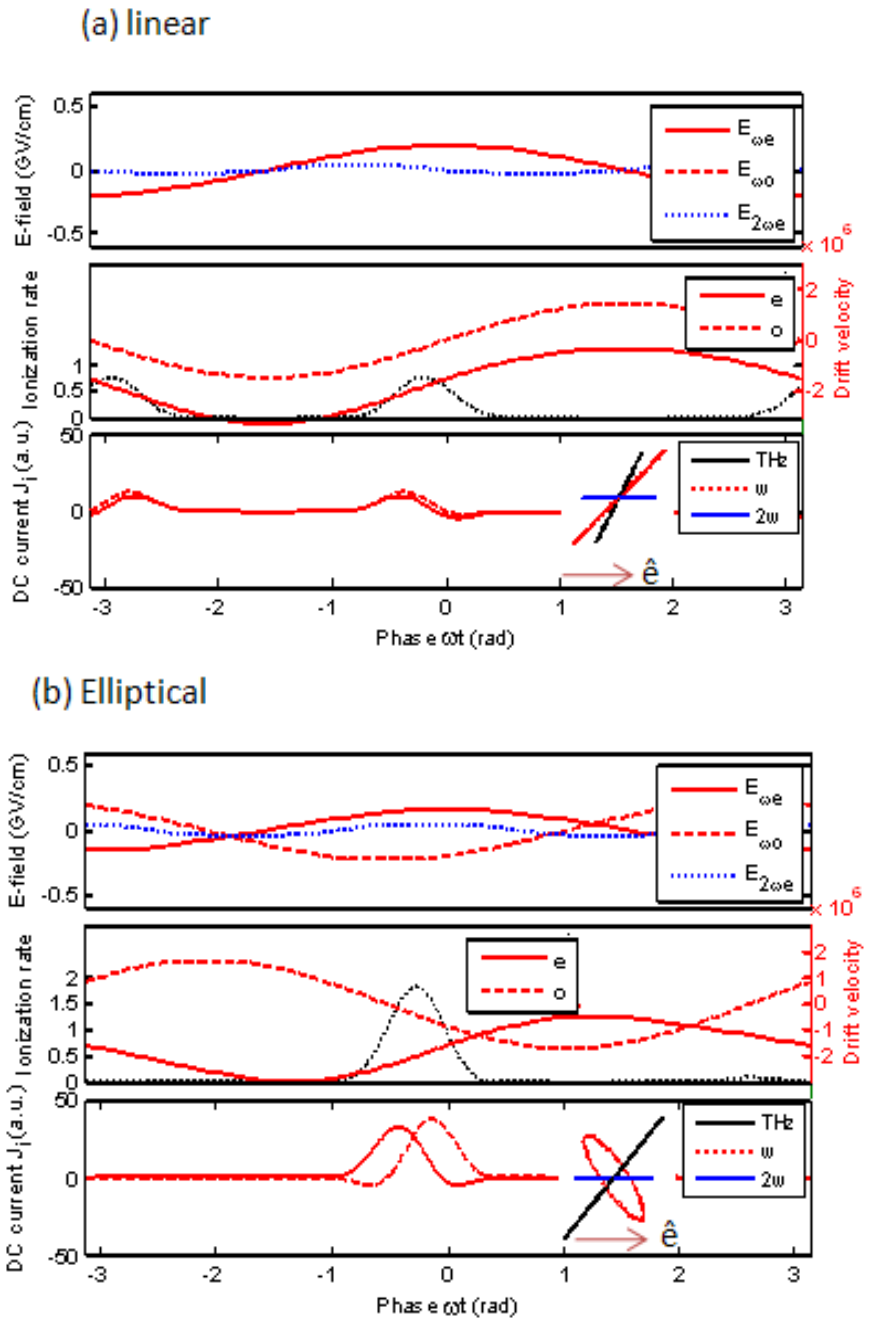

Figure 2.2 2-D plasma current producing linear fundamental field case; (a) φ = 0˚ a = 45˚, and θ = 90˚ (left) and elliptical fundamental field case; (b) φ

= 210˚, a = 55˚, and θ = 20˚ at peak laser intensities of $I_\omega = 10^{14}$ W/cm^2 at λ_ω = 800 nm and $I_{2\omega} = 0.8 \times 10^{13}$ W/cm^2 at $\lambda_{2\omega}$ = 400 nm. Over one cycle of the fundamental field ($-\pi < \omega t < \pi$) are shown the laser fields $E_{\omega e}$ (red solid line), $E_{\omega o}$ (red dashed line), $E_{2\omega}$ (blue dotted line); ionization rate calculated by the total field (black dotted line) and electron drift velocities along the **ô** (red dashed line) and **ê** (red solid line) axes; plasma currents J_o (red dashed line) and J_e (red solid line) along the **ô** and **ê** axis, respectively. The insets show the polarization diagrams of E_ω (red line), $E_{2\omega}$ (blue line), and E_{THz} (black line) for the two cases.

Figure 2.2 shows selected simulation results of 2-D plasma current model for two different cases. In the first case, Fig. 2.2(a), both E_ω and $E_{2\omega}$ are linearly polarized with an angle of 45˚, which can occur when φ = 0˚ and α = 45˚. In this case, the total current density summed over one cycle is maximized at θ = 90˚. This also means that maximum THz radiation occurs at θ = 90˚, consistent with our previous 1-D model [47]. The inset in Fig. 2.2(a) shows the polarization diagrams of all three waves, E_ω, $E_{2\omega}$, and E_{THz}.

In the second case, Figure 2.2(b), E_ω is elliptically polarized (φ = 210˚, α = 55˚) while $E_{2\omega}$ is linearly polarized. In this case, the maximum THz yield occurs at θ = 20˚. The inset in (b) shows the angle of THz polarization with respect to those of the other two waves E_ω and $E_{2\omega}$. Here, we note that the elliptical field case (b) produces almost four times higher THz fields compared to the linear polarization case (a). This suggests that linearly-polarized (but not parallel) two-color fields do not necessarily yield the maximal THz output in the all-in-line THz generation configuration. Thus, one needs to find the optimal φ, α, and θ parameters which maximize the THz output.

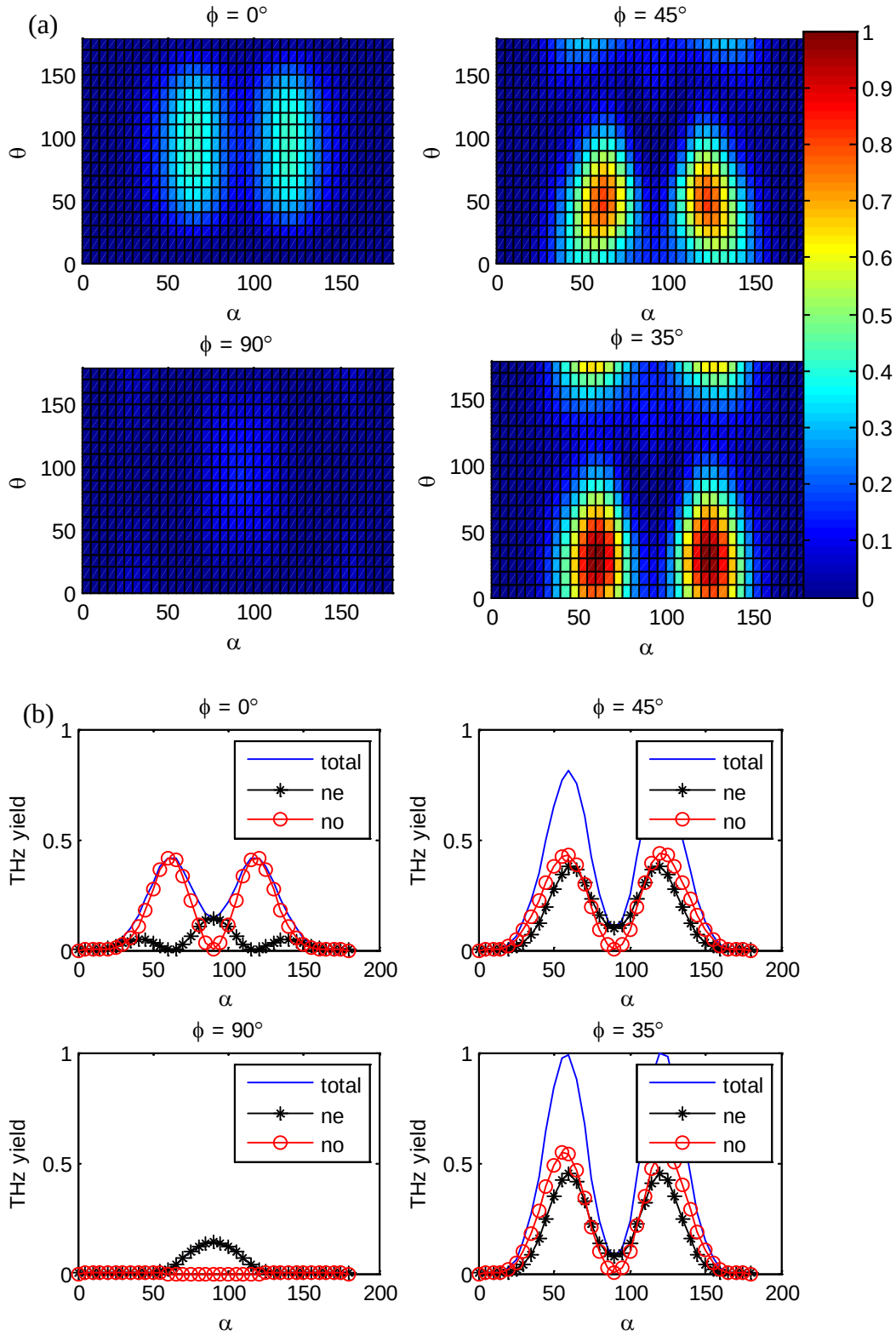
(a)
ϕ = 0°
ϕ = 45°
ϕ = 90°
ϕ = 35°
θ
α
0
50
100
150
1
0.9
0.8
0.7
0.6
0.5
0.4
0.3
0.2
0.1
(b)
THz yield
total
ne
no
200

Figure 2.3 (a) Resulting $|\boldsymbol{J}_\perp|^2$ (or THz yields) as a function of θ and a (degrees) for four different φ = 0˚, 45˚, 90˚, and 210˚. (b) In each 2-D simulation, the line which yields the local $|\boldsymbol{J}_\perp|^2$ maximum at a fixed θ is selected and plotted as a function of a for $|J_o|^2$ (line with circles), $|J_e|^2$ (line with asterisks), and $|\boldsymbol{J}_\perp|^2$ (solid line).

Based on the 2-D photocurrent simulation, Figure 2.3 shows 2-D THz yield color map. The 2-D electron current density squared, $|\boldsymbol{J}_\perp|^2$ (equivalently THz yield) is examined by varying all three simulation parameters (φ, θ, and α). Figure 2.3(a) shows $|\boldsymbol{J}_\perp|^2$ as a function of θ and α for four φ values (φ = 0˚, 45˚, 90˚, and 210˚). For each 2-D plot $|\boldsymbol{J}_\perp|^2$ (α, θ), the line which has a local maximum is selected and plotted as a function of α for $|J_o|^2$, $|J_e|^2$, and $|\boldsymbol{J}_\perp|^2$ (bottom). The maximum THz yield occurs at φ = 210˚, θ = 20˚, and α = 55˚. One should note that the maximum yield does not occur at θ = 90˚ anymore owing to 2-D photocurrents. In the case of φ = 210˚, the THz polarization angle is ~60˚ with respect to the $\hat{\mathbf{e}}$ axis as shown in Fig. 2.1(b). With φ = 90˚, the fundamental field E_ω is circularly polarized and the resulting THz field is purely polarized along the $\hat{\mathbf{e}}$ axis [see Fig. 2.3 (b)].

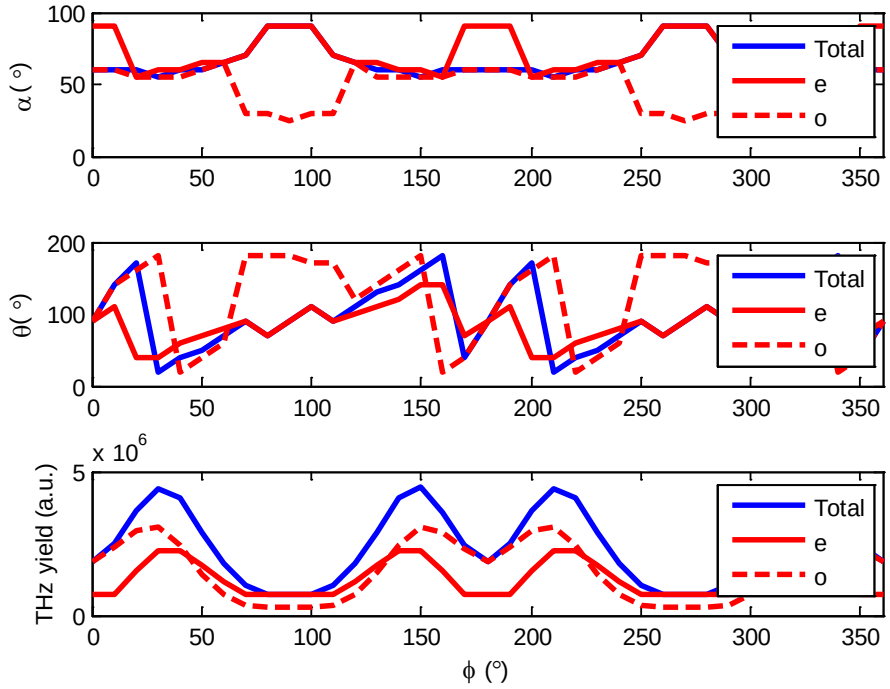

Figure 2.4 Optimal α and θ values maximizing THz output for a given φ value. It considers three maximum types: $|J_o|^2$ (red dashed line), $|J_e|^2$ (red solid line), and $|\boldsymbol{J}_\perp|^2$ (blue solid line). This shows the total THz radiation (or $|\boldsymbol{J}_\perp|^2$) peaks at φ = 30˚, 150˚, 210˚, and 330˚ and at α ~55˚.

Figure 2.4 summarizes 2-D photocurrent simulation data and presents the optimal α and θ which maximize $|J_o|^2$, $|J_e|^2$, and $|\boldsymbol{J}_\perp|^2$ for varying φ value ($0^\circ \le \varphi < 360^\circ$). For instance, the total THz output (blue solid line) peaks at φ = 30˚, 150˚, 210˚, and 330˚ (see the last graph). At given φ angles, α and θ values maximizing the total THz yield are shown in the first and second graphs. For all cases, the maximum THz yield occurs at $\alpha \sim 55^\circ$, and this agrees well with previous experimental reports employing all-in-line schemes [34,38]. We also note that the optimal θ has a broad range of values depending on φ and whether the total or polarized ($\hat{\mathbf{o}}$ or $\hat{\mathbf{e}}$) yield is calculated.

2.3 Experiment and simulation results

The experimental setup for 2-D photocurrent study is shown in Fig. 2.5. A Ti:sapphire laser system delivering a 800 nm center wavelength, ~6 mJ, 25 fs pulses at a 1 kHz repetition rate (Legend elite USX, Coherent Inc.) is used to generate THz radiation.

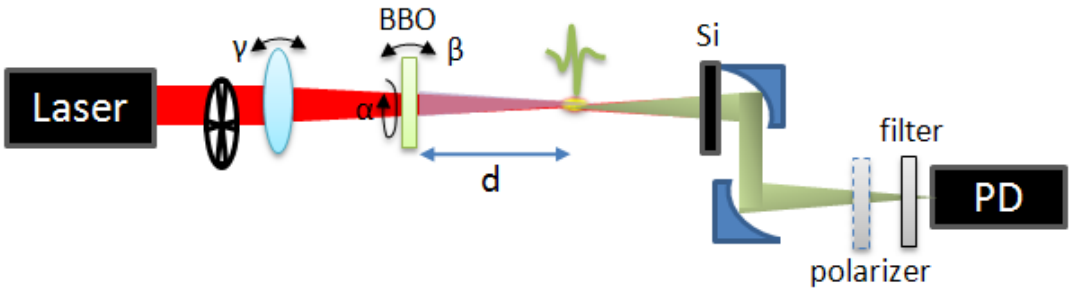

Figure 2.5 Schematic setup for THz generation and detection. The far-field THz yield and polarization is measured with a pyroelectric detector combined with a wire-grid polarizer and filters (Teflon, HDPE, Sapphire, or Ge). THz output is controlled by varying the distant from BBO to filament (d), azimuthal angle of BBO (α), tilt angle of BBO (β), and tilt angle of lens (γ).

The fundamental laser pulses (ω) are focused by a focusing lens (250 mm) and propagate through a 0.1-mm thick BBO crystal (type-I) which generates second harmonics. The fundamental (ω) and second harmonic pulses (2ω) co-propagate and ionize atmospheric air at the focus, generating THz radiation. A 5-mm thick silicon (Si) wafer is placed to block the optical pulses, whereas the THz radiation produced at the focal spot is collected and focused by two off-axis parabolic mirrors into a pyroelectric detector (SPI-A-62THZ, Spectrum detector Inc.). For low (<3 THz) and

high (<10 THz) frequency THz detection, an additional 1.5-mm thick Teflon, 1.5-mm thick high-density polyethylene (HDPE), 2-mm thick Sapphire, or 2-mm thick Ge filter is placed in front of the detector. For low-frequency (<3 THz) THz polarization detection, an optional wire-grid polarizer (G50x20, Microtech instruments, contrast >95:2 below 3 THz) with 50 μm wire spacing and 20 μm wire diameter is placed in front of the pyroelectric detector.

We control the relative amplitude, $E_{\omega e}/E_{2\omega}$, by azimuthally rotating the BBO angle α, relative phase θ by moving the BBO position d, and phase retardation φ by tilting the BBO angle β. Furthermore, we change the filament length by tilting the focusing lens angle γ.

2.3.1 Relative phase (θ or d) effect on THz yields

The first experimental test is studying the effect of the relative phase (θ) on output THz yields. Figure 2.6(a) shows the THz yield measured by a function of the BBO to focus distance d. As mentioned in the experimental setup, five lines were obtained with five different filters (Si, Ge, Sapphire, HDPE, or Teflon) placed in front of the pyroelectric detector. All five lines increase quadratically with decreasing d, and an additional oscillatory modulation occurs with a period of ~2.5 cm. This quadratic and oscillatory trend was previously reported [47] and consistent with the air dispersion term shown in Eq. (2-3) [34]. However, distinct from previous electro-optic (EO) based measurements [34,38,47], the yield does not reach the bottom when the yields are minimal. This imperfect oscillatory behavior can be explained by the 2-D plasma current model described in Section 2.2. As shown in our simulation result

in Fig. 2.6(b), the total THz wave can be considered as the superposition of two orthogonal THz fields polarized along the ordinary and extraordinary axes. The total yield curve (blue line) in Fig. 2.6(b) reproduces the experimental trend shown in Fig. 2.6(a). It is important to note that the individual yields, $|E_{\mathrm{THz,o}}|^2$ (red dotted line) or $|E_{\mathrm{THz,e}}|^2$ (green dotted line) follow the complete oscillatory θ dependence, reaching the bottom at local minimum, agreeing with the previous EO-based measurements [34,38,47].

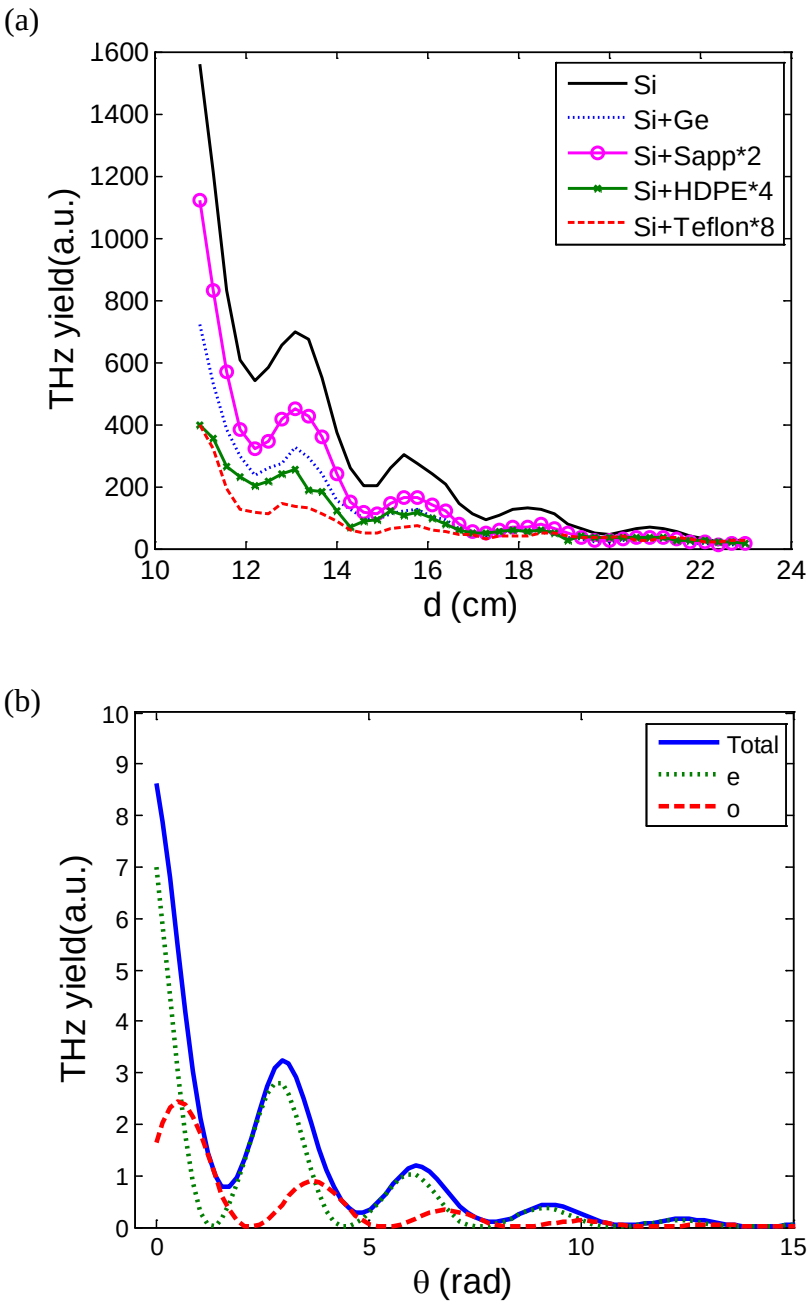

Figure 2.6 (a) Measured THz yield dependence on the relative phase (φ) obtained with various THz filters: Si (black solid line), Ge (blue dotted line), Sapphire (magenta line with circles), HDPE (green line with x), and Teflon (red dashed line), in addition to the Si filter. Here, the Sapphire, HDPE, and Teflon signal are rescaled by a multiplication factors of 2, 4 and 8, respectively.

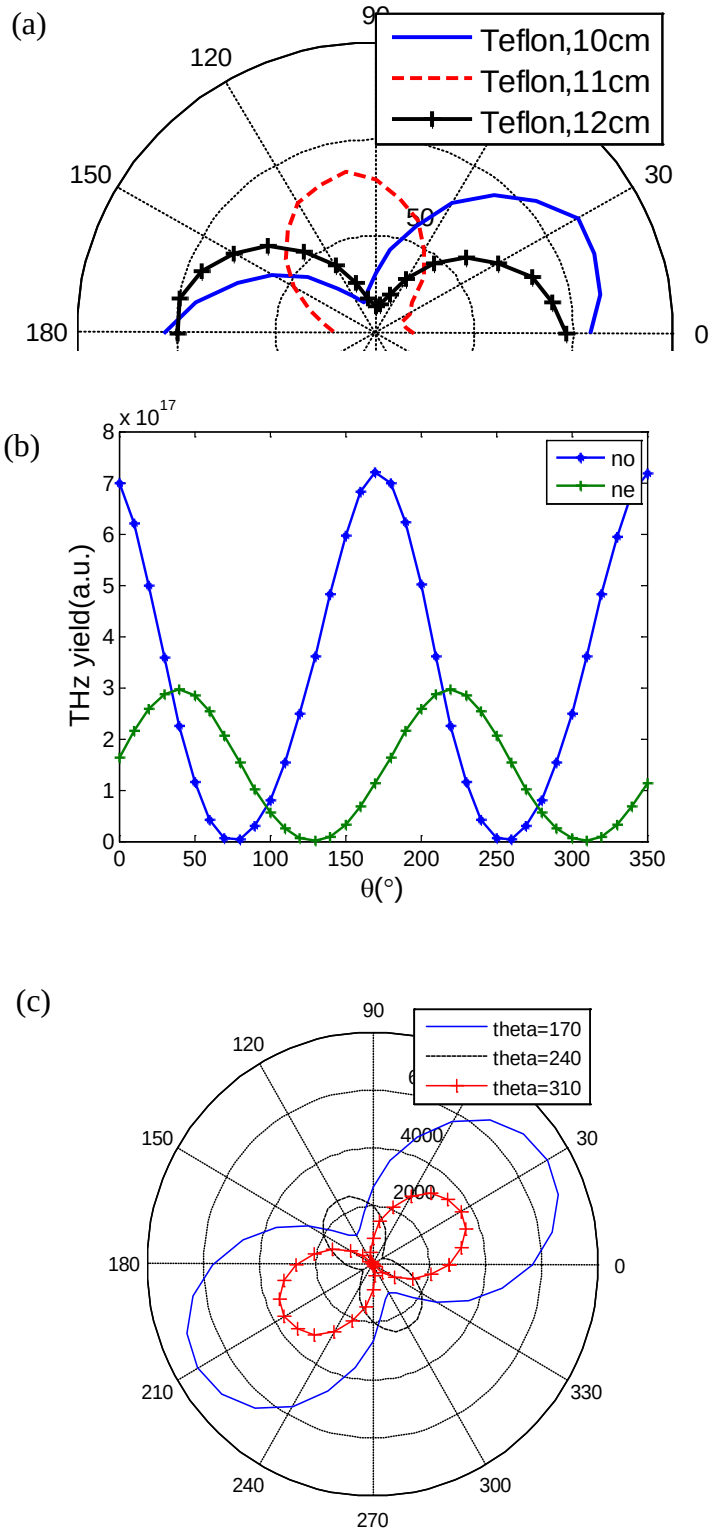

Figure 2.7 (a) THz polarization angular map with three different positions of BBO crystal at 10 cm, 11 cm, and 12 cm. (b-c) Simulated THz yields with varying θ for the total (blue line), **ô**-polarized (red line with +), **ê**-

polarized (green dotted line) THz yields. In the simulation, φ = 210˚ (or β ≈ 1˚) and α= 55˚ are assumed.

Figure 2.7(a) shows three polarization maps obtained with three different d (or θ) values , d = 10 cm, 11 cm, and 12 cm . It is shown that the THz polarization rotates with varying θ, which is consistent with the 2-D plasma current model and the previous reports [37,38]. Because the THz yields along ê and ô axes are a function of θ, the THz polarization is rotating as the relative phase θ changes. The simulation results (Fig. 2.7(c)) show the total (blue line), **ô**-polarized (red line with +), **ê**-polarized (green dotted line) THz yields with varying θ. With three different θ values, we can simulate the polarization condition shown in our experimental results. Thus our 2-D photocurrent model can be applied in describing the rotation of THz polarization.

2.3.2 Azimuth (α) and tilt (β) angle effects on THz yields and polarization

The azimuth α and tilt β angles of BBO crystal also affects THz output yield and polarization. To quantify those effects, THz yields are measured with varying α and β.

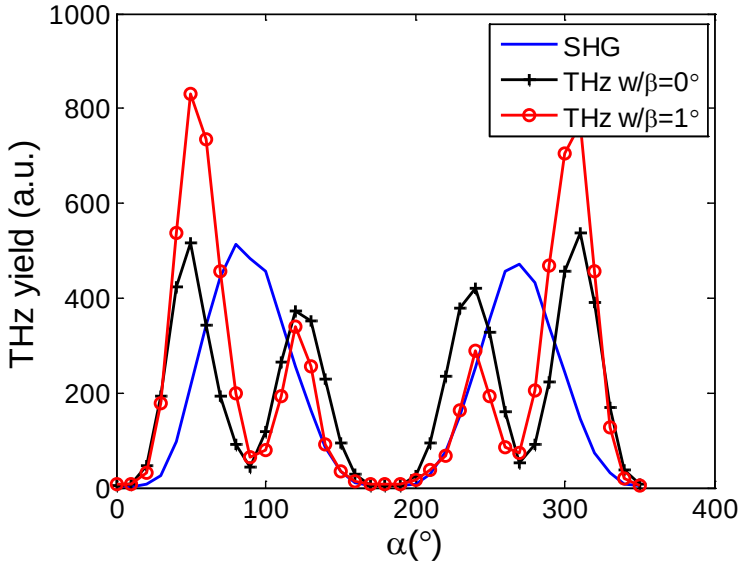

Figure 2.8 THz yields as a function of α angle at β = 0˚ (black line with +) and β = 1˚ (red line with o). Co-plotted is the second harmonic intensity (blue line).

To evaluate the THz yield dependence on the azimuth angle α of BBO crystal, the output THz yield is measured over the azimuth angle α of BBO crystal. The blue line in Fig. 2.8 shows second harmonic generation from BBO, and it is maximized when the ω polarization is aligned with the ordinary axis of the BBO (i.e. α = 90), but that is not the case of maximum THz yield. The maximum THz occurs at $\alpha \approx 50^{\circ}$, consistent with the previous reports and very close to our simulation result $\alpha = 55^{\circ}$ [35]. Figure 2.8 also shows that THz yield is varied with tilting angle β. To optimize the output THz yield, one needs to tune the BBO crystal. This is equivalent to controlling φ as mentioned in the simulation section. Figure 2.8 also shows the THz yield as a function of α at two tilt angles β = 0˚ (black line with +) and β = 1˚ (red line with o). It shows that $\beta \approx 1^{\circ}$ provides the higher signal (60% more), which suggests that one needs to optimize φ, or practically β, to maximize the THz output.

Here, we estimate φ to be 268˚ and 210˚ at $\beta \approx 0$˚ and 1˚, respectively, in our BBO crystal case.

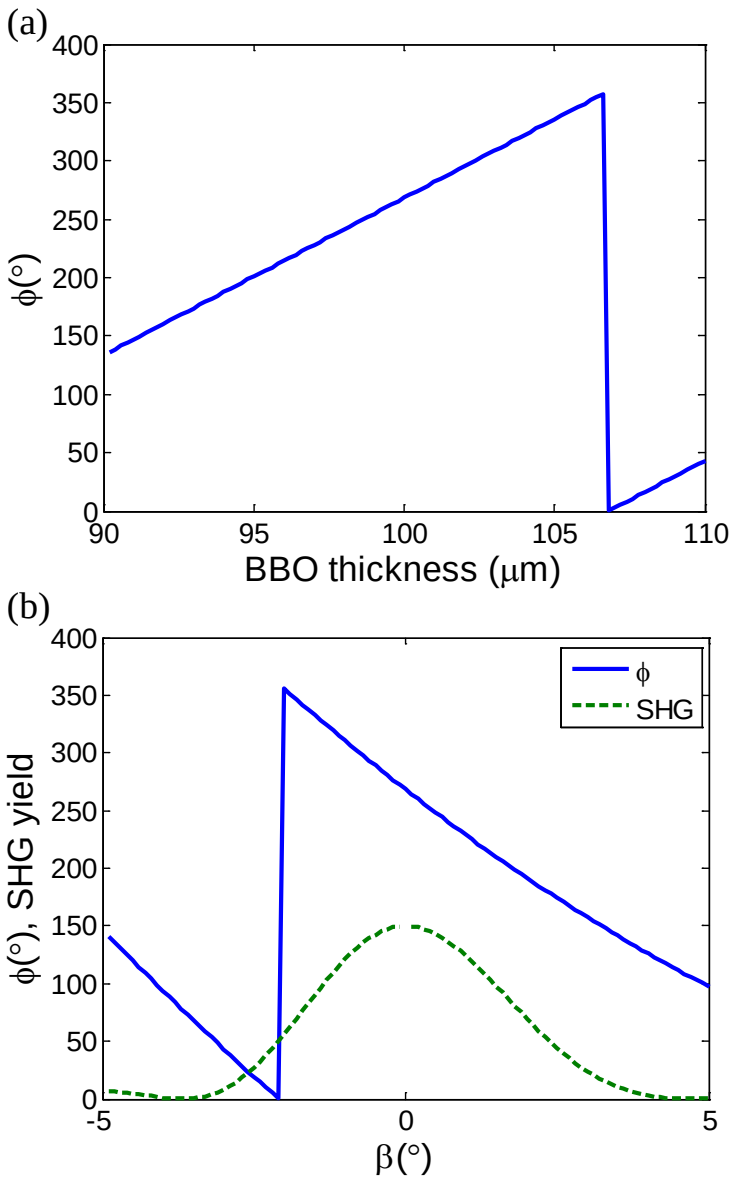

Figure 2.9 Simulated φ value (blue line) as a function of (a) the BBO effective thickness in μm and (b) β in degrees. Co-plotted in (b) is the second harmonic intensity (green dashed line) produced by type-I phase-matching as a function of β.

Figure 2.9 shows how φ changes with the effective BBO thickness l or β under our experimental condition. In general, controlling φ by titling the BBO angle (β) is practically limited as it simultaneously affects the phase-matching condition in second harmonic generation. For example, Figure 2.9(b) shows the second harmonic intensity (green line) as a function of β. If β deviates more than $\pm 2^{\circ}$, the second harmonic conversion efficiency drops significantly, ultimately reducing THz output power. This limits the achievable φ value as $\pi < \varphi < 2\pi$ (or equivalently $0 < \varphi < \pi$), which is just good for a full control of φ but this naturally drops the THz output energy when the optimal β approaches $\pm 2^{\circ}$. This, however, can be overcome, if an optical waveplate is inserted before the BBO crystal and adjusted to control the tilt angle β separately. In addition, Figure 2.9(b) shows that the initial value of φ is ~268°

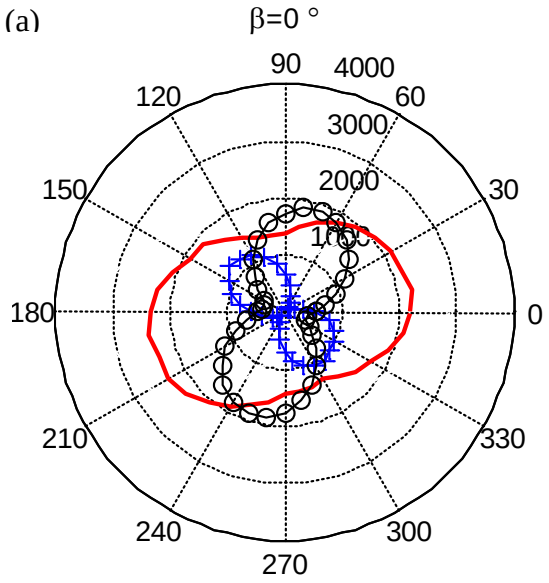

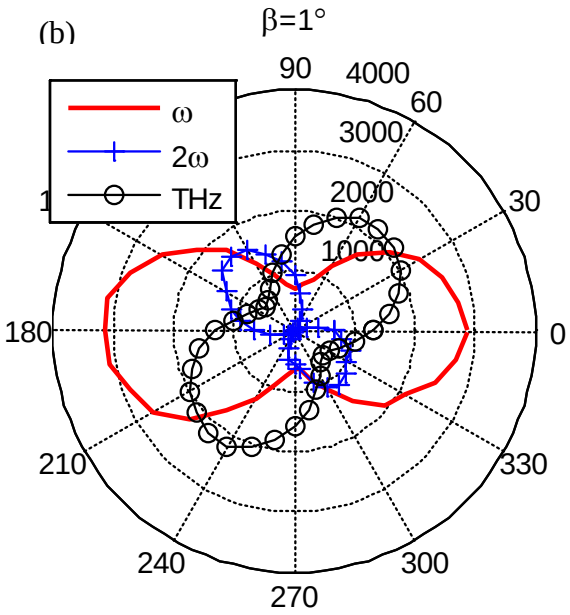

Figure 2.10 Fundamental (ω, red line), second harmonic (2ω, blue line with +), and THz (black line with circles) polarization maps obtained with rotating the polarization analyzer at $\beta = 0^{\circ}$ (a) and 1° (b). Unlike 2ω, ω polarization is depending on the tilt angle β.

Figure 2.10 shows fundamental (ω, red line), second harmonic (2ω, blue line with +), and THz (black line with circles) polarization maps obtained while rotating the THz polarizer in front of the detector with two different angles $\beta = 0^{\circ}$ and 1°. In this test, $\alpha \approx 55^{\circ}$ is selected and fixed. The polarization of fundamental is rotating as β changes from 0° to 1° and thus THz polarization also rotates. The results suggest that THz yield and polarization are highly depending on BBO crystal condition such as azimuthal angle and tilting angle as we predicted from the 2-D simulation.

2.3.3 Plasma filament length effect on THz yields

The 2-D plasma current model described in Sec. 2.2 predicts linear THz polarization, but circular or elliptically polarized THz radiation is often observed experimentally. For instance, the polarization map shown in Fig. 2.10 indicates the THz wave is not perfectly linearly polarized but rather elliptically polarized. We believe this occurs because the transverse plasma current (thus THz polarization) direction gradually rotates with varying θ along the plasma filament (recall θ varies with d). Thus, the THz pulse produced at each point along the filament has different linear polarization and arrives at different times on the detection plane. Because the THz velocity is faster than the optical group velocity, the THz pulse produced at the entrance of filament arrives earlier than that produced at the end of filament [60]. In addition, there is an instantaneous cross Kerr effect between ω and 2ω pulses occurring along the filament, which also rotates the plasma current and THz radiation direction. These two effects can produce elliptically or circularly THz polarization.

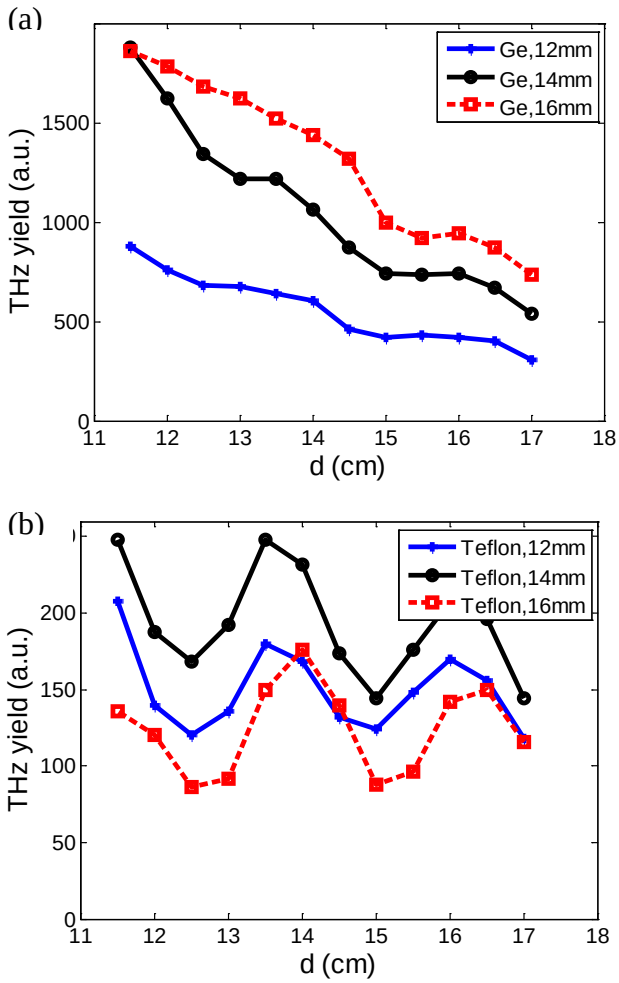

Figure 2.11 THz emission as a function of the BBO-to-plasma distance *d* with three different plasma lengths, 12 mm (line with +), 14 mm (line with circles), and 16 mm (line with squares) with (a) the Ge filter for high frequency (<10 THz) detection and (b) the Teflon filter for low frequency (0.1 ~ 3 THz) detection.

Figure 2.11 shows the total THz yield with increasing *d* for three different plasma lengths, 12 mm, 14 mm, and 16 mm with two different filter sets: (a) Ge (<10 THz) and (b) Teflon (0.1~3 THz) [6,7]. Here, the filament length is adjusted by titling the lens normal angle as shown in Fig. 2.5. At both high and low THz frequencies, the longer the filament is, the more intense THz generation is produced as shown in Figs. 2.11. This implies that tilt-induced aberration increases the laser

spot size, possibly dropping the laser intensity in the filament, but its effect appears less significant compared to the plasma volume (length and/or radius) effect on THz generation. Here, the maximum enhancement factor is ~2.8 for the high THz frequency case. However, in the low THz case, the enhancement factor is ~1.4, and the yield even drops when the filament length reaches ~16 mm [Fig. 2.11(b)]. This is attributed to THz absorption in the plasma filament. It was previously shown that low frequency THz components start to saturate earlier than the higher frequency components [48]. We also note that the θ dependence is more dramatic with the low THz frequency case. We speculate that this may be attributed to certain effects which are not included in our model. For simplicity, we ignore many effects in filamentation, which include collective plasma oscillations, electron-ion and electron-neutral collisional effects, rescattering with parent ions, and any propagation effects [50] including self- and cross-phase modulation, spectral shifting and broadening, Kerr-induced polarization rotation, phase- and group velocity walk-off between two-color fields. In particular, plasma oscillations and collisional effects greatly influence the low frequency components of THz radiation initially produced by plasma currents [61] .

2.3.4 Study on the effect of the laser pulse duration

As a supplementary study, the dependence of THz yields on input laser pulse durations is discussed in this section.

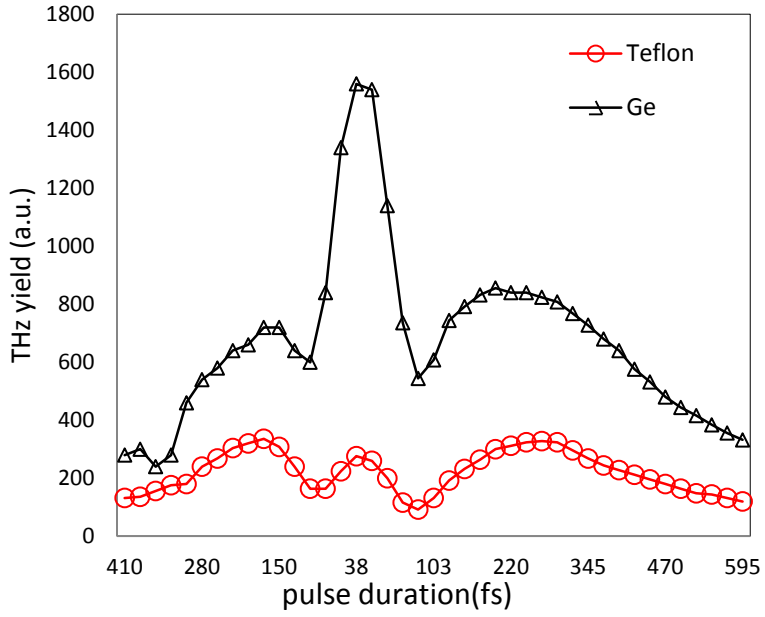

Figure 2.12 THz yield measurement as a function of input laser pulse durations with Teflon and Ge filters placed in front of the pyroelectric detector.

Figure 2.12 shows the output THz yield as a function of input laser pulse durations. Here the laser pulse duration is adjusted by detuning the laser compressor and measured with a homemade single-shot autocorrelator. It shows that for high frequency THz radiation, the signal peaks with the shortest pulse duration <40 fs and there are two more peaks occurring at negatively chirped 150 fs and at positively chirped 220 fs. However, for low THz frequencies, the peak at ~38 fs substantially drops, exhibiting three equivalent peaks. This trend is different from the previous report by Wang *et al*. [62]. This interesting three-peak feature may be explained in the plasma current model by including chirp-dependent second harmonic generation in the BBO crystal and plasma current generation.

2.4 Conclusion

In this chapter, we describe the mechanism of 2-D plasma current generation and optimization of THz radiation in two-color photoionization. This is done by controlling the relative phase θ, BBO azimuth angle α, and tilt angle β. We show that these parameters can control many laser-THz properties including the laser (ω and 2ω) amplitudes, ellipticity of ω, phase retardation φ, phase delay θ, polarization and the intensity of THz, all consistent with our 2-D photocurrent model. Furthermore, we measure the THz yield dependence on the filament length. All these results verify the sensitivity of control parameters in generating intense THz radiation and will motivate further investigations. In addition, our semiclassical approach needs to be replaced by full quantum mechanical calculations, in particular when the quasi-static tunneling ionization regime becomes inapplicable [63].

Chapter 3 : High power terahertz generation in two-color laser produced plasmas: THz yield scaling and saturation

3.1 Introduction to high power THz generation

Terahertz (THz) generation by two-color laser mixing in air plasma has attracted a considerable amount of interest owing to its capability of producing ultra-broadband and high-power THz pulses [30–54]. In this schematic, the fundamental and second harmonic of an ultrashort pulsed laser are combined to ionize air molecules at the focus, which produces an intense THz pulse in the far field.

Microscopically, this process originates from tunnel-ionized electrons moving in a non-symmetric two-color laser field. This creates a subpicosecond directional current surge with concurrent THz radiation [47–49]. Femtosecond laser pulses can create filaments ranging from a few centimeters to meters due to dynamic balancing between Kerr-induced laser self-focusing in air and plasma-induced defocusing [64–68]. In this regime, macroscopic phase-matching becomes crucial for efficient THz generation. Recently, off-axis phase-matched THz generation was demonstrated with ~70 mm long filamentation, and its mechanism is understood in the context of off-axis constructive interference between the local THz waves emitted along the filament [52].

At the same time, it is of great interest to understand what limits THz output energy and how the yield can be optimized. In the previous chapter, we studied how laser parameters such as phase, amplitude, polarization, and ellipticity affect the

resulting THz yield [51]. In this chapter, we re-examine THz energy scaling and saturation in two-color filamentation with laser energies up to 60 mJ. In particular, we investigate laser energy coupling into filaments under various external focusing conditions, ultimately addressing a mechanism leading to THz yield saturation.

3.2 Experimental setup

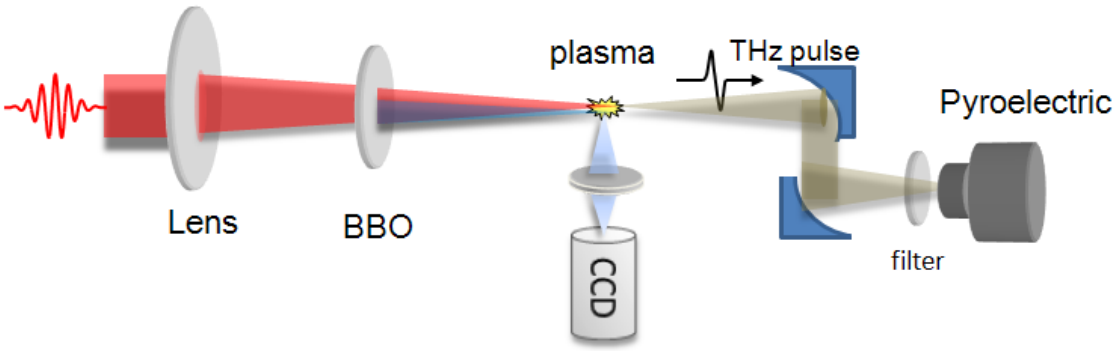

Figure 3.1 Schematic of experimental setup. A pyroelectric detector with various filters detects THz and transverse imaging with a CCD camera monitoring filament fluorescence.

Figure 3.1 shows a schematic experimental setup for THz saturation study. A Ti:sapphire laser system which is capable of delivering 800 nm, ~70 mJ, 50 fs pulses at a 10 Hz repetition rate is used to generate THz radiation. Various neutral density (ND) filters are placed before the grating compressor in the laser system to control the laser pulse energy. The laser pulse is focused by a lens with focal length of f = 150 mm, 200 mm, 250 mm, 1.0 m, 1.5 m, or ~4 m, and then propagates through a 0.1-mm thick BBO crystal (type-I) which generates a second harmonic. The fundamental and second harmonic pulses co-propagate and create a plasma filament at the focus,

generating THz radiation. Then the optical pulses are blocked by a 5-mm thick silicon (Si) wafer, while the generated THz radiation is being collected and focused by two off-axis parabolic mirrors into a 2 mm or 9 mm pyroelectric sensor (SPI-A-62THZ, Spectrum detector Inc., QS9-THZ-BL, Gentec-EO Inc). For f = 1.0 m, 1.5 m, and 4.0 m focusing, a parabolic mirror with 20 cm diameter was used to collect and detect THz radiation. To detect different THz frequency ranges, an additional 1.5-mm thick Teflon (<3 THz), 1.5-mm thick high-density polyethylene (HDPE), or 2-mm thick germanium filter (<10 THz) is placed in front of the pyroelectric detector. A transverse optical imaging setup consisting of a lens, a color filter, and a charge coupled device (CCD) camera is also used to measure the plasma filament length and fluorescence (see Fig. 3.1 bottom).

3.3 Results and discussion

3.3.1 Short filament experiments

Figure 3.2 shows the measurements of the pyroeletric signal (THz yields) for a relative short filament (under 2 cm) as a function of increasing laser input energy. We use three different focal lens, (a) f = 150 mm, (b) f = 200 mm, and (c) f = 250 mm. In all cases, the THz output generally increases with laser energy in the low input energy regime. However, as the laser energy further increases, the output soon saturates and even decreases in certain cases. In addition, it shows different saturation curves for different focusing geometry. For instance, with f = 150 mm focusing, the yield starts saturating at ~35 mJ. With f = 200 mm, it saturates at ~45 mJ. With f = 250 mm, the signal continuously increases up to ~55 mJ, yielding more THz output energy compared to the shorter focusing cases. The maximum THz energy is 0.2 μJ, 0.5 μJ, and, 0.8 μJ, with f = 150 mm, 200 mm, and 250 mm focusing, respectively. This shows the THz generation efficiency is greatly sensitive to the focal length of the lens, which is consistent with the previous observation [42].

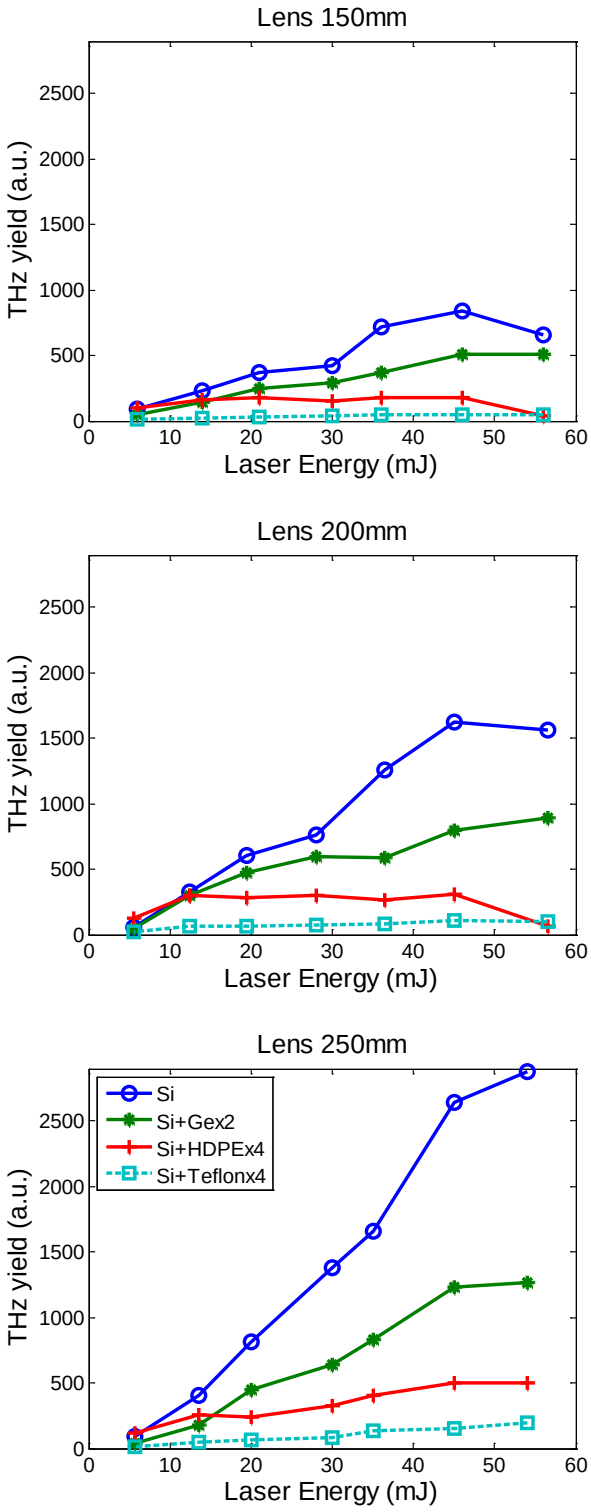

Figure 3.2 THz energy measurement (Pyroelectric detector signal) with various THz filters (Si, Ge, HDPE , or Teflon) as a function of input laser energy with three different focusing lenses: 150 mm, 200 mm and 250mm.

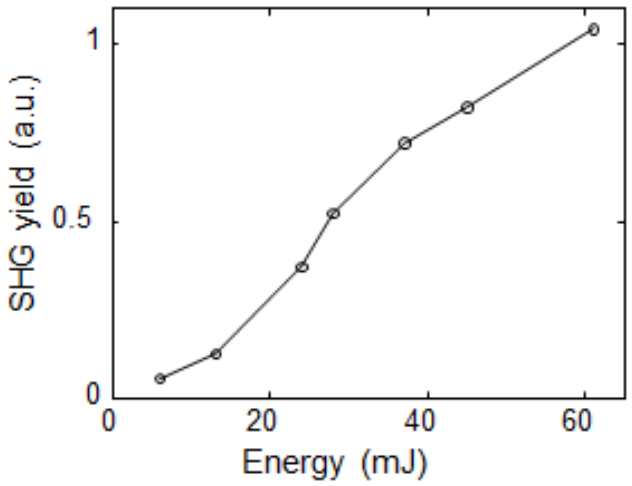

Figure 3.3 Second harmonic generation (SHG) from the 100 μm thick BBO crystal pumped by 800 nm laser.

Here, we note the observed THz saturation is not correlated with the SHG process occurring in the BBO crystal. Figure 3.3 shows the second harmonic generation (SHG) from a 100 μm thick BBO crystal. It shows an almost linear second harmonic yield even with high laser energy.

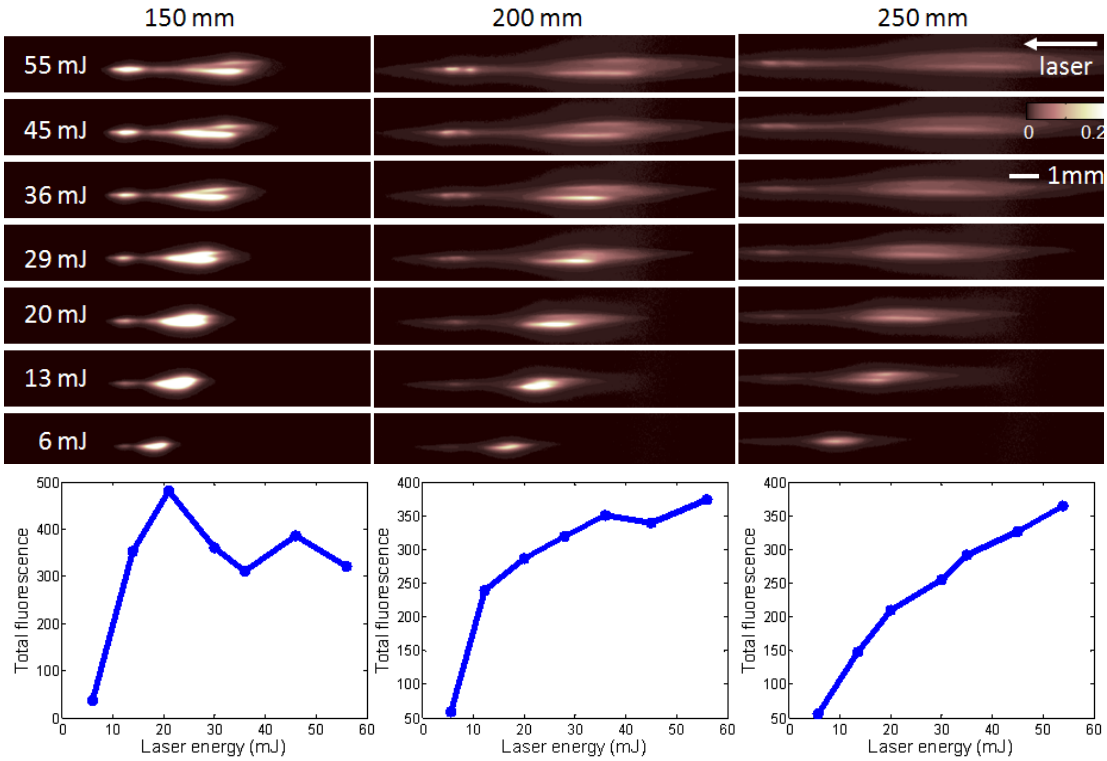

Figure 3.4 Filament fluorescence imaged by a CCD with increasing laser energy. Laser pulses enter from right to left. (Bottom) Total fluorescence intensity versus input laser energy with three focusing lenses, 150 mm, 200 mm and 250 mm.

Figure 3.4 shows filament fluorescence images as a function of laser energy obtained with different focusing lenses, 150 mm, 200 mm, and 250 mm. The bottom row shows the total fluorescence intensity integrated over the entire region of interest as a function of laser input energy. By analyzing the filament fluorescence images, we can study how the THz saturation is connected to the input laser energy and/or lens focal length conditions. Although it does not directly measure the electron densities or laser intensities, the filament fluorescence provides information as to how the laser pulse propagates with different lens-focusing and how its energy is coupled into plasma [59] [69]

.

In the low laser energy regime, it shows that filaments are formed at very close to the vacuum focus of the lens. However, with increasing laser energy, the filaments start appearing well before the vacuum focus due to Kerr-induced self-focusing in air (moving to the right in the figures), also increasing their lengths. In this filamentation regime, self-focusing and plasma-induced defocusing play important roles in extending the filament length and simultaneously preventing the laser from reaching higher intensities [64–67] [70].

The bottom figures show the total fluorescence intensity integrated over the entire frame as a function of laser input energy. Interestingly, with the short focal lenses (150 mm and 200 mm), the measured fluorescence intensity strongly saturates. Overall, the trend matches well with the THz yield curves shown in Fig. 3.2. This indicates the saturation in THz generation is strongly correlated with the plasma filament condition. In the case of short focusing geometry (f =150 mm), a dense plasma is formed and strongly defocuses the high-energy laser pulse, which is evident from the saturated fluorescence signal. Here the laser energy is not effectively coupled into plasma, which results in less THz emission. This is why THz output strongly saturates with increasing laser input energy.

3.3.2 Long filament experiments

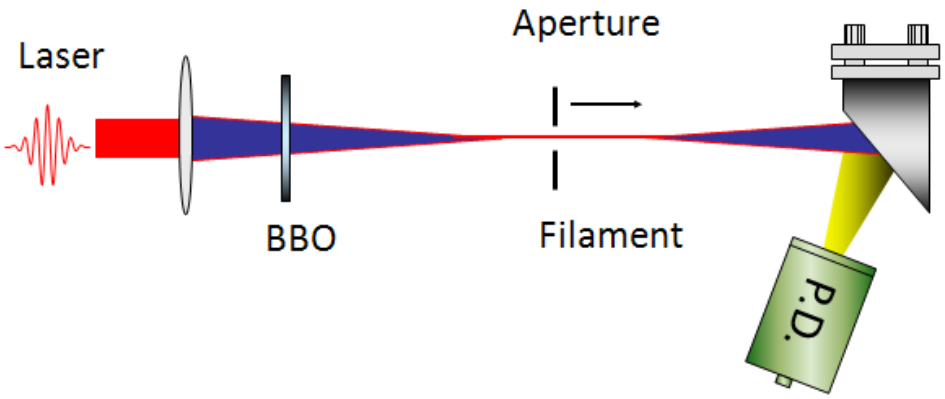

Figure 3.5 Long filamentation experiment with pyroelectric detection. A ~3 mm diameter aperture is placed and scanned to control the effective filament length

To avoid ionization-induced defocusing with high input laser energy, we re-distribute the incoming laser energy over elongated plasma with weak focusing. Figure 3.5 shows a modified experiment setup for long filamentation. We use the same laser system, the amplified Ti:sapphire laser delivering 800 nm, 60 mJ (fixed), 50 fs pulses at a 10 Hz repetition rate. The femtosecond laser pulses are focused by a long focal length lens, f = 1.0 m, 1.5 m, or ~4 m. Here the effective filament length, l_{eff}, is controlled by scanning a ~3 mm diameter aperture, along the filament direction. It blocks the THz radiation emitted prior to the aperture (left side of the aperture in Fig. 3.5), while the THz waves generated behind the aperture (right side of the aperture) are collected and focused into the detector [52] . Due to the long filament length reaching up to 40 cm, a 20 cm size parabolic mirror is placed to collect and detect THz radiation. Here a 9 mm pyroelectric sensor (QS9-THZ-BL, Gentec-EO Inc) is used for THz detection.

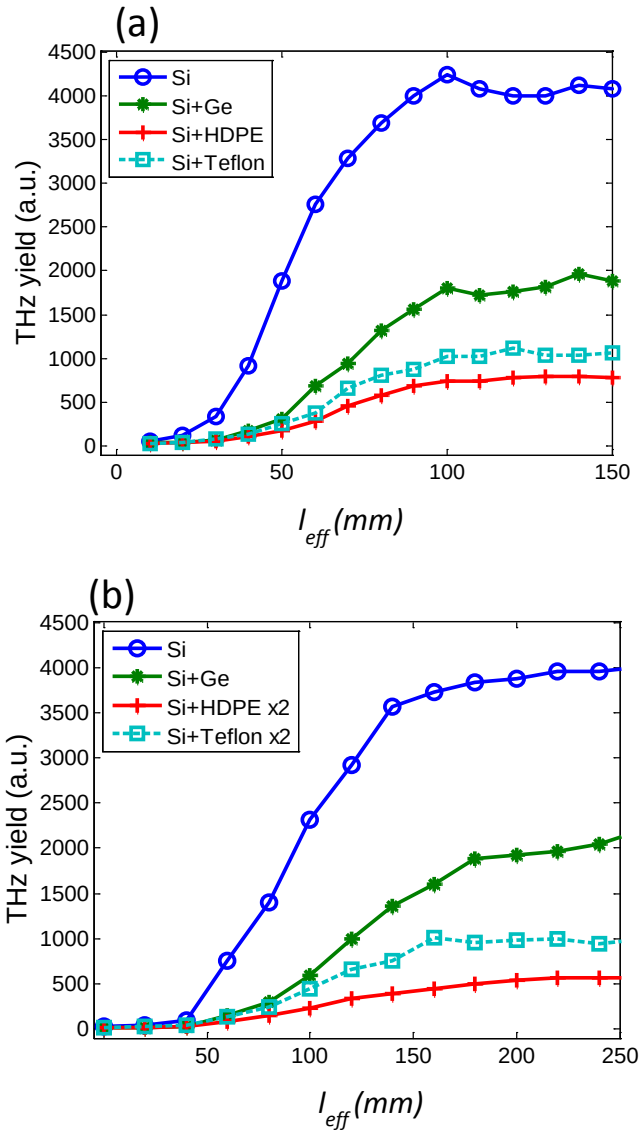
(a)
Si
Si+Ge
Si+HDPE
Si+Teflon
THz yield (a.u.)
4500
4000
3500
3000
2500
2000
1500
1000
500
0
0
50
100
150
l_{eff}(mm)
(b)
Si
Si+Ge
Si+HDPE x2
Si+Teflon x2
THz yield (a.u.)
4500
4000
3500
3000
2500
2000
1500
1000
500
0
50
100
150
200
250
l_{eff}(mm)

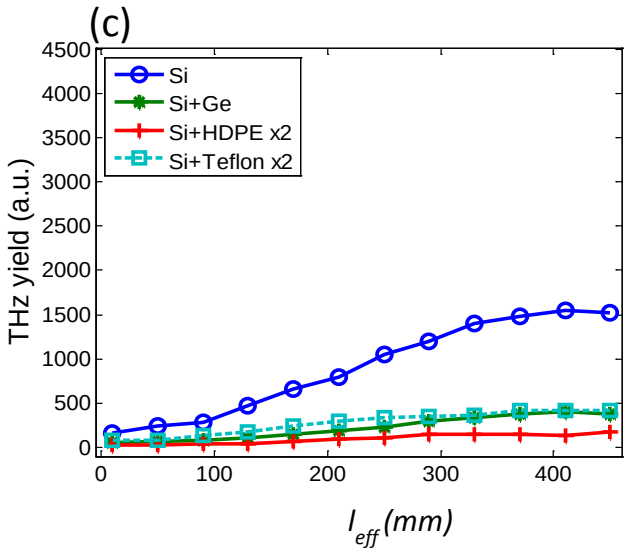

Figure 3.6 THz yield scaling as a function of the effective filament length (l_{eff}) adjusted by a moving pinhole along the filament with lens focusing of (a) 1 m, (b) 1.5 m, and (c) ~4 m (obtained with a combination of two lenses).

Figure 3.6 shows the measured THz yield as a function of the effective filament length, l_{eff}, with f = (a) 1 m, (b) 1.5 m, and (c) ~4 m lens focusing with fixed input laser energy, 60 mJ. It shows that the THz output increases over hundreds of millimeters until it saturates at 100 mm, 150 mm, and 400 mm with f = 1 m, 1.5 m, and 4 m focusing, respectively. In the case of f = 4 m, the yield continuously increases up to 400 mm. This strongly supports the off-axis THz phase-matching mechanism in two-color filamentation, in which the total THz yield continuously increases with the filament length, well beyond the dispersion-induced dephasing length (~22 mm) [52]. However, when the filament is elongated too much, the maximum achievable THz energy decreases because the laser intensity drops well below the clamped level in extremely weak focusing. In addition, we observe that the THz yield with Si and HDPE filtering is always greater than that with Si and Teflon

filtering in the short focusing cases (see Fig. 3.2), but the trend reverses in the longer focusing (see Fig. 3.6). This is because we used a different parabolic mirror with a 10-mm diameter hole, in addition to a different pyroelectric sensor (QS9-THZ-BL, Gentec-EO Inc) for the longer focusing. Because of the hole, a small fraction of higher frequency components were not collected effectively.

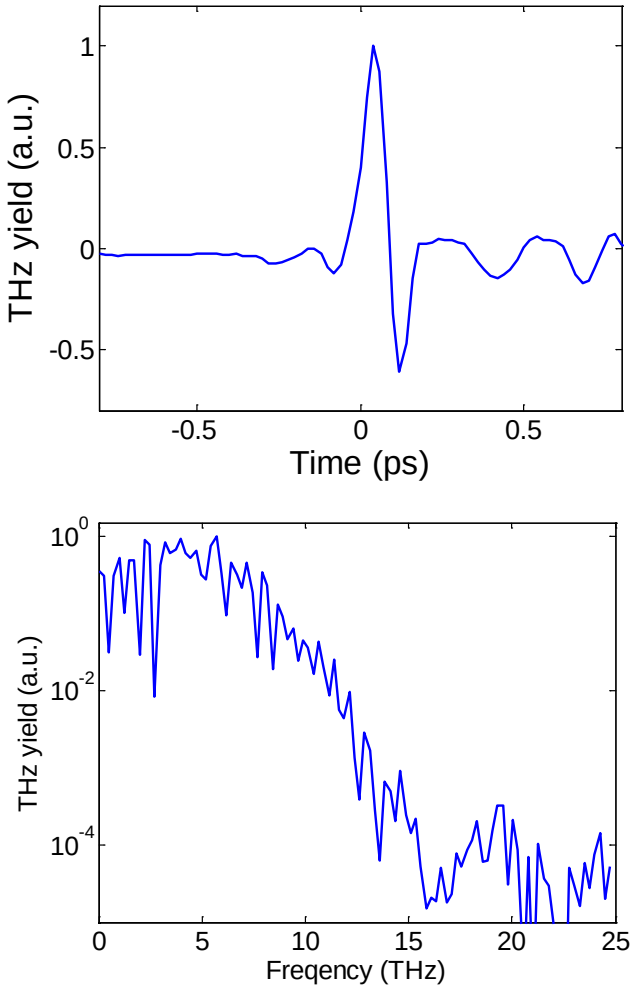

Figure 3.7 Measured THz waveform and its corresponding spectrum measured via air-based coherent detection (ABCD) [45] with f = 150 mm and laser energy of ~15 mJ.

Figure 3.2 shows additional experimental data showing the THz waveform and spectrum measured by an electric field induced second harmonic technique [20].

Figure 3.7(b) shows that two-color laser mixing in air can provide >10 THz bandwidth. Under our experimental condition ($E \leq 60$ mJ), the optimal focusing occurs for $f = 1$ m. The maximum achieved THz energy is 7 μJ per pulse yielding conversion efficiency of 0.012%, very close to that achieved with much lower laser energy [55]. In particular, the measured energy is ~40 times larger compared to the $f = 150$ mm focusing case. However elongated filamentation results in increasing the spot size of THz radiation when refocused by parabolic mirrors alone. In this case, the focused spot radius scales as $R \sim l_f \tan(\Theta_p)$, where l_f is the filament length, Θ_p is the off-axis phase matching angle given by $\cos\left(\Theta_p\right) = 1 - \Gamma/(2l_d)$. Here, l_d is the dephasing length, over which the two-color phase difference changes from 0 to π [52], and Γ is the THz wavelength. For a ~7 cm long filament, the focused spot size is measured to be 1.5 mm at 1~3 THz [52]. This refocusing problem, however, can be improved by collecting THz radiation with an axicon lens or mirror, and then focusing with an off-axis parabolic mirror. In this scheme, the focused THz field may reach ~50 MV/cm with 2× diffraction limited focusing at 10 THz, along with its ultrashort (<0.1 ps) waveform (see Fig. 3.7).

3.4 Conclusion

In this chapter, we observe and explain the THz saturation effect in two-color laser filamentation. This saturation occurs mainly due to ionization-induced defocusing and laser intensity clamping in filamentation. In tight focusing geometries, this results in an ineffective coupling of laser energy into the plasma. To minimize such effects and thus improve the THz conversion efficiency, one can distribute the laser energy over a longer filament.

Chapter 4 Intense terahertz generation in two-color laser filamentation: energy scaling with terawatt laser system

4.1 Introduction

Strong terahertz (THz) pulse generation via two-color laser mixing in air has attracted considerable attention for ultrafast THz studies including broadband THz time domain spectroscopy, THz imaging, and nonlinear THz studies [30–54]. In this two-color scheme, an ultrashort laser's fundamental and its second harmonic pulses are focused in air (or any gas) to create a gaseous plasma via multiphoton/tunneling ionization. This emits a THz pulse in the forward direction. Compared to solid-sate THz sources such as photoconduction in semiconductors [24,26] or optical rectification in nonlinear crystals [29,71–73], two-color laser mixing provides intense, broadband THz pulse [30]. In particular, optical rectification in lithium niobate ($LiNbO_3$) crystals with tilted pulse front excitation provides extremely high THz energy (current record 125 μJ), but the radiation spectrum is mostly limited to <1.5 THz [29]. By contrast, two-color laser mixing is reported to provide ultra-broadband radiation up to 200 THz [30] as well as down to extremely low frequency radiation (<0.01 THz) [48]. Basically, this produces electromagnetic (EM) radiation ranging from radio-microwave to near infrared frequencies. This provides an attractive characteristic for broadband spectroscopic studies.

Microscopically, THz radiation in two-color mixing originates from ultrafast plasma current generation during tunneling ionization [47–50] although there is still

a debate on the mechanism. Besides this microscopic picture, equally important is the macroscopic laser-THz propagation effect. This is strongly coupled with femtosecond laser filamentation in air. In general, filamentation occurs due to dynamic balancing between Kerr-induced beam self-focusing and ionization-induced beam defocusing [64–67]. This results in a long filament ranging from a few centimeters to several meters depending on the laser and gas parameters. This filamentation naturally governs the macroscopic process of THz generation, making the two-color mixing phenomenon more complex. Practically, this macroscopic effect determines the far-field radiation profile [52,74], polarization [53], and bandwidth [75], as well as THz energy scaling [48,52].

Previously, an off-axis phase-matching mechanism was proposed and demonstrated to show this macroscopic effect in two-color filamentation [52]. We also showed that a long filament emits conical (donut-shaped) THz radiation peaked at 4–7° off from the forward axis depending the radiation frequency [52] [76]. However, this phase-matching condition was demonstrated for relatively short filaments (<7 cm) with laser energy limited to <5 mJ [52]. In this chapter, we extend the study for much longer filaments with multi-terawatt (TW) laser systems. In particular, we test THz energy scaling in long filamentation (1 cm ~ 60 cm) with 2 TW and 30 TW laser systems. Our scaling law predicts the THz peak power can approach multi gigawatt (GW) by creating about a meter long filament with a 30 TW laser system.

In parallel, we have investigated high-average power THz generation at a 1 kHz repetition rate. For this, we have developed and used a cryogenically-cooled

Ti:sapphire amplifier capable of delivering 15 mJ per pulse at 1 kHz. This produces a high-average-power (>1 mW) THz generation with >50 THz. Further enhancement toward 10 mW average power is also discussed. Finally, we discuss an issue associated with focusing conical THz radiation into a small spot size, which is of great importance for nearly all THz experiments.

4.2 Macroscopic model for THz generation in two-color filamentation

A schematic picture of two-color laser filamentation and simultaneous THz generation is shown in Fig. 4.1. A femtosecond laser pulse (ω) is weakly focused onto a frequency doubling crystal such as beta barium borate (BBO), which generates a second harmonic pulse (2ω). In this in-line scheme, the BBO crystal is often detuned from its optimal angle (ω polarization parallel to the ordinary axis of the crystal) in order to produce a ω-field component parallel to 2ω polarized along the extraordinary axis. In this scheme, ω becomes elliptically polarized after passing through the crystal due to the birefringence in BBO [51]. Alternatively, the BBO crystal can be tuned at the right angle for type-I phase matching, which results in crossed polarization between ω and 2 ω. This polarization state, however, can be converted into co-linear by inserting an ultra-thin, dichroic half-wave plate just after the BBO crystal (not shown in Fig. 4.1). In this way, the two-color laser fields can be linearly polarized in the same direction. Assuming this is the case, the laser field E_L at a point in the filament is expressed as

$$E_L = E_\omega(t)\cos(\omega t) + E_{2\omega}(t)\cos(2\omega t + \theta), \tag{4-1}$$

where $E_{\omega}(t)$ and $E_{2\omega}(t)$ are the amplitudes of the fundamental and the second harmonic fields, respectively, θ is the relative phase between $E_{\omega}(t)$ and $E_{2\omega}(t)$ at a distance d from the starting point of the filament. At the point, tunneling ionization occurs under the combined laser field and a plasma current arises from tunnel-ionized electrons. Here, the local plasma current density is given by [49]

$$J(t) = -\int e v_d(t, t') dN_e(t'), \tag{4-2}$$

where $dN(t')$ is the density of free electrons produced by the laser field in the interval between t' and $t' + dt'$, and $v_d(t, t')$ is the drift velocity of those electrons at t. An ultrafast current surge at the point emits THz radiation in all directions, like dipole radiation from a point source, with the far field scaling as $E_{\mathrm{THz}} \propto dJ(t)/dt$. In the classical plasma current model, the far-field THz radiation peaks at $\theta = \pm\pi/2$, while minimal THz radiation occurs at $\theta = 0$ [47]. The described plasma current model is also confirmed by numerical simulations [77].

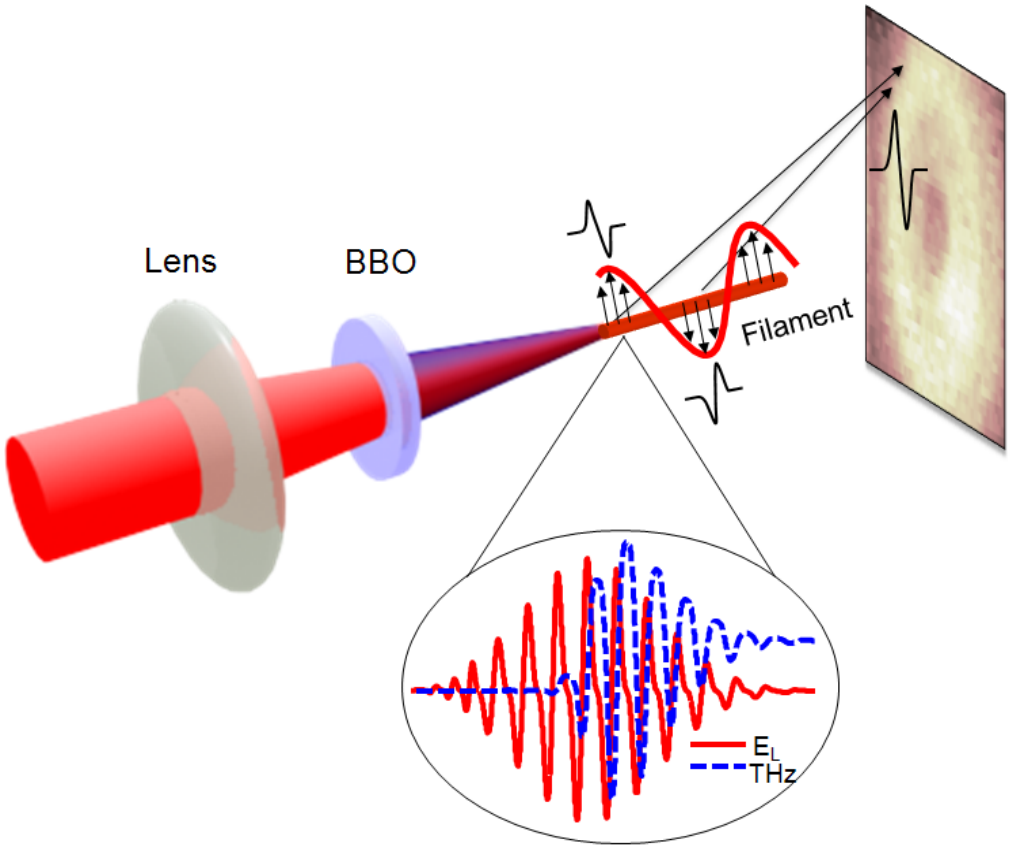

Figure 4.1 . Schematic of THz generation in two-color, femtosecond, laser filamentation in air. A microscopic plasma current (blue dotted line), produced by the two-color electric field (red solid line) via tunneling ionization, emits THz radiation in all directions. However, the far-field THz radiation profile shown on the detection plane is determined by macroscopic interference between the THz waves emitted from the local THz sources distributed along the filament. This provides an off-axis phase-matching condition, yielding conical THz radiation profiles. This macroscopic propagation effect also broadens the two-color laser and THz spectra via self-phase modulation and ionization-induced spectral blueshifts.

The relative phase θ between the two-color laser fields, however, changes along the filament as,

$$\theta = \omega(n_\omega - n_{2\omega})d / c + \theta_0, \tag{4-3}$$

where n_ω and $n_{2\omega}$ is the refractive index of air-plasma filament at ω and 2ω frequency, respectively, c is the speed of light in vacuum, and θ_0 is the initial relative phase at the starting point of the filament. Here, the refractive index of weakly-ionized (Ne << Nc) air filament [78] is given by $n_{\text{filament}} = n_{\text{air}} + \Delta n_{\text{plasma}} + \Delta n_{\text{Kerr}}$, where $\Delta n_{plasma} \approx -\frac{1}{2}\left(N_e/N_c\right)\left(1+i\nu/\omega\right)^{-1}$, N_e is the electron density, N_c is the critical density, and ν is the electron-ion collisional frequency which is negligible for the electron density of our interest ($\nu << \omega$). Because of this filament dispersion, the relative phase θ changes from 0 to π over a distance l_d, where $l_d = \left(\lambda/2\right)\left(n_\omega - n_{2\omega}\right)^{-1}$ is the dephasing length for ω and 2ω. Here, λ is the optical wavelength at ω. For pure (no plasma) atmospheric air (~10^{19} cm^{-3}), l_d = 25 mm at λ = 800 nm. For a filament with electron density of N_e = 10^{16} cm^{-3} in atmospheric air, l_d = 22 mm. As this relative phase varies along the filament, the local THz amplitude and polarity also changes along the filament as shown in Fig. 4.1 (note the red oscillating curve along the filament). Because of this oscillating THz source polarity, far-field THz radiation is not simply emitted in the forward direction [79].

In general, the THz far field, $E(r, \Omega)$, is obtained by integrating the contributions from all source points distributed along the filament as [52],

$$E(\mathbf{r},\Omega) \propto \int_V d^3\mathbf{r}' \frac{\tilde{P}\left(\mathbf{r}',\Omega\right)e^{i\,k_{THz}|\mathbf{r}-\mathbf{r}'|}}{\left|\mathbf{r}-\mathbf{r}'\right|}, \tag{4-4}$$

where $\tilde{P}\left(\mathbf{r}',\Omega\right) \propto \tilde{A}\left(\mathbf{r}',\Omega\right)\sin\left(\theta(z')\right)\exp\left(in_g k_{THz} z' - i\Omega t\right)$ is the nonlinear THz polarization, $\tilde{A} \propto dJ(\mathbf{r}',\Omega)/dt$ is the local THz amplitude at frequency Ω, determined by the microscopic plasma current model [47–49]. At a distance far longer the filament length ($|\mathbf{r} - \mathbf{r}'| >> |\mathbf{r}'|$), the far-field THz intensity profile is approximated as [52],

$$\left|E\left(r,\Theta,\Omega\right)\right|^2 \propto \left|\tilde{A}\left(\mathbf{r}',\Omega\right)\right|^2 \frac{(\pi a^2)^2 l^2}{r^2}\left(\kappa_1^2 + \kappa_2^2 + 2\kappa_1\kappa_2\cos\left(2\theta_0 + \pi\right)\right)\left(\frac{2J_1(\beta)}{\beta}\right)^2, \tag{4-5}$$

where $\kappa_{1,2} = \sin(\alpha_{1,2})/\alpha_{1,2}$, $\alpha_{1,2} = k_{THz} l\left[n_g \pm \Gamma/(2l_d) - \cos(\Theta)\right]/2$, $\beta = 2\pi a \lambda^{-1}\sin(\Theta)$, Γ is the THz wavelength, and the last term in Eq. (4-5) represents circular diffraction. The third term in Eq. (4-5) provides a phase-matching condition for efficient THz generation. Here, maximum THz generation is achieved with $\alpha_{1,2} = 0$. This provides the angle for phase matching, Θ_p, given by $\cos\left(\Theta_p\right) = 1 - \Gamma/(2l_d)$ for weakly ionized plasma filaments ($n_g \approx 1$). The phase matching angle Θ_p can be also obtained from the condition necessary for constructive interference between two oppositely-polarized THz waves as shown in Fig. 4.1. This condition is satisfied when the path length difference becomes $\Gamma/2$, which provides the same phase matching angle. For example, a filament length of l = 70 mm, 1 THz radiation (Γ = 300 μm) peaks at $\Theta \sim 7°$ with a conical radiation profile as shown in Fig. 4.1.

The total THz yield obtained from the entire filament length is given by, $\int \left|E\left(r,\Theta,\Omega\right)\right|^2 \sin\Theta d\Theta$. This scales quasi-linearly with the filament length [52]. This implies that we can enhance the THz energy output by increasing the filament length while maintaining the local THz strengths is same. This condition remains valid for multi-filamentation. For example, two filaments separated by *d* (on the order of hundreds of micrometers) in the transverse direction would produce THz waves in phase and those two waves interfere destructively in the far field at an angle of $\theta_d = \sin^{-1}(\Gamma/(2d))$. Compared with the phase matching angle, $\Theta_p = \cos^{-1}(1-\Gamma/(2l_d))$, θ_d at which destructive interference occurs due to multi-filamentation is much greater than the phase matching angle Θ_d because of $d << l_d$. Thus multi-filamentation plays little or no role in determining the far-field THz radiation profile. The total plasma volume, however, will contribute to the output THz yield.

4.3 Results: THz energy scaling with high power laser systems

4.3.1 THz energy scaling with a 2 TW laser operating at 10 Hz

A 2 TW Ti:sapphire laser system capable of delivering 800 nm, 100 mJ, 50 fs pulses at a 10 Hz repetition rate is used for THz generation. The experimental setup is shown in Fig. 4.2(a). In addition to far-field THz measurements, a 5-mm-diameter, single-loop wire (B-dot probe) is used to monitor the near-field, low-frequency THz waveforms. Basically, this can probe the local THz amplitudes and polarities. Previously, it was shown that the B-dot signal is strongly correlated with far-field THz radiation [48].

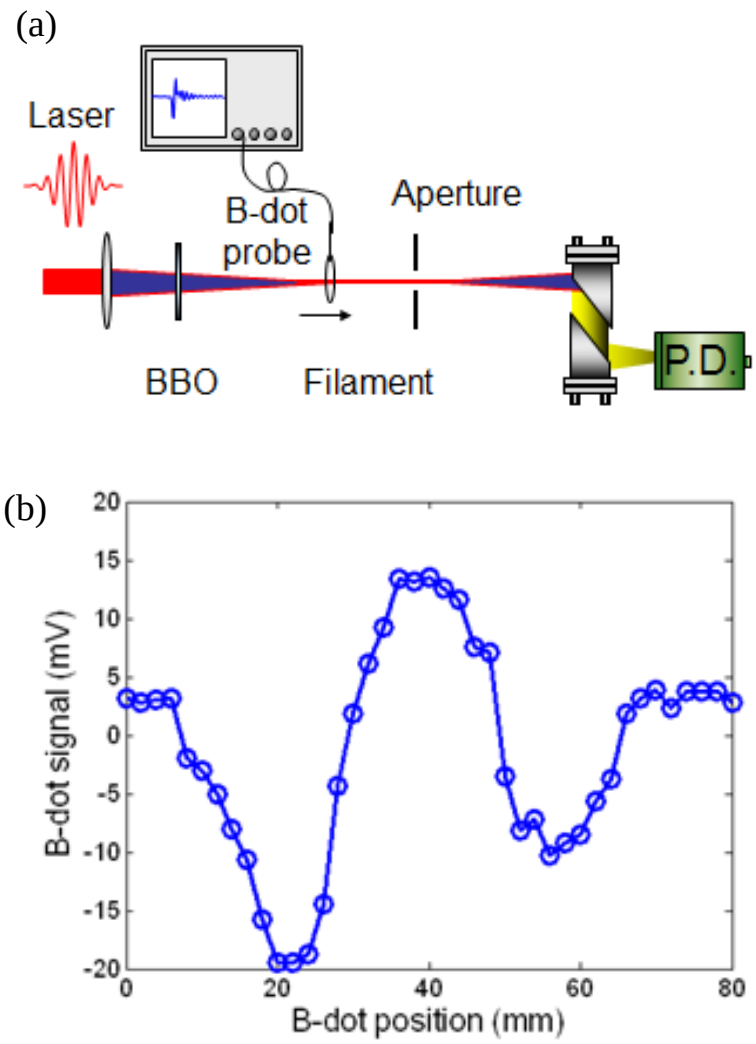

Figure 4.2 (a) Experimental setup for B-dot probe and THz energy measurements. (b) Peak-to-peak B-dot signal as a function of its position *d* along the plasma filament.

For B-dot measurements, ~50 mJ of laser energy is used to create >300 mm long filaments with f = 2 m focusing. A 0.1-mm thick BBO crystal (type-I) is placed in the beam path (~120 mm after the focusing lens) to generate collinear second harmonics. A B-dot probe is placed and scanned in the air plasma filament as shown in Fig. 4.2(a). A 0.5 GHz, 5 giga-sample/s oscilloscope is used to measure the

induced voltage across the ends of the B-dot coil. According to Faraday's law, the induced voltage is given by $V = -\int \dot{\mathbf{B}} \cdot \mathbf{ds}$, where $\dot{\mathbf{B}}$ (B-dot) is the time derivative of magnetic field, which arises from a transient current in the plasma according to Ampere's law, $\nabla \times \dot{\mathbf{B}} = \mu_0 \dot{\mathbf{J}}$. Thus, the induced voltage (B-dot signal) represents the peak rate of electric current change where the probe is located [67]. Here we note that the plasma current, produced by detuned type-I phase matching, is generally elliptical [53]. This has a circular current component along the B-dot loop direction. To observe variations in the local plasma current with increasing filament length, the B-dot probe is scanned along the filament. As shown in Fig. 4.2(b), the B-dot signal (or local THz radiation) indeed oscillates with varying d (or θ) and the oscillation period is estimated to be $l_d \sim 20$ mm. This corresponds to an electron density of $N_e \sim 10^{16}$ cm^{-3}, consistent with other measurements [59,80].

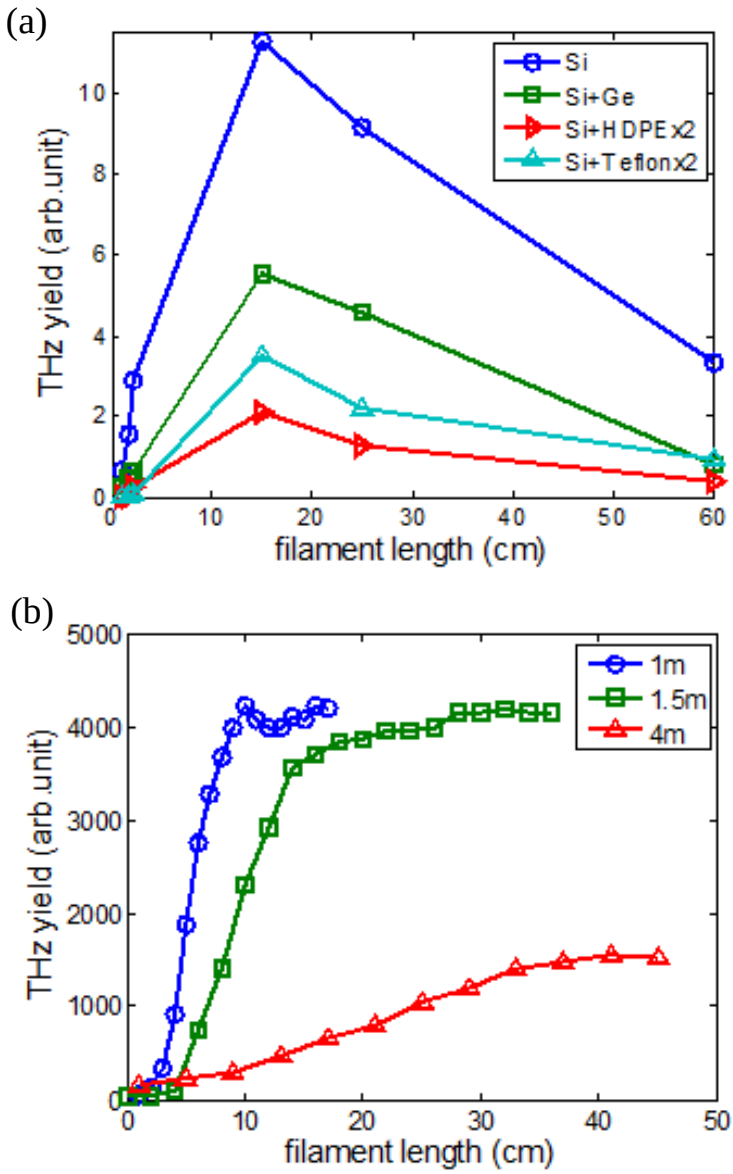

Figure 4.3 (a) THz yield measured with a pyroelectric detector as a function of filament length made with 6 different focal length lenses. Four different transmission filters are used for THz detection at various bands (Si for <20 THz, Ge for <10 THz, HDPE or Teflon for 0.1~3 THz) [7]. For clarity, the yields for HDPE and Teflon are multiplied by a factor of 2. Here, the laser energy is fixed at 60 mJ. The maximum THz energy is 7 μJ obtained with ~10 cm long filamentation. (b) THz yield as a function of the iris position for three filaments produced by f = 1 m, 1.5 m, and 4 m focusing. Here the iris blocks THz radiation emitted before the aperture, which controls the effective filament length.

We also examine THz energy scaling and saturation in two-color filamentation with laser energies up to 60 mJ. In particular, we investigate laser energy coupling into filaments under various external focusing conditions. Figure 4.3(a) shows the THz energy output as a function of the filament length, varied from 1 cm to 60 cm with several focal lengths: f = 15 cm, 20 cm, 25 cm, 100 cm, 150 cm, and 400 cm. Here the THz energy is measured with a pyroelectric detector with various THz filters (Si, Ge, HDPE, and Teflon). A silicon filter is used to block unwanted optical and infrared light. In addition to the Si filter, additional filters are used to characterize THz profiles at different frequency bands: a Germanium wafer is used to detect THz frequencies mostly at <10 THz, whereas a 3-mm thick Teflon window is used as a low pass filter to detect <3 THz. The yield increases with the filament length and peaks at 7 μJ with f = 100 cm focusing. With a focusing lens shorter than 100 cm, the input laser energy is not efficiently absorbed in creating a plasma filament, mainly due to strong ionization-induced defocusing [54]. This leads to laser intensity clamping in filamentation [64–67] and thus sets the maximum laser intensity for THz generation in air. On the other hand, when focused with a lens longer than 100 cm, the laser energy starts to spread out over the filament. This drops the local plasma-current amplitude, consequently yielding less THz radiation. This trend is consistent with the previous report [42] .

We have also changed the effective filament length by scanning a pinhole aperture along the filament as shown in Fig. 4.2(a). The iris blocks the THz emitted before the aperture while not affecting the THz emitted after the aperture. Figure 4.2(b) shows the measured THz energy as a function of the aperture position for

filaments made with three focal length lenses (f = 1 m, 1.5 m, 4 m). It shows that the total THz yield increases with the filament length, confirming off-axis phase-matching up to ~50 cm long filamentation.

4.3.2 THz generation from gaseous and clustered plasmas with a 30 TW, 10 Hz laser

We have also used a 30 TW (35 fs, 1 J) Ti:sapphire laser system for THz generation. Here we have conducted experiments in a vacuum chamber [see Fig. 4.4(a)]. In particular, we have tested gas/cluster jets for THz generation. An off-axis mirror (not shown) was used to focus incoming laser pulses onto elongated (~2 cm long) gas jets. Here, clusters—van der Waals-bonded aggregates of up to ~10^7 atoms—are formed in a condensing supersonic nozzle flow into vacuum [81] . In this experiment, two types of gas species, argon and nitrogen, are used. The emitted THz energy is collected by a parabolic mirror and focused into a pyroelectric detector. A silicon filter is placed in front of the detector.

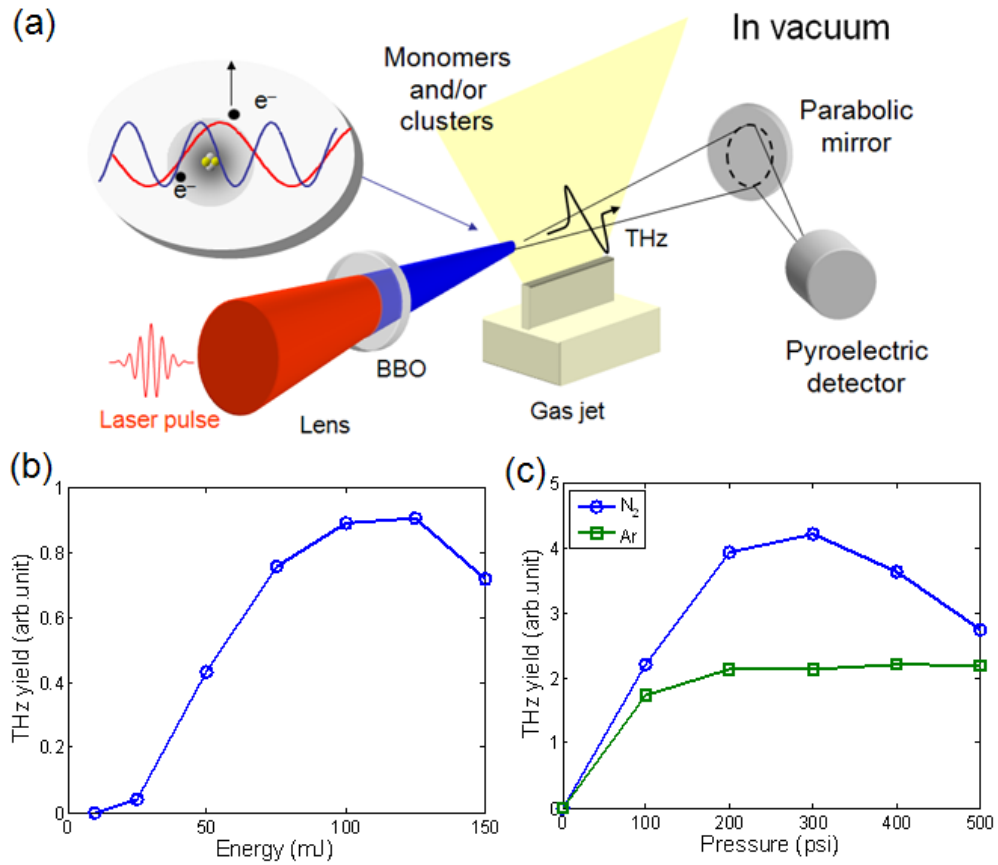

Figure 4.4 (a) Experiment setup for THz radiation from monomers and/or clusters ionized by a femtosecond two-color pulse in a vacuum chamber. Argon clusters are formed in an elongated gas jet via adiabatic expansion of high pressure gas into vacuum. (b) THz yield from gaseous nitrogen jets as a function of laser energy at 200 psi backing pressure. (c) THz yields as a function of nitrogen gas and argon cluster targets with increasing backing gas pressure.

Figure 4.4(b) shows THz output energy for nitrogen at 200 psi backing pressure and room temperature. The output yield increases with laser energy up to 100 mJ but soon drops after 100 mJ. This saturation is attributed to strong THz absorption in dense plasma [48] and/or plasma-induced laser defocusing in filamentation [54] as discussed in Chapter 3. Here, the scaling test was limited to <200 mJ because of severe material damage and strong supercontinuum generation in

the BBO substrate. Overall, the measured THz energy is much weaker than that obtained with the 2 TW laser in long filamentation. This is because the gas jet (or filament) length is limited to ~2 cm. Figure 4.4(c) shows THz yields as a function of gas backing pressure for nitrogen and argon. Both gases show strong saturations with increasing gas pressure, consistent with the previous reports [39,49]. One interesting feature is that argon produces less THz energy compared to nitrogen. This contrasts with the previous result performed for gas-phase targets [36,48], where argon provides a higher THz yield compared to nitrogen. This is because the current argon jets produce many more and larger clusters compared to nitrogen in our experimental condition. This implies that clusters are not an efficient target for THz generation in two-color photoionization. Although a large fraction of laser energy up to 90% can be absorbed in a gas of clusters, the emitted THz radiation may be vastly absorbed by local supercritical clustered plasmas.

4.3.3 High average power THz generation with a 0.5 TW, 15 mJ/pulse, 1 kHz laser

For high-peak and high-average power THz generation, we have developed and used a cryogenically-cooled Ti:sapphire amplifier. Figure 4.5(a) shows a photograph of our amplifier which delivers 800 nm, 15 mJ, 30 fs pulses at a 1 kHz repetition rate. A 6 mJ, ~150 ps (uncompressed) seed pulse from a commercial Ti:sapphire laser system (Legend Elite USX, Coherent Inc.) is amplified to 15 mJ in a 5 mm × 5 mm × 5.5 mm Ti:sapphire crystal pumped by a frequency-doubled (527 nm) Nd:YLF laser (Evolution HE, Coherent Inc.) providing 45 W at 1 kHz. To minimize

thermal lensing in the gain medium caused by high-power pumping, the crystal rod is cooled down to ~60 K with a cryogenic refrigerator (PT-90, Cryomech Inc.). In order to avoid condensation at low temperature, the crystal rod is placed inside a vacuum chamber pumped down to 10^{-7}~ 10^{-8} Torr with a turbo pump (V-81M) backed up by a scroll pump (Varian, Agilent Technology Inc.). The amplification operates in the gain saturation regime for energy stability. This provides ~18 mJ of uncompressed energy per pulse. We observe a small amount of spectral redshift in the amplification. This, in principle, can be improved by tilting the spectral flattening filter in the regenerative amplifier and slightly blue-shifting the seed pulse. After amplification, the pulse duration is compressed back to <30 fs in a grating-based compressor with 84% transmission efficiency. This provides ~0.5 TW peak power at 1 kHz.

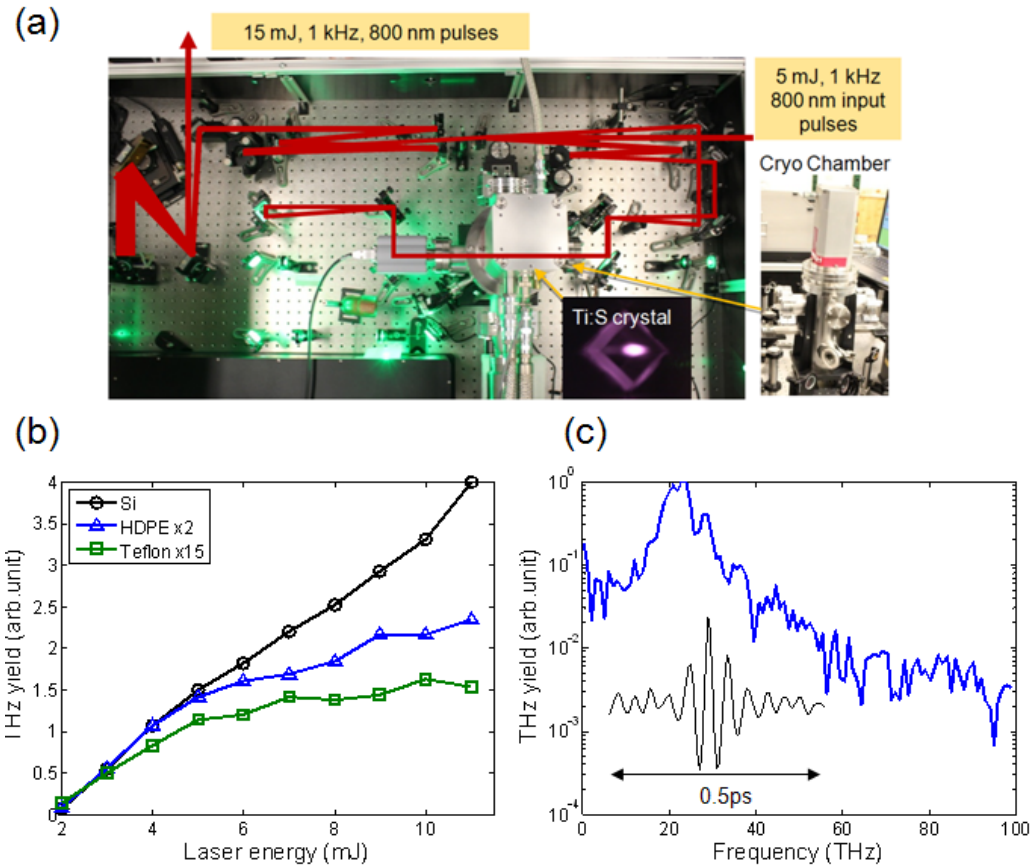

Figure 4.5 (a) Photography of a homebuilt cryogenically-cooled Ti:sapphire amplifier capable of producing 15 mJ, 30 fs, 800 nm pulses at a 1 kHz repetition rate for high average power THz generation. (b) Measured THz output energy as a function of input laser energy with three different filter sets. For clarity, the yields for HDPE and Teflon are multiplied by a factor of 2 and 15, respectively. The maximum THz energy is ~1 μJ/pulse at 1 kHz. (c) THz radiation spectrum measured by FTIR.

Using the cryogenic amplifier system, we have generated THz radiation via two-color filamentation in air and tested THz energy scaling. The input laser energy is varied with a combination of a half wave plate and a thin film polarizer. The THz pulse is collected and focused by a pair of off-axis parabolic mirrors into a pyroelectric detector (SPI-A-62THZ, Spectrum detector Inc.).

Figure 4.5(b) shows measured THz output energy with increasing laser input energy. Three THz filters are used for detection at different frequency regions. The three lines in Fig. 4.5(b) show that the majority of radiation occurs at high frequencies. Note that the Teflon signal is rescaled by 15 times for clarity. In addition, the low frequency radiation (<3 THz) saturates quickly whereas the high frequency signal (Si filter) continues to increase with increasing input energy up to ~11 mJ, providing THz energy of ~1 μJ/pulse.

Figure 4.5(c) shows a typical first-order interferometric field autocorrelation and the corresponding THz spectrum measured by Fourier transform infrared spectroscopy (FTIR) [48]. It shows radiation up to ~60 THz with input pulse duration of ~30 fs. Even broader bandwidth ranging up to >100 THz is reportedly achieved by using a shorter (<20 fs) pulse duration [30,82]. In our case, the majority of radiation occurs at high frequencies and peaks at 22 THz. This source is capable of providing 1 μJ/pulse, >60 THz pulses at 1 kHz and can be readily used for broadband nonlinear THz studies.

4.3.4 THz radiation profiles in long filamentation and refocusing

The previous section shows that high-energy THz radiation can be produced by an elongated filament which naturally forms a line source. Due to off-axis phase matching in filamentation, the line source emits conical THz radiation. In this section we discuss such radiation profiles and in particular the issue of refocusing conical radiation into a small spot size.

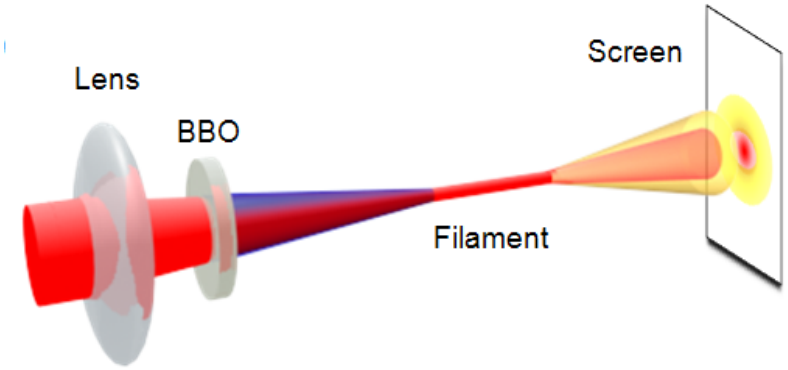

Figure 4.6 Experimental setup for measuring THz far-field radiation profiles. The pyroelectric detector (not shown) is raster scanned over 3.5 cm × 5 cm on a screen at ~20 cm away from the filament.

Figure 4.6 shows an experimental layout for measuring a THz radiation profile in the far field. With f = 1.5 m focusing with 5 mJ laser energy, a >7 cm long filament is produced. A pyroelectric detector mounted on a two-dimensional (2-D) motorized stage is raster scanned to measure the radiation profile. In addition, various THz transmission filters are placed to study high and low THz radiation profiles. The THz profile, obtained with a Teflon transmission filter, shows a donut-shaped structure. This off-axis radiation profile is attributed to the phase matching condition in long filamentation [52].

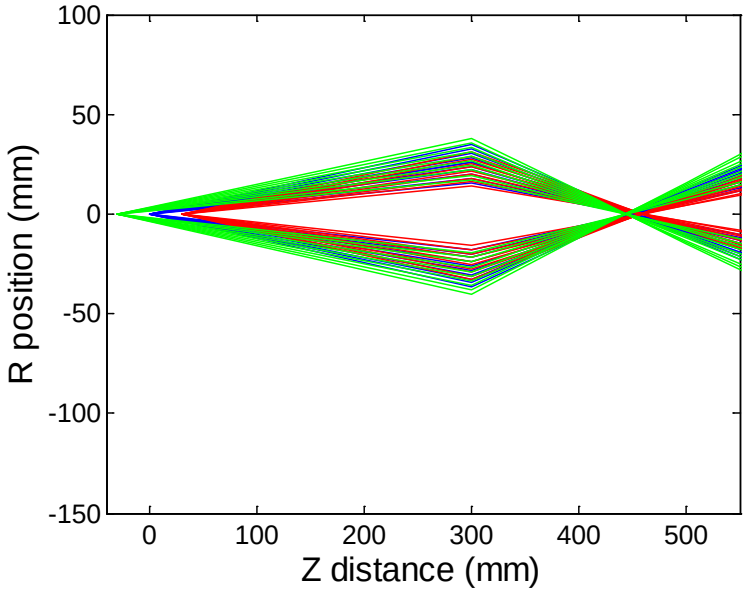

Figure 4.7 THz ray tracing calculation of a ~7 cm long filament source.

We also calculate and measure the profiles of THz radiation when refocused by a pair of parabolic mirrors. The measured minimum spot size is ~1.5 mm at 1~3 THz frequencies. Unlike the conical radiation before the focusing, the refocused THz intensity is peaked on axis. This transition can be explained by ray-tracing under geometric focusing as shown in Fig. 4.7. The refocused profile is bell-shaped, favorable for real applications, but the spot size inevitably increases with the filament length when the radiation from a line source is collected and focused by an off-axis parabolic mirror alone. In this case, the focused spot size scales as $D \sim l_f \cos^{-1}[1 - \Gamma/(2l_d)]$, where l_f is the filament length and Γ is the THz wavelength. For a ~7 cm long filament with $\Theta_p \sim 5^\circ$, the minimum spot size is calculated to be <1.5 mm, which agrees well with our measurements. This implies that THz energy

benefits from long filamentation but not for THz refocusing. Ultimately, this affects the THz field strength at the focus. However, this refocusing problem can be corrected by collimating the far field THz radiation with an axicon lens. More details are presented in chapter 6.

4.4 Conclusion

In chapter 4, we have discussed intense THz generation and its theoretical limit in two-color laser filamentation, with an emphasis on the macroscopic propagation effect. Experimentally, we have used three TW laser systems (0.5 TW, 2 TW, and 30 TW) to create a broad range of filament conditions. Our simulation and experimental results confirm scalable THz generation with increasing filament length.

With our 2 TW system, we have produced ~7 μJ of THz energy with a 15 cm long filament at 10 Hz. Further enhancement to 100 μJ can be achieved in 1.5-m long filamentation with using a 30 TW laser. This can provide multi-GW peak power with a 100 THz bandwidth. In terms of high average power, our kHz system can currently provide 1 mW with ~1 μJ/pulse. The focused field strength is >1 MV/cm but can be enhanced up to ~100 MV/cm with ionization in a gas cell and axicon-based beam collimation. Due to this broadband and high-field strength, two-color laser filamentation will be a very useful source for broadband THz spectroscopy and strong THz field studies.

Chapter 5 : Broadband THz radiation and detection

5.1 Introduction to THz detection

The advantage of THz generation in air plasma lies in not only the output power, but also its ultra-broad spectrum bandwidth. To detect such broadband radiation, various complementary methods must be applied. Therefore, in this chapter, we introduce and discuss broadband THz generation in two-color laser mixing in air and its various THz detection schemes including electro-optic sampling, Fourier transform infrared (FTIR) detection, and electric field induced second harmonic (EFISH) detection.

5.1.1 Electro-optic sampling

Electro-optic sampling (EOS) measures the electric field of THz radiation in the time domain using the Pockels effect in an electro-optic crystal. The Pockels effect, $P^{(2)}$, and field induced susceptibility, $\chi^{(2)}$ in the crystal are given by [7] [83],

$$P_j^{(2)}(\omega) = \sum_j \varepsilon_0 \chi_{ij}^{(2)}(\omega) \mathrm{E}_j(\omega) \tag{5.1}$$

$$\chi_{ij}^{(2)}(\omega) = \sum_k \chi_{ijk}^{(2)}(\omega, \omega, \Omega_{THz}) \mathrm{E}_k(\Omega_{THz}) \tag{5.2}$$

As one can see from eq. (5.2), the susceptibility is a function of an applied electric field. A greater THz electric field induces more birefringence in the nonlinear crystal, and thus the measured birefringence in the crystal can be converted into the THz field in the time domain [7].

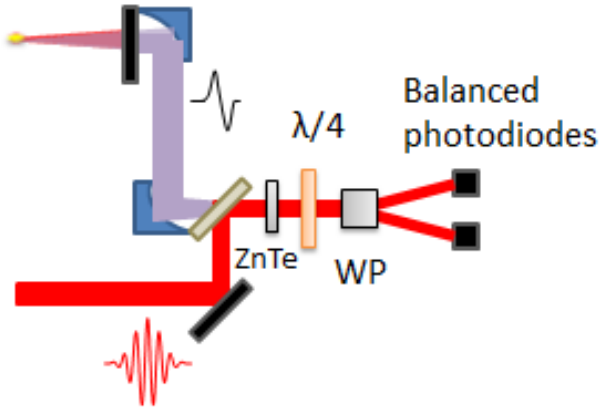

Figure 5.1 Two-color laser based THz generation and electro-optic sampling (EOS) detection. An optical pulse is focused onto a detection ZnTe crystal along with the THz pulse to be characterized. The probe pulse then goes through a quarter-wave plate (λ/4) and a Wollaston prism (WP) before being detected by balanced photodiodes.

Figure 5.1 shows a typical EOS detection scheme for THz field measurements in the time domain. A THz pulse produced in air-plasma is collimated and focused onto a detection crystal such as ZnTe, by two off-axis parabolic mirrors. When the THz pulse induces transient birefringence in the ZnTe crystal, a linearly polarized probe pulse undergoes a birefringent phase retardation in the crystal and its polarization changes into elliptical. The birefringent phase retardation in the nonlinear crystal is given by [7],

$$\Delta\phi = (n_x - n_y)\frac{\omega L}{c} = \frac{\omega L}{c} n_O^3 r_{41} E_{THz} \tag{5.3}$$

where n_o is the refractive index at optical wavelength and r_{41} is the EO coefficient (= 4 pm/V for ZnTe) [7]. After that, the elliptically polarized probe pulse passes through a quarter wave plate and Wollaston prism and then is detected by balanced photodiodes. The probe beam intensities measured by each photodiode are given by [7],

$$I_x = \frac{I_0}{2}(1-\Delta\phi) \qquad \text{and} \qquad I_y = \frac{I_0}{2}(1+\Delta\phi)\,. \tag{5.4}$$

Finally, the balanced intensity is shown as,

$$I_b = I_y - I_x = I_0 \Delta\phi \propto E_{THz} \tag{5.5}$$

As we can see from Eq (5.5), the measure of the balanced photodiodes, I_b, is proportional to the birefringent phase retardation induced by the THz field, and thus the signal provides the THz electric field (waveform) in the time domain [7] [84].

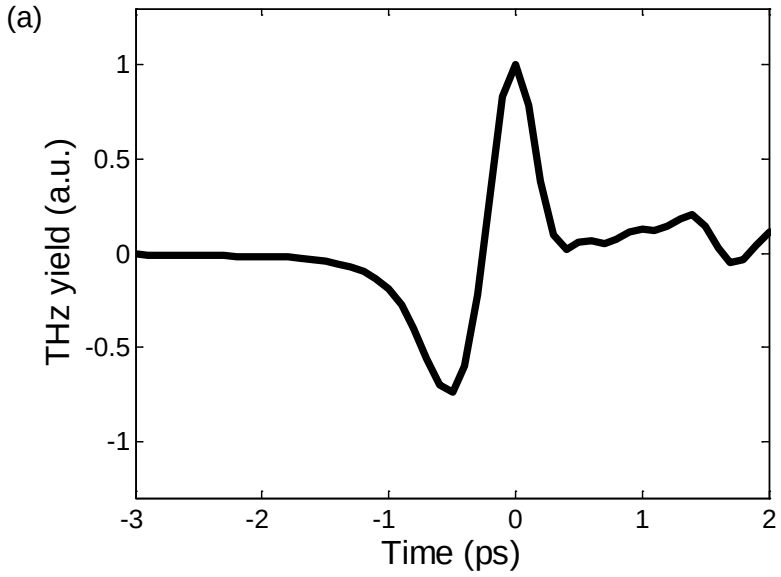

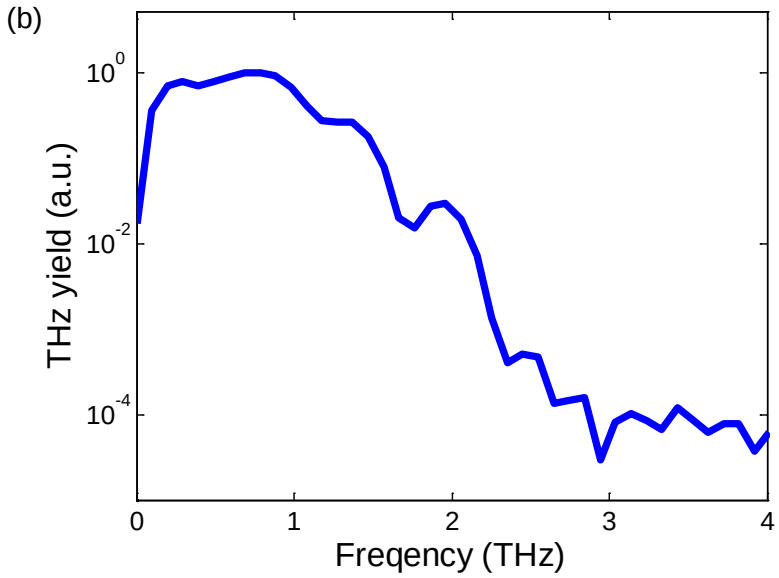

Figure 5.2 Experimental measurement with EOS detection in ZnTe. (a) THz yield in time and (b) Corresponding THz spectrum in a logarithmic scale.

Figure 5.2 shows a typical THz waveform by EOS with a 1 mm-thick ZnTe crystal. The corresponding spectrum is obtained by a post Fourier-transform. Here, the radiation bandwidth is limited to 3 THz but can be further increased by using a thinner and/or different EOS crystal having higher THz absorption lines, such as GaP.

5.1.2 Fourier transform infrared (FTIR) detection

Despite its straightforward setup, EOS covers limited spectrum bandwidth which is highly dependent on THz absorption and optical-THz velocity walk-off in the detection crystal. For instance, a 1 mm-thick ZnTe crystal provides up to 3 THz at

optical probing with 800 nm (see Fig. 5.2). This prevents us from utilizing the full spectral bandwidth that our source can generate.

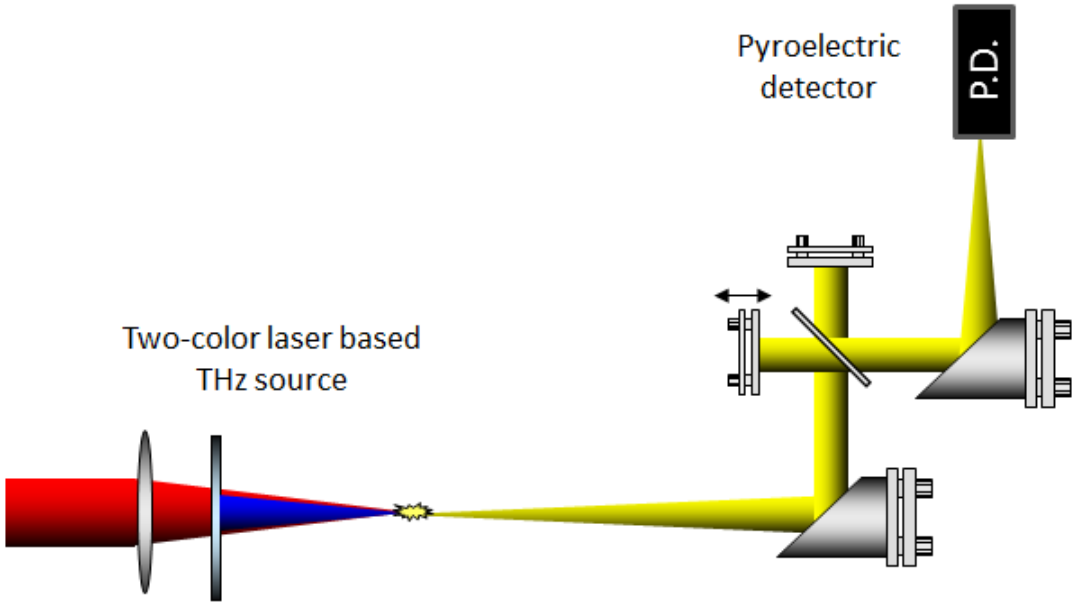

Figure 5.3 Two-color laser based THz generation and Michelson-type THz interferometery with Fourier transform infrared (FTIR) detection. The interference measured by a pyroelectric detector is Fourier transformed to retrieve the THz spectral information in the frequency domain.

For higher bandwidth detection, Michelson-type THz interferometery can be utilized for Fourier transform infrared spectroscopy (FTIR, see Fig. 5.3) [40] [48]. The THz pulses to be measured are split and recombined by a pellicle beamsplitter and then they interfere with a relative phase set by the optical path length difference between the two arms. The interference measured by a pyroelectric detector is Fourier transformed to frequency-domain for THz spectral intensity information (see Fig. 5.4). Although this FTIR does not directly provide THz waveforms, the detection

bandwidth is not limited by the optical probe duration as in the electric field induced second harmonic (EFISH) method which will be discussed in the next section. With FTIR our measurement in Fig. 5.4 shows THz radiation up to 60 THz.

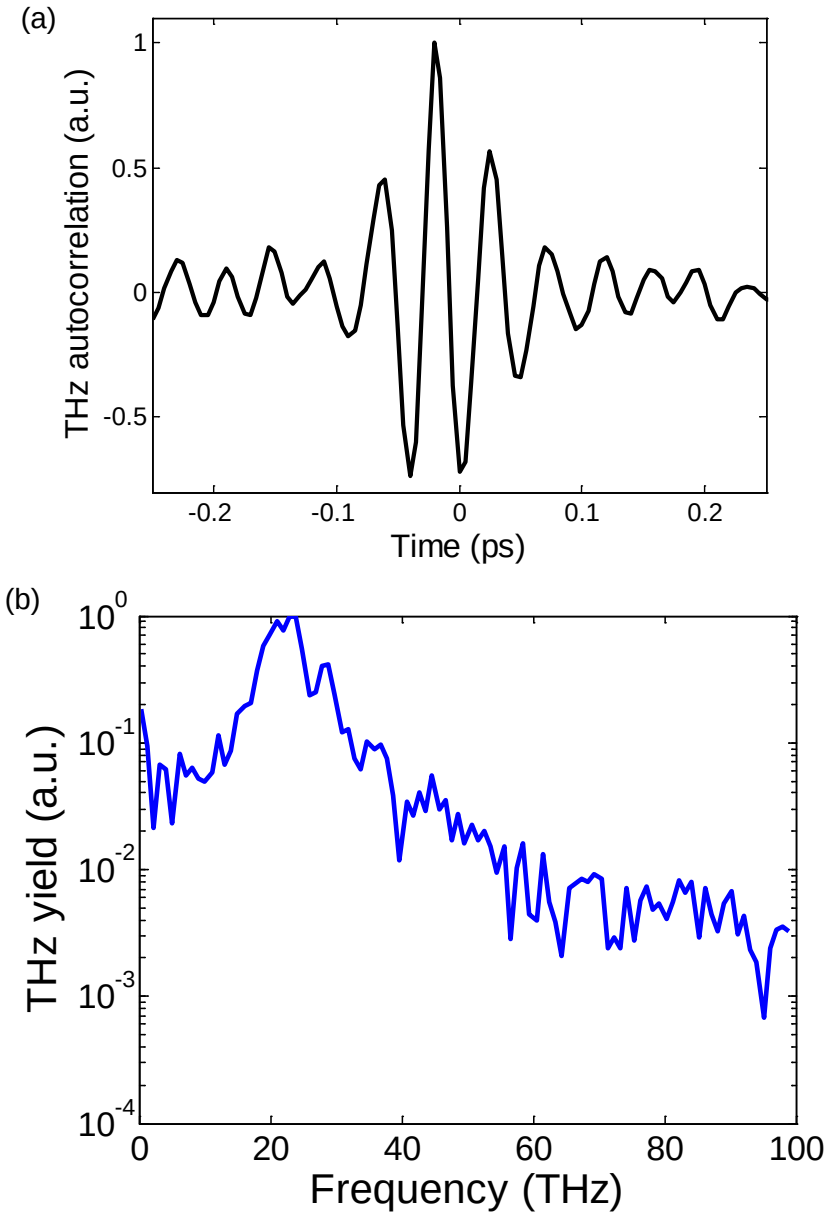

Figure 5.4 Experimental measurement of broadband THz detection. (a) THz autocorrelation in time and (b) the corresponding THz spectral intensity in a logarithmic scale.

5.1.3 Electric field induced second harmonic detection

One drawback of FTIR is that it does not provide the THz waveforms directly. Another method for broadband THz detection is using electric-field-induced second-harmonic (EFISH) generation, also known as air-biased-coherent-detection (ABCD) [45] [85]. In this scheme, the THz pulse to be measured is focused into air along with an ultrashort optical pulse, which produces an optical second harmonic of the incoming optical probe by the EFISH effect. It can be considered as the reverse process of THz generation by two-color mixing in air, i.e., the change in second harmonic yield is proportional to the THz electric field to be measured at the focus [45]. One big advantage of this technique is its capability of detecting THz waveforms directly (see Fig. 5.6).

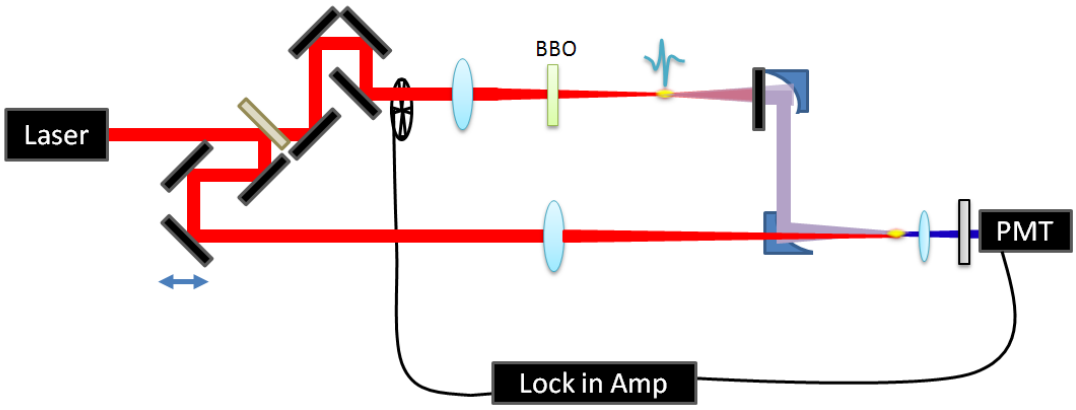

Figure 5.5 Two color laser based THz generation and electric-field-induced second-harmonic (EFISH) detection scheme. The induced second harmonic is measured by a photomultiplier tube (PMT).

Figure 5.5 shows a typical EFISH detection setup. The THz pulses produced in air-plasma are collimated and focused by two off-axis parabolic mirrors. Simultaneously, the probe laser pulses pass through a pinhole in the last off-axis parabolic mirror and co-focus with the THz pulses. At the focus, the THz field induces a second harmonic (400 nm) of the probe beam (800 nm). The induced second harmonic is detected by a photomultiplier tube (PMT) with narrow-band interference filters placed in front.

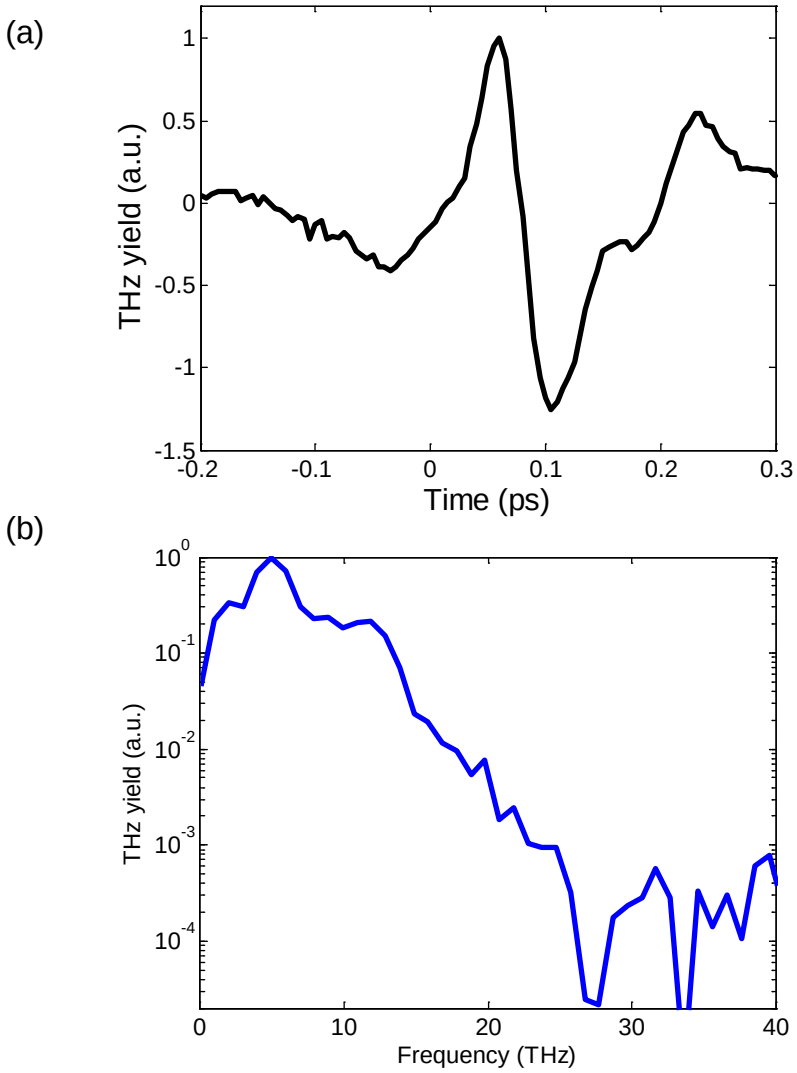

Figure 5.6 Experimental measurement of broadband THz detection via EFISH detection. (a) Measured THz waveform, and (b) the corresponding THz spectral intensity in a logarithmic scale.

Figure 5.6 shows experimental results for broadband THz radiation using EFISH. The detection bandwidth in this scheme is fundamentally limited by the probe pulse duration. We have measured THz radiation up to 30 THz, mainly limited by our stretched probe pulse width (> 30 fs) [86]. We note that Zhang *et al*. have reported THz detection up to 60 THz using much shorter laser pulses (< 20 fs) produced by

supercontinuum generation followed by hollow-fiber-based pulse compressor in 2011 [45].

5.2 Summary for Broadband THz detection

As we mentioned, two-color photoionization can generate EM radiation at an extremely broad range, covering from RF to extreme ultraviolets (EUVs). At first, an ultrafast photocurrent induced by two-color ionization creates EM radiation with a large bandwidth. Here the timescale for the current surge is much shorter than the laser pulse duration because tunneling ionization occurs mostly around the peak intensity. For a ~30 fs (FWHM) laser pulsewidth, for example, the total ionization duration can be as short as ~12 fs (FWHM). This supports EM radiation with a bandwidth of >80 THz. This radiation bandwidth is then further broadened and modulated by several mechanisms summarized in Fig. 5.7(a).

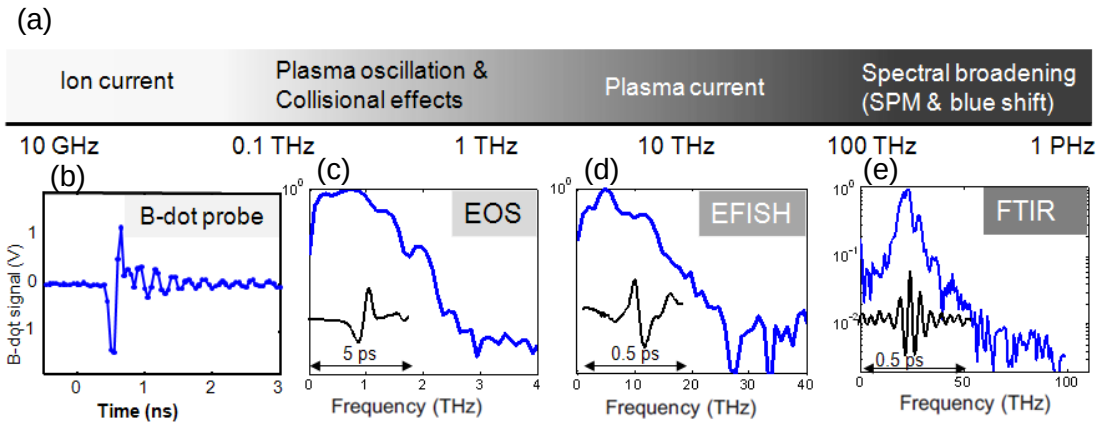

Figure 5.7 (a) Mechanisms for broadband electromagnetic radiation generation in two-color photoionization and radiation spectra measured

with the (b) B-dot probe, (c) EOS in ZnTe, (d) EFISH, and (e) FTIR techniques at broad frequency ranges.

The laser spectrum broadens with propagation due to self-phase modulation in air, ionization-induced blueshifts and self-steepening of femtosecond laser pulses [87]. The broadened laser spectrum increases the THz bandwidth even further. The spectrum at 0.1-1 THz is strongly modulated by plasma oscillation and collisional effects. In addition, the plasma density of 10^{16} - 10^{17} cm^{-3} strongly affects THz absorption in the filament direction. The collisional process ultimately terminates the plasma current. However, a very slow ion current can arise, producing radiation down to 0.01 THz. This corresponds to RF and microwaves. At the other frequency end, broadband EUVs can be produced by optical high harmonic generation (HHG). In particular, two-color based HHG can produce both odd and even harmonics, also enhancing the overall yields. This HHG is strongly connected with THz generation as they both arise from coherent motion of electrons in tunneling ionization [48,88].

To detect such broadband radiation, various complementary methods must be applied. Figures 5.7(b-e) show a list of our THz detection schemes along with measured radiation spectra. For example, the B-dot probe detects extremely low frequency components such as RF and microwaves (see Fig. 5.7(b)). For THz detection at 0.1-3 THz, electro-optic sampling (EOS) with a 1 mm-thick ZnTe crystal was adopted to measure THz waveforms (see Fig. 5.7(b)). For even higher bandwidth detection, EFISH and FTIR can be used and their results are shown in Figs. 5.7(d) and (e) respectively.

Chapter 6 : Summary and outlook for intense THz generation

6.1 Summary for high energy THz generation in two-color laser mixing

In this section, we summarize our work and discuss the outlook for high peak-power THz generation and theoretical limits in two-color laser filamentation.

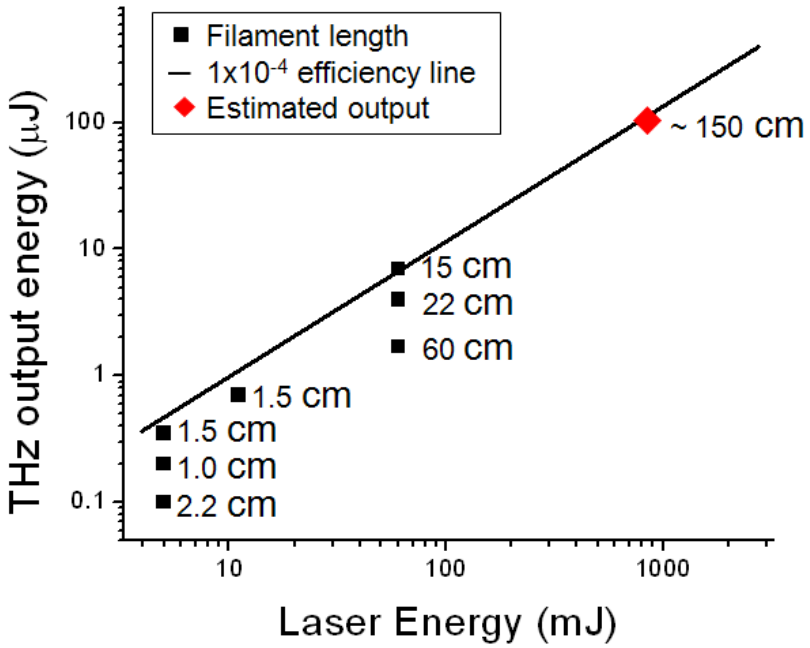

Figure 6.1 THz output energy as a function of input laser energy with various air filament lengths (black squares). The straight line represents maximum achievable THz energy with a conversion efficiency of 10^{-4}. A ~1.5 m long filament made with 1 J can theoretically yield ~100 μJ THz. The ultimate THz output energy is limited to ~300 μJ by the group velocity walk-off between two-color laser pulses. Here the fundamental laser wavelength is assumed to be 800 nm. We note that the optical to THz conversion efficiency can be further increased with longer wavelength (1~4 μm) pumping for filamentation [89].

Figure 6.1 summarizes THz energy scaling as a function of laser input energy. The black squares are our measurements obtained with various laser energy and filament length conditions. For a given energy value, there is a favorable filament length which yields the optimal THz conversion efficiency, 10^{-4}. This is represented as the straight line in Fig. 6.1. For instance, 10 mJ of laser input energy will yield ~1 μJ THz energy with an optimal filament length of ~2 cm, while 100 mJ of laser energy will require a >15 cm long filament to produce ~10 μJ THz energy. An input of 1 J energy, readily available with a 30 TW laser system, will yield 100 μJ of THz energy with an estimated filament length of ~1.5 m (red diamond in the figure). The corresponding peak power will approach multi-GW with a 100 THz bandwidth. The maximum achievable THz energy, however, is limited by the group velocity walk-off between two-color laser pulses. Due to air-plasma dispersion, two 50 fs pulses at 800 nm and 400 nm, for example, get separated in time as they propagate over ~4 m in air [52]. This effect limits production to ~300 μJ THz energy, a theoretical limit in two-color filamentation in air if the walk-off is not compensated.

6.2 Outlook for intense THz generation

Long filaments require a large parabolic mirror for THz energy collection. In addition, THz refocusing is another issue, as discussed in chapter 4. One possible method which can reduce the filament length while keeping the same high-energy THz output is to increase the plasma filament volume in the transverse direction. Focusing two-color laser pulses with a cylindrical lens can create a plasma sheet as

shown in Fig. 6.2(a). For a laser input of 1 J, a plasma sheet of ~1 cm^2 can be created. For THz collection and refocusing, a combination of a cylindrical mirror and a parabolic mirror can be used for tight focusing.

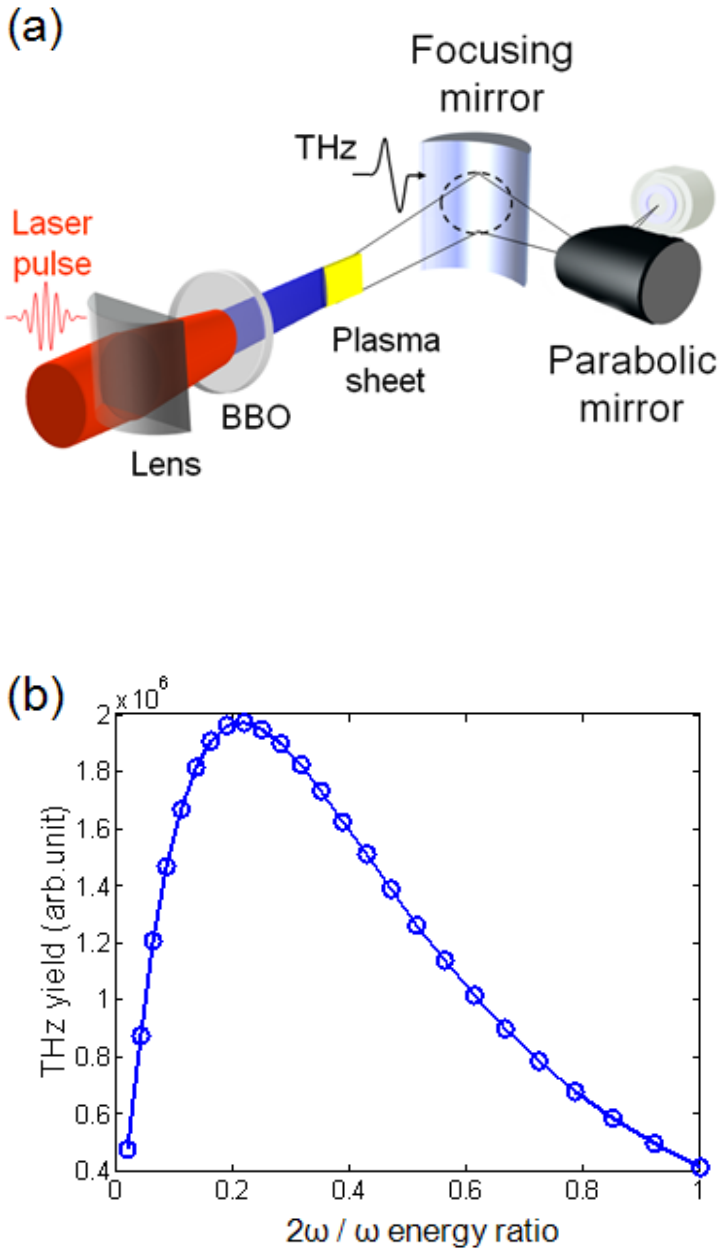

Figure 6.2 (a) Proposed experimental setup for scalable THz generation in a 2-D plasma sheet using cylindrical lens focusing and recollection. (b) Simulated THz output energy as a function of the energy ratio of 2ω to ω

with the total energy fixed. The output peaks at ratio ~0.2 according to the microscopic plasma current model [47].

For further THz energy scaling, the intensity of second harmonics needs to be increased. For example, Figure 6.2(b) shows a simulation result of THz output as a function of the ratio of the second harmonic intensity to the fundamental intensity, $I_{2\omega}/I_{\omega}$. According to the microscopic plasma current model, the output THz yield peaks at $I_{2\omega}/I_{\omega} \approx 20\%$ with $I_{2\omega} = 2 \times 10^{13}$ W/cm^2. In our experiments, the ratio is typically ~8%. This is partly because the frequency doubling crystal (BBO) is intentionally detuned from its optical angle. This scheme can be improved by using an ultrathin, dichroic half-waveplate right after the BBO crystal [46]. This allows us to optimize not only the efficiency in second harmonic generation with type-I phase matching but also the amplitude of plasma current at the focus with collinear two-color fields. Also the ultrathin thickness minimizes the two-color walk-off and pulse stretching. In addition, more efficient crystals such as BIBO [90] can be used to increase the conversion efficiency toward 20%.

Finally, a gas cell can be used for further THz enhancement. Previous results show that gases with low ionization potential such as krypton or xenon can dramatically increase THz output energy [39,48,74]. However, as those gases can easily saturate the output signal, it is important to increase the filament length accordingly. Combined with the ultrathin waveplate technique, this can increase the conversion efficiency toward 10^{-3}. For better refocusing, a conical lens (axicon) made of silicon or an axicon mirror can be used to collimate the conical THz emission.

Here we note that THz generation with axicon-based laser focusing was previously discussed [61,91], but our scheme proposes using an axicon for THz beam collimation only, not for laser beam focusing as in Ref. [61,91]. After collimation, a conventional off-axis parabolic mirror can be used for diffraction-limited refocusing. With our 1 kHz Ti:sapphire system capable of delivering 15 mJ/pulse, this gas cell method will produce 10 μJ/pulse at 1 kHz, corresponding to 10 mW average power, with a potential bandwidth of 100 THz. With an assumption of 100 fs THz pulse duration, the corresponding electric field at the focus will be 3 MV/cm with uncompensated refocusing (~1 mm diameter), while it will approach 100 MV/cm with diffraction-limited focusing (30 μm diameter). This source will be a very useful tool in high-power THz study including broadband nonlinear spectroscopy and imaging applications.

Appendix A : Cryogenic-cooled Ti:sapphire multi-pass amplifier

A.1 Introduction to our cryogenic-cooled amplifier

The laser system used in this dissertation is an amplified Ti:sapphire laser system. Consisting of a Kerr-lens mode-locking oscillator (Micra, Coherent Inc.) and a regenerative amplifier (Legend Elite USX, Coherent Inc.), our pre-existing system can deliver 800 nm central wavelength, 60 nm bandwidth (FWHM), >5 mJ, 25 fs pulses at a 1 kHz repetition rate (see Fig. A.1(a)). For even higher energy experiments, we have designed and built an additional cryogenically-cooled double-pass amplifier, which delivers 800 nm, 15 mJ, 30 fs pulses at a 1 kHz repetition rate. In this chapter, we describe its design and operation in detail.

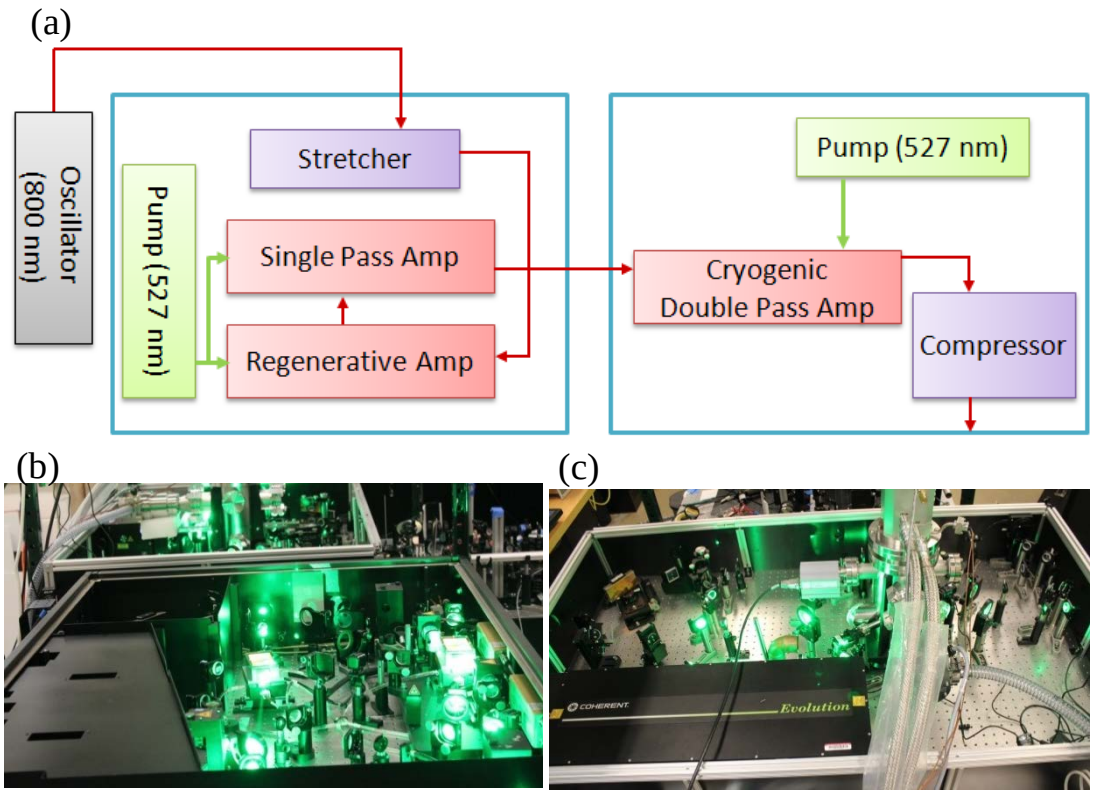

Figure A.1 (a) Diagram of our laser system consisting of an oscillator (Micra, Coherent Inc.), a regenerative amplifier (Legend USX, Coherent Inc.) and a cryogenic cooled double pass amplifier. Photography of our (b) regenerative amplifier and (c) double pass cryogenic amplifier.

Figure A.1 shows a systematic diagram of our amplified Ti:sapphire laser system. A seed laser pulse of 5 nJ and >80 nm (FWHM) from the oscillator is stretched to ~150 ps prior to amplification and injected into the regenerative and single-pass amplifiers, yielding 6 mJ and 60 nm (FWHM). Then the amplified pulse enters an external cryogenically-cooled amplifier achieving ~18 mJ and 50 nm (FWHM). The laser pulse is then compressed back to ~30 fs in a grating-based pulse compressor, and finally delivers 15 mJ and 50 nm (FWHM) at a 1 kHz repetition rate.

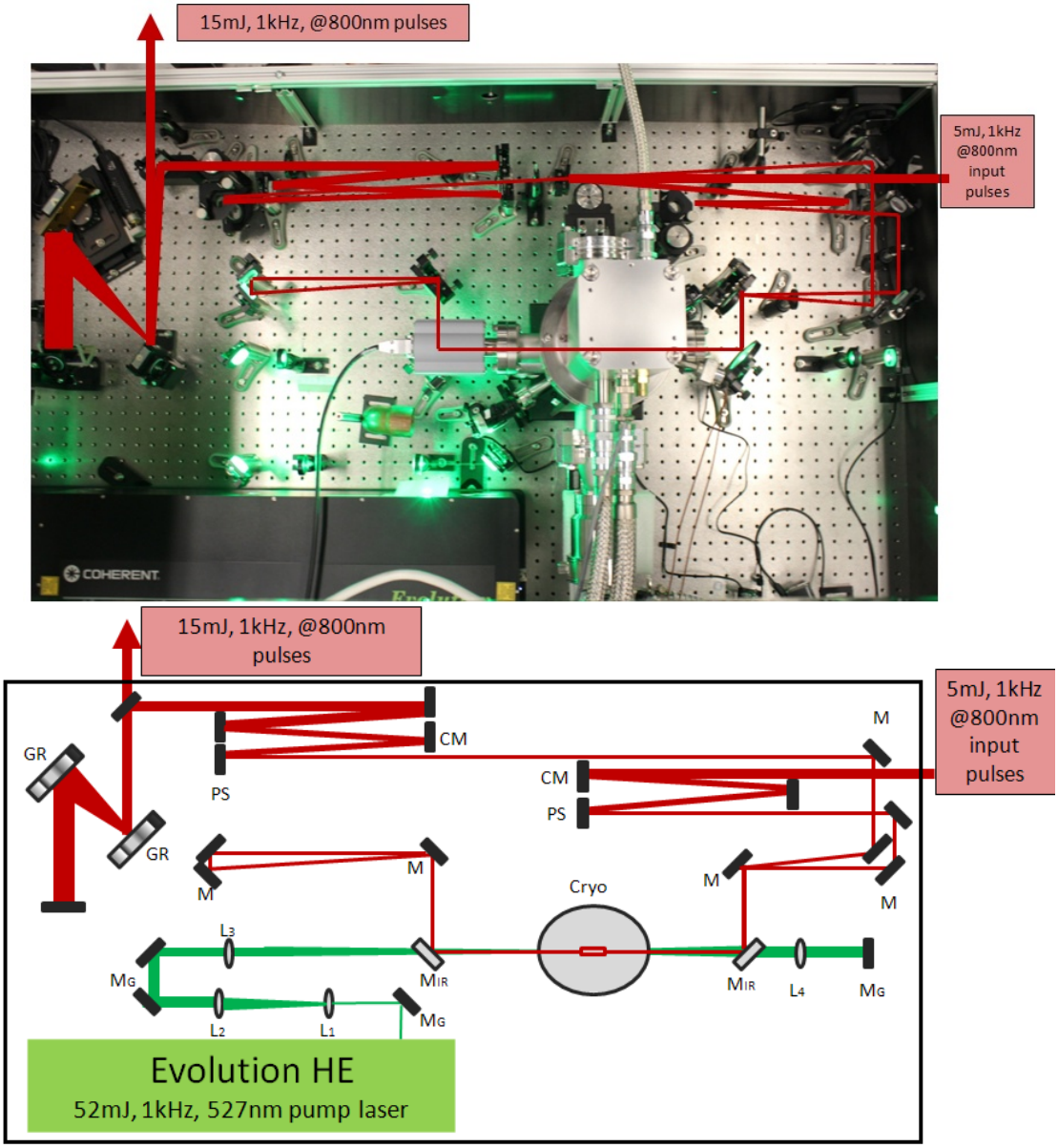

Figure A.2 Photography and optical layout of our cryogenically-cooled amplifier. The green line represents a pump laser beam (527 nm) and the red line represents a Ti:sapphire (800 nm) beam path.

Figure A.2 shows an optical path for the pump laser beam (527 nm) and amplified laser beam (800 nm) in the cryogenic laser system. The green line represents a pump laser beam (527 nm) path and the red line represents a Ti:sapphire (800 nm) beam path. The Ti:sapphire crystal in the amplifier is pumped by a frequency-doubled Nd:YLF laser (Evolution HE, Coherent Inc.), providing 45 mJ at

1 kHz repetition rate. The crystal is single-side pumped, while the transmitted pump energy is reflected back to the crystal for recycling. The amplification operates in the gain saturation regime for energy stability. The seed pulse is designed to pass through the gain medium twice to have the maximum gain efficiency (292% amplification).

A.2 Cryogenic cooling system

To minimize thermal lensing in the gain medium caused by unwanted residual heat from the high average power pumping, the Ti:sapphire crystal rod is cooled down to ~60 K with a cryogenic refrigerator (PT-90, Cryomech Inc.). The cryogenic refrigerator uses pure helium as a refrigerant gas in a closed-loop expansion cycle. Figure A.3 shows a photograph of the helium compressor.

Figure A.3 Cryomech helium compressor for cryogenic cooling.

Figure A.4 (a) Vacuum chamber in the cryogenic amplifier housing a Ti:sapphire crystal along with its cryorefrigerator head. (b) Cryorefrigerator and its cold head (Crymech Inc.) (c) Zoom-in picture of the cold head and 5 mm × 5 mm × 5.5 mm Ti:sapphire crystal.

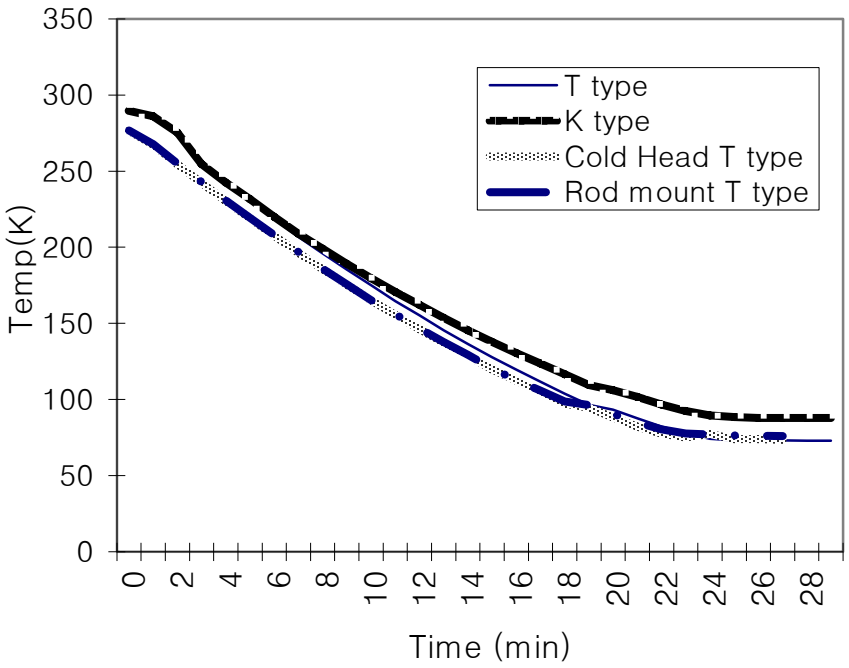

Figure A.5 Cold head and rod mount cooling measured with T and K type thermostat sensors as a function of time.

In order to avoid condensation at low temperature, the crystal rod is located inside a vacuum chamber (see Fig. A.4(a)) and pumped down to 10^{-7}~ 10^{-8} Torr with a turbo pump (V-81M, Agilent Technology Inc.) backed by a scroll pump (Varian, Agilent Technology Inc.). Figure A.4 shows a photo of Cryomech's cold head and a rod mount for the crystal in the vacuum chamber. The crystal rod is placed in between the two parts (upper and lower) of the rod mount along with indium sheets for good heat conductivity. Figure A.5 shows the temperature of the crystal rod as a function of time with cooling. The rod temperature drops to ~ 60 K, within 30 minutes.

A.3 Pump beam alignment and pulse delay setting

To achieve maximum gain in the cryogenic amplifier, the pump laser has to be synchronized with the seed pulses. To control the pulse delay between the pump and seed pulses, we use a delay generator (BNC 575, Berkeley Nucleonics Corp.) which synchronizes the pump laser in the cryogenic system (Evo 2) with the other pump laser in the regenerative amplifier system (Evo 1).

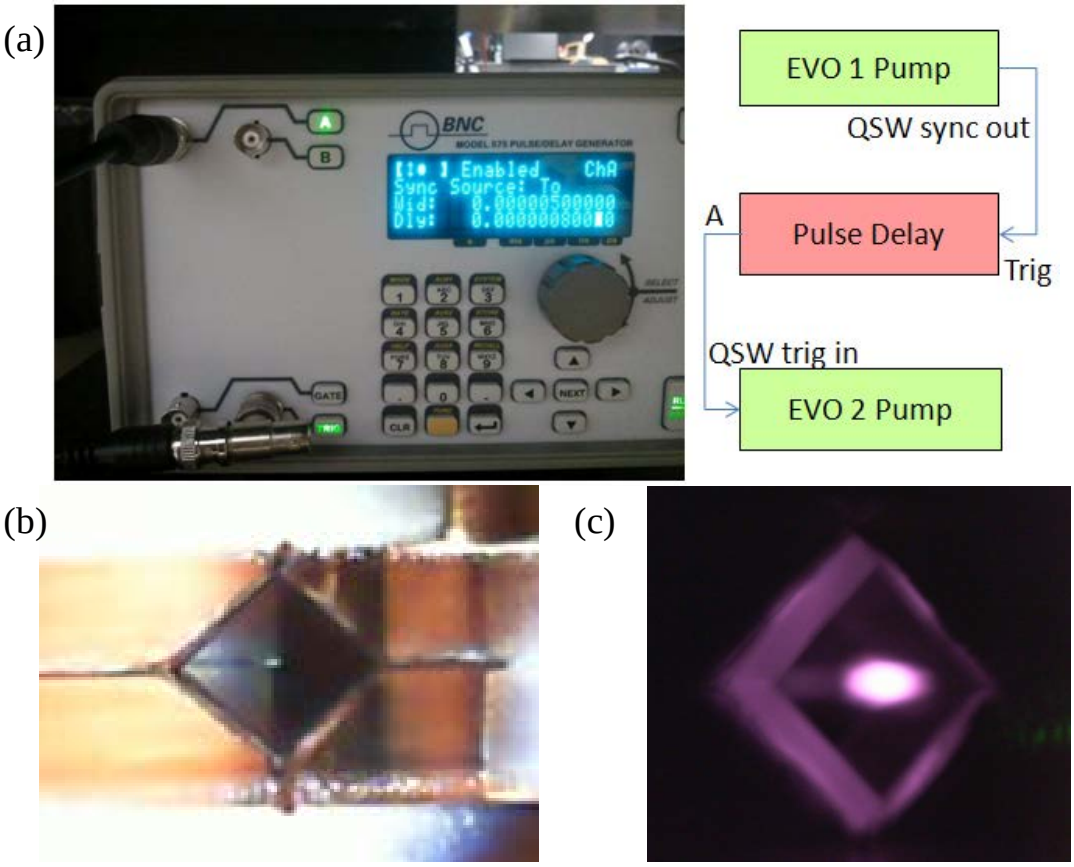

Figure A.6 (a) Delay generator and its connection diagram for synchronization between the pump and seed pulses. Ti:sapphire crystal (b) without and (c) with laser pumping.

Figure A.6 shows the delay generator and its connection diagram for synchronization. The desired setting for optimal pumping is as follows: trigger

(falling edge) and delay (800 ns with a width of 5000 ns). Figures A.6 (b-c) show a Ti:sapphire crystal without and with pumping.

A.4 Grating based pulse compressor

After amplification, the laser pulses are injected into a grating based compressor [3] [92]. Here, the pre-stretched pulses (18 mJ, ~150 ps) are compressed back to near its original pulse duration (15 mJ, 30 fs) with 84 % transmission efficiency.

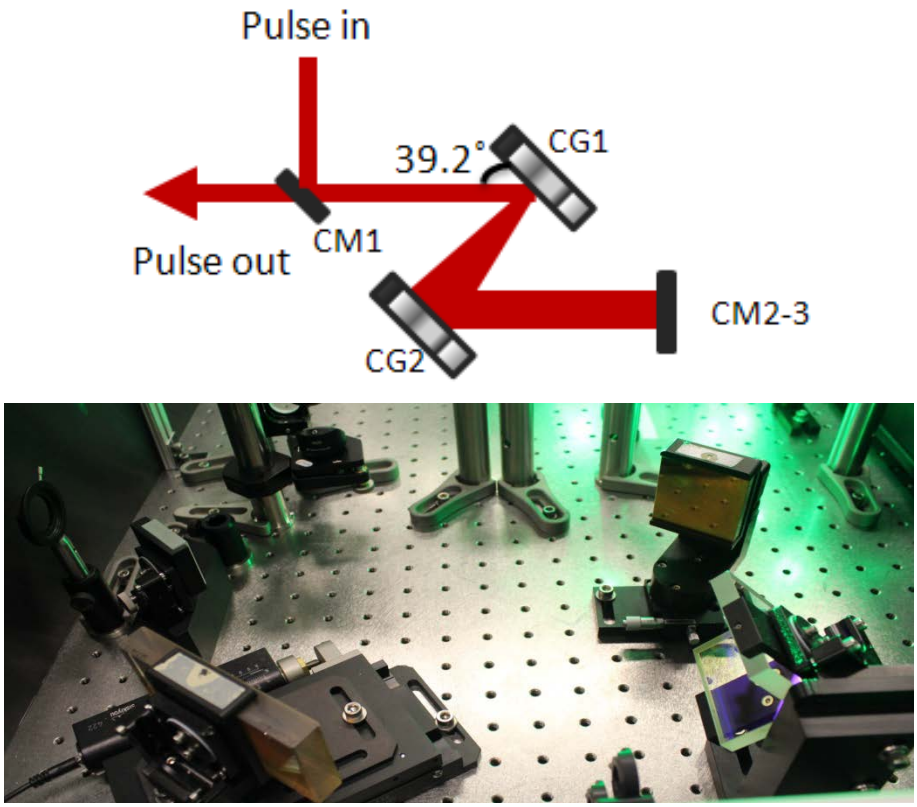

Figure A.7 Design and photography of a grating based compressor. The incident angle (φ_{in}) is 50.8 degrees. CG1 and CG2 are compressor gratings with 1500 g/mm.

A pulse from the oscillator is stretched into ~150 ps in the stretcher before being injected into the regenerative amplifier. In this pulse stretching, group delay dispersion (GDD) of ~2.13 × 10^6 fs^2 is added to the pulse given by [93],

$$\tau_{chirped} = \tau_{initial}(1+(4\ln 2\cdot(\frac{GDD}{\tau_{initial}^2}))^2)^{0.5}. \quad \text{(A.1)}$$

In addition, the Ti:sapphire crystal rod in the regenerative amplifier adds additional GDD of ~1441 fs^2 for a single pass. The pulse in the regenerative amplifier cavity undergoes 10 round trips, which results in ~28820 fs^2 overall. The Ti:sapphire rods in the single-pass and double-pass amplifiers add additional ~2391 fs^2. So the estimated total GDD is ~3.78 × 10^6 fs^2, and third-order dispersion (TOD) is ~5.88 × 10^8 fs^3

To compensate the accumulated GDD and TOD effectively, we calculated the grating separation length *L* using the following dispersion relationship, [55]

$$\phi''_{compressor} = -\frac{\lambda^3 L}{\pi c^2 d^2}\left[1-(\frac{\lambda}{d}-\sin\theta_{in})^2\right]^{-3/2}, \quad \text{(A.2)}$$

$$\phi'''_{compressor} = -\phi'''_{compressor}\frac{6\pi\lambda}{c}\frac{\left[1+\sin\theta_{in}(\frac{\lambda}{d}-\sin\theta_{in})\right]}{\left[1-(\frac{\lambda}{d}-\sin\theta_{in})^2\right]}, \quad \text{(A.3)}$$

where *L* is the perpendicular separation between the two parallel gratings, θ_{in} is the incident angle, and *d* is the grating groove spacing, and λ is the central wavelength (800 nm). The required double grating separation (*L*) is ~ 26.5 cm with an incident angle (φ_{in}) of 50.8° for our grating groove density of 1500 grooves/mm.

A.5 Output Beam measurement

Figure A.8(a) shows a cryogenic cooled amplifier beam profile prior to pulse compression. The beam size is measured to be 1.5 mm × 1.5 mm ($1/e^2$). Figure A.8(b) shows the final laser beam profile on a white screen located 1-m away from the final compressor.

(a)

(b)

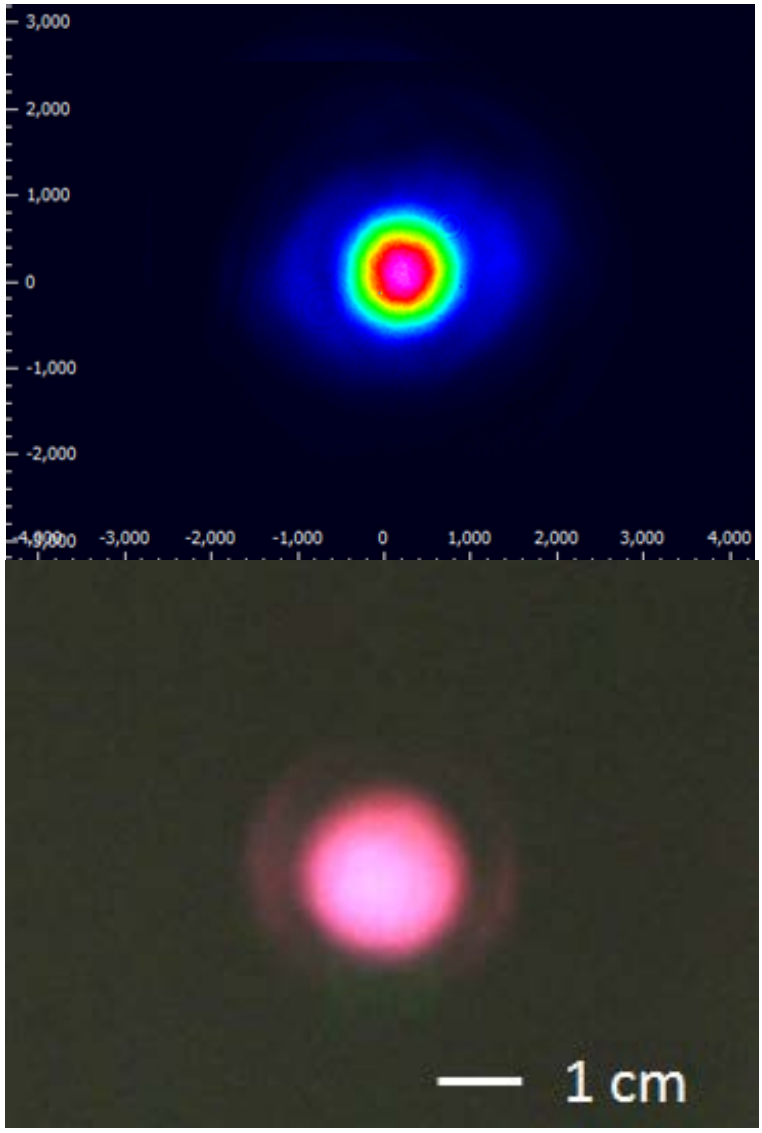

Figure A.8 Cryogenic amplifier beam profile (a) before expansion and (b) on a screen located 1-m away from the laser system.

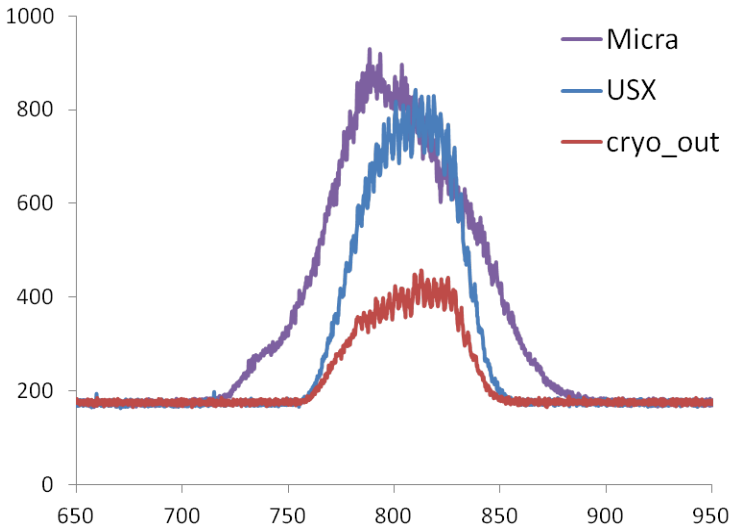

Figure A.9 Laser spectra after the oscillator (Micra), regenerative amplifier (Legend USX), and cryogenic amplifier.

Figure A.10 shows measured laser spectra after the oscillator, regenerative and cryogenic amplifiers. The center wavelength after the cryogenic amplifier is 807 nm (red-shifted) with a bandwidth of 55 nm. The small amount of spectral redshift, in principle, can be improved by tilting the spectral flattening filter in the regenerative amplifier and slightly blue-shifting the seed pulse. The pulse width is ~30 fs, measured with a single shot intensity autocorrelator. Thus, the system provides 15 mJ, 30 fs pulses at 1 kHz repetition rate with a peak laser power of ~0.5 TW.

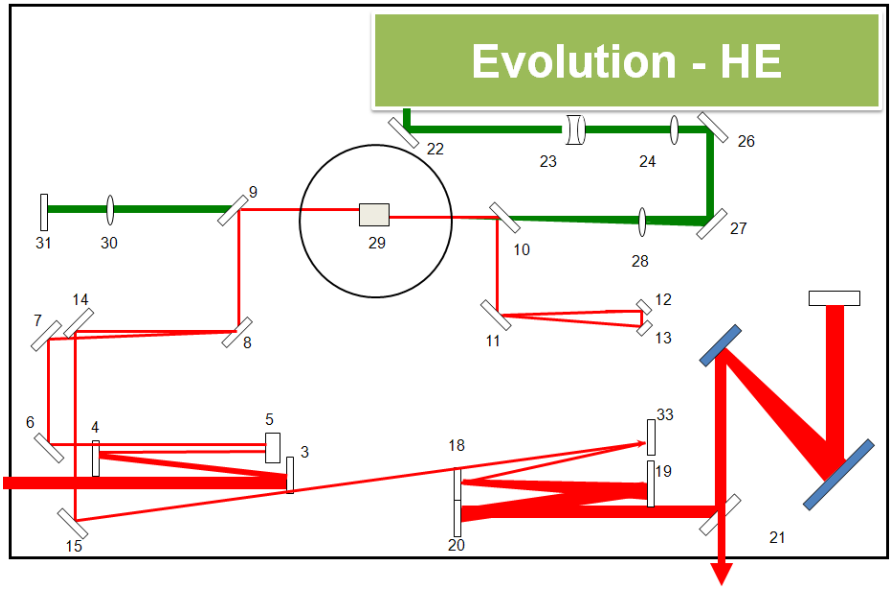

Figure A.10 Cryogenic-cooled double pass amplifier diagram

Table 1 Optical components for cryogenic cooled laser system

#	Optics
MA1	45 deg, HR 800nm P, 1.5" diam., flat
MA2	45 deg, HR 800nm P, 1.5" diam., flat
3	0 deg, HR 800nm P, 1.0" diam., f = + 500 concave
4	0 deg, HR 800nm P, 1.0" diam., f = - 75 convex
5	Periscope kit
6	45 deg, HR 800nm P, 1.0" diam., flat
7	45 deg, HR 800nm P, 1.0" diam., flat
8	45 deg, HR 800nm P, 1.5" diam., flat
9	45 deg, HR 800nm P, HT 527nm, 2.0" diam., flat
10	45 deg, HR 800nm P, HT 527nm, 2.0" diam., flat
11	45 deg, HR 800nm P, 1.5" diam., flat
12	45 deg, HR 800nm P, 1.0" diam., flat
13	45 deg, HR 800nm P, 1.0" diam., flat
14	45 deg, HR 800nm P, 1.0" diam., flat
15	45 deg, HR 800nm P, 1.0" diam., flat
18	0 deg, HR 800nm P, 1.0" diam., f = - 100 convex
19	0 deg, HR 800nm P, 2.0" diam., f = 500 concave
20	0 deg, HR 800nm P, 1.0" diam., flat
21	Grating Compressor
22	45 deg, HR 527nm P, 1.0" diam., flat
23	Concave lens, AR 527nm, 1.0" diam., f = -100 mm
24	Convex lens, AR 527nm, 1.0" diam., f = +250 mm
26	45 deg, HR 527nm P, 1.0" diam., flat
27	45 deg, HR 527nm P, 1.0" diam., flat
28	Convex lens, AR 527nm, 1.0" diam., f = +500 mm
29	Cryo vacuum chamber
30	Convex lens, AR 527nm, 1.0" diam., f = +350 mm
31	0 deg, HR 527nm P, 1.0" diam., flat
33	Periscope kit

Bibliography

1. T. H. Maiman, "Stimulated Optical Radiation in Ruby," Nature **187**, 493–494 (1960).
2. G. A. Mourou, C. P. J. Barry, and M. D. Perry, "Ultrahigh-Intensity Lasers: Physics of the Extreme on a Tabletop," Physics Today **51**, 22–28 (1998).
3. C. Rulliere, *Femtosecond Laser Pulses - Principles and Experiments, 2nd* ed. (Springer, USA, 2005)
4. P. F. Moulton, "Spectroscopic and laser characteristics of Ti:Al2O3," J. Opt. Soc. Am. B **3**, 125–133 (1986).
5. G. Overton,"Petawatts proliferate," Laser Focus World, 8, 2012. http://www.laserfocusworld.com/blogs/photon-focus/2012/08/petawatts-proliferate.html.
6. S. G. Ganichev and W. Prettl, *Intense Terahertz Excitation of Semiconductors* (Oxford University Press, USA, 2006).
7. Y.-S. Lee, *Principles of Terahertz Science and Technology,* 1st ed. (Springer, USA, 2008).
8. BR Labs, http://www.br-labs.com/divisions/terahertz/.
9. M. Tonouchi, "Cutting-edge terahertz technology," Nat. Photon **1**, 97–105 (2007).
10. D. Grischkowsky, S. Keiding, M. van Exter, and C. Fattinger, "Far-infrared time-domain spectroscopy with terahertz beams of dielectrics and semiconductors," J. Opt. Soc. Am. B **7**, 2006–2015 (1990).
11. B. Ferguson and X.-C. Zhang, "Materials for terahertz science and technology," Nature Materials **1**, 26–33 (2002).
12. B. B. Hu and M. C. Nuss, "Imaging with terahertz waves," Opt. Lett. **20**, 1716–1718 (1995).
13. K. Kawase, Y. Ogawa, Y. Watanabe, and H. Inoue, "Non-destructive terahertz imaging of illicit drugs using spectral fingerprints," Opt. Express **11**, 2549–2554 (2003).

14. J. B. Jackson, M. Mourou, J. F. Whitaker, I. N. Duling III, S. L. Williamson, M. Menu, and G. A. Mourou, “Terahertz imaging for non-destructive evaluation of mural paintings,” Opt. Comm. **281**, 527–532 (2008).
15. H. Hamster, A. Sullivan, S. Gordon, W. White, and R. W. Falcone, "Subpicosecond, electromagnetic pulses from intense laser-plasma interaction," Phys. Rev. Lett. **71**, 2725 (1993).
16. W. P. Leemans, C. G. R. Geddes, J. Faure, C. Tóth, J. Van Tilborg, C. B. Schroeder, E. Esarey, G. Fubiani, D. Auerbach, B. Marcelis, M. A. Carnahan, R. A. Kaindl, J. Byrd, and M. C. Martin, “Observation of terahertz emission from a laser-plasma accelerated electron bunch crossing a plasma-vacuum boundary.,” Phys. Rev. Lett. **91**, 074802 (2003).
17. J. Hebling, K.-L. Yeh, M. C. Hoffmann, B. Bartal, and K. A. Nelson, "Generation of high-power terahertz pulses by tilted-pulse-front excitation and their application possibilities," J. Opt. Soc. Am. B **25**, B6–B19 (2008).
18. M. C. Hoffmann, J. Hebling, H. Y. Hwang, K.-L. Yeh, and K. A. Nelson, "THz-pump/THz-probe spectroscopy of semiconductors at high field strengths [Invited]," J. Opt. Soc. Am. B **26**, A29–A34 (2009).
19. P. Gaal, K. Reimann, M. Woerner, T. Elsaesser, R. Hey, and K. H. Ploog, "Nonlinear Terahertz Response of n-Type GaAs," Phys. Rev. Lett. **96**, 187402 (2006).
20. Y. Shen, T. Watanabe, D. A. Arena, C.-C. Kao, J. B. Murphy, T. Y. Tsang, X. J. Wang, and G. L. Carr, "Nonlinear Cross-Phase Modulation with Intense Single-Cycle Terahertz Pulses," Phys. Rev. Lett. **99**, 043901 (2007).
21. J. Hebling, K.-L. Yeh, K. A. Nelson, and M. C. Hoffmann, "High-Power THz Generation, THz Nonlinear Optics, and THz Nonlinear Spectroscopy," IEEE Journal of Selected Topics in Quantum Electronics **14**, 345 –353 (2008).
22. M. C. Hoffmann, N. C. Brandt, H. Y. Hwang, K.-L. Yeh, and K. A. Nelson, "Terahertz Kerr effect," Appl. Phys. Lett. **95**, 231105 1–3 (2009).
23. G. L. Carr, M. C. Martin, W. R. McKinney, K. Jordan, G. R. Neil, and G. P. Williams, "High-power terahertz radiation from relativistic electrons," Nature **420**, 153–156 (2002).

24. D. You, R. R. Jones, P. H. Bucksbaum, and D. R. Dykaar, "Generation of high-power sub-single-cycle 500-fs electromagnetic pulses," Opt. Lett. **18**, 290–292 (1993).
25. X.-C. Zhang and J. Xu, *Introduction to THz Wave Photonics*, 1st ed. (Springer, 2009).
26. A. Dreyhaupt, S. Winnerl, T. Dekorsy, and M. Helm, "High-intensity terahertz radiation from a microstructured large-area photoconductor," Appl. Phys. Lett. **86**, 121114–121114–3 (2005).
27. M. Beck, H. Schäfer, G. Klatt, J. Demsar, S. Winnerl, M. Helm, and T. Dekorsy, "Impulsive terahertz radiation with high electric fields from an amplifier-driven large-area photoconductive antenna," Opt. Express **18**, 9251–9257 (2010).
28. S. L. Dexheimer, *Terahertz Spectroscopy: Principles and Applications*, 1st ed. (CRC Press, 2007).
29. J. A. Fülöp, L. Pálfalvi, S. Klingebiel, G. Almási, F. Krausz, S. Karsch, and J. Hebling, "Generation of sub-mJ terahertz pulses by optical rectification," Opt. Lett. **37**, 557–559 (2012).
30. E. Matsubara, M. Nagai, and M. Ashida, "Ultrabroadband coherent electric field from far infrared to 200 THz using air plasma induced by 10 fs pulses," Appl. Phys. Lett. **101**, 011105 1–4 (2012).
31. D. J. Cook and R. M. Hochstrasser, "Intense terahertz pulses by four-wave rectification in air," Opt. Lett. **25**, 1210–1212 (2000).
32. T. Bartel, P. Gaal, K. Reimann, M. Woerner, and T. Elsaesser, "Generation of single-cycle THz transients with high electric-field amplitudes," Opt. Lett. **30**, 2805–2807 (2005).
33. M. Kresz, T. Loffler, M. D. Thomson, R. Dorner, H. Gimpel, K. Zrost, T. Ergler, R. Moshammer, U. Morgner, J. Ullrich, and H. G. Roskos, "Determination of the carrier-envelope phase of few-cycle laser pulses with terahertz-emission spectroscopy," Nat Phys **2**, 327–331 (2006).
34. M. Kress, T. Löffler, S. Eden, M. Thomson, and H. G. Roskos, "Terahertz-pulse generation by photoionization of air with laser pulses composed of both fundamental and second-harmonic waves," Opt. Lett. **29**, 1120–1122 (2004).

35. X. Xie, J. Dai, and X.-C. Zhang, "Coherent Control of THz Wave Generation in Ambient Air," Phys. Rev. Lett. **96**, 075005 (2006).
36. Y. Chen, M. Yamaguchi, M. Wang, and X.-C. Zhang, "Terahertz pulse generation from noble gases," Appl. Phys. Lett. **91**, 251116 1–3 (2007).
37. J. Dai, N. Karpowicz, and X.-C. Zhang, "Coherent Polarization Control of Terahertz Waves Generated from Two-Color Laser-Induced Gas Plasma," Phys. Rev. Lett. **103**, 023001 (2009).
38. H. Wen and A. M. Lindenberg, "Coherent Terahertz Polarization Control through Manipulation of Electron Trajectories," Phys. Rev. Lett. **103**, 023902 (2009).
39. F. Blanchard, G. Sharma, X. Ropagnol, L. Razzari, R. Morandotti, and T. Ozaki, "Improved terahertz two-color plasma sources pumped by high intensity laser beam," Opt. Express **17**, 6044–6052 (2009).
40. G. Rodriguez and G. L. Dakovski, "Scaling behavior of ultrafast two-color terahertz generation in plasma gas targets: energy and pressure dependence," Opt. Express **18**, 15130–15143 (2010).
41. T.-J. Wang, J.-F. Daigle, Y. Chen, C. Marceau, F. Théberge, M. Châteauneuf, J. Dubois, and S. l. Chin, "High energy THz generation from meter-long two-color filaments in air," Laser Phys. Lett. **7**, 517–521 (2010).
42. T.-J. Wang, C. Marceau, S. Yuan, Y. Chen, Q. Wang, F. Théberge, M. Châteauneuf, J. Dubois, and S. l. Chin, "External focusing effect on terahertz emission from a two-color femtosecond laser-induced filament in air," Laser Phys. Lett. **8**, 57–61 (2011).
43. F. Blanchard, G. Sharma, L. Razzari, X. Ropagnol, H.-C. Bandulet, F. Vidal, R. Morandotti, J.-C. Kieffer, T. Ozaki, H. Tiedje, H. Haugen, M. Reid, and F. Hegmann, "Generation of Intense Terahertz Radiation via Optical Methods," IEEE Journal of Selected Topics in Quantum Electronics **17**, 5–16 (2011).
44. M. C. Hoffmann and J. A. Fülöp, "Intense ultrashort terahertz pulses: generation and applications," Journal of Physics D: Applied Physics **44**, 083001 (2011).

45. Jianming Dai, B. Clough, I-Chen Ho, Xiaofei Lu, Jingle Liu, and Xi-Cheng Zhang, "Recent Progresses in Terahertz Wave Air Photonics," IEEE Transactions on Terahertz Science and Technology **1**, 274–281 (2011).
46. Y. Minami, T. Kurihara, K. Yamaguchi, M. Nakajima, and T. Suemoto, "High-power THz wave generation in plasma induced by polarization adjusted two-color laser pulses," Appl. Phys. Lett. **102**, 041105–1–4 (2013).
47. K.-Y. Kim, J. H. Glownia, A. J. Taylor, and G. Rodriguez, "Terahertz emission from ultrafast ionizing air in symmetry-broken laser fields," Opt. Express **15**, 4577–4584 (2007).
48. K.-Y. Kim, A. J. Taylor, J. H. Glownia, and G. Rodriguez, "Coherent control of terahertz supercontinuum generation in ultrafast laser-gas interactions," Nat Photon **2**, 605–609 (2008).
49. K.-Y. Kim, "Generation of coherent terahertz radiation in ultrafast laser-gas interactions," Phys. Plasmas **16**, 056706 (2009).
50. K.-Y. Kim, J. H. Glownia, A. J. Taylor, and G. Rodriguez, "High-Power Broadband Terahertz Generation via Two-Color Photoionization in Gases," IEEE Journal of Quantum Electronics **48**, 797 –805 (2012).
51. T. I. Oh, Y. S. You, and K. Y. Kim, "Two-dimensional plasma current and optimized terahertz generation in two-color photoionization," Opt. Express **20**, 19778–19786 (2012).
52. Y. S. You, T. I. Oh, and K. Y. Kim, "Off-Axis Phase-Matched Terahertz Emission from Two-Color Laser-Induced Plasma Filaments," Phys. Rev. Lett. **109**, 183902 (2012).
53. Y. S. You, T. I. Oh, and K.-Y. Kim, "Mechanism of elliptically polarized terahertz generation in two-color laser filamentation," Opt. Lett. **38**, 1034–1036 (2013).
54. T. I. Oh, Y. S. You, and K.-Y. Kim, “Scaling and Saturation of High-Power Terahertz Radiation Generation in Two-Color Laser Filamentation,” Appl. Phys. Lett. **102,** 201113 (2013).

55. K.-Y. Kim, Ph.D. Dissertation, “Measurement of ultrafast dynamics in the interaction of intense laser pulses with gases, atomic clusters, and plasmas,” University of Maryland (2003).
56. M. V. Ammosov, N. B. Delone, and V. P. Kraĭnov, "Tunnel ionization of complex atoms and of atomic ions in an alternating electromagnetic field," Soviet Physics - JETP **64**, 1191–1194 (1986).
57. V. S. Popov, "Tunnel and multiphoton ionization of atoms and ions in a strong laser field (Keldysh theory)," Phys.-Usp. **47**, 855 (2004).
58. L. D. Landau and L. M. Lifshitz, *Quantum Mechanics Non-Relativistic Theory, Third Edition: Volume 3*, 3rd ed. (Butterworth-Heinemann, 1981).
59. G. Rodriguez, A. R. Valenzuela, B. Yellampalle, M. J. Schmitt, and K.-Y. Kim, "In-line holographic imaging and electron density extraction of ultrafast ionized air filaments," J. Opt. Soc. Am. B **25**, 1988–1997 (2008).
60. X. Lu and X.-C. Zhang, "Generation of Elliptically Polarized Terahertz Waves from Laser-Induced Plasma with Double Helix Electrodes," Phys. Rev. Lett. **108**, 123903 (2012).
61. V. B. Gildenburg and N. V. Vvedenskii, "Optical-to-THz Wave Conversion via Excitation of Plasma Oscillations in the Tunneling-Ionization Process," Phys. Rev. Lett. **98**, 245002 (2007).
62. T.-J. Wang, Y. Chen, C. Marceau, F. Théberge, M. Chateauneuf, J. Dubois, and S. L. Chin, “High energy terahertz emission from two-color laser-induced filamentation in air with pump pulse duration control,” Appl. Phys. Lett. **95**, 131108 (2009).
63. A. A. Silaev and N. V. Vvedenskii, "Residual-Current Excitation in Plasmas Produced by Few-Cycle Laser Pulses," Phys. Rev. Lett. **102**, 115005 (2009).
64. A. Couairon and A. Mysyrowicz, "Femtosecond filamentation in transparent media," Physics Reports **441**, 47–189 (2007).
65. S. L. Chin, T.-J. Wang, C. Marceau, J. Wu, J. S. Liu, O. Kosareva, N. Panov, Y. P. Chen, J.-F. Daigle, S. Yuan, A. Azarm, W. W. Liu, T. Seideman, H. P. Zeng, M. Richardson, R. Li, and Z. Z. Xu, "Advances in intense femtosecond laser filamentation in air," Laser Phys. **22**, 1–53 (2012).

66. L. Bergé, S. Skupin, R. Nuter, J. Kasparian, and J.-P. Wolf, "Ultrashort filaments of light in weakly ionized, optically transparent media," Rep. Prog. Phys. **71**, 109801 (2008).
67. S. A. Hosseini, B. Ferland, and S. L. Chin, “Measurement of filament length generated by an intense femtosecond laser pulse using electromagnetic radiation detection,” Appl. Phys. B **76**, 583–586 (2003).
68. S. L. Chin, F. Théberge, and W. Liu, "Filamentation nonlinear optics," Appl. Phys. B **86**, 477–483 (2007).
69. F. Théberge, W. Liu, P. T. Simard, A. Becker, and S. L. Chin, "Plasma density inside a femtosecond laser filament in air: strong dependence on external focusing," Phys Rev E Stat Nonlin Soft Matter Phys **74**, 036406 (2006).
70. J. K. Wahlstrand, Y.-H. Cheng, and H. M. Milchberg, “Absolute measurement of the transient optical nonlinearity in N_2, O_2, N_2O, and Ar,” Phys. Rev. A **85**, (2012).
71. K.-L. Yeh, M. C. Hoffmann, J. Hebling, and K. A. Nelson, "Generation of 10 μJ ultrashort terahertz pulses by optical rectification," Appl. Phys. Lett. **90**, 171121 1–3 (2007).
72. F. Blanchard, L. Razzari, H. C. Bandulet, G. Sharma, R. Morandotti, J. C. Kieffer, T. Ozaki, M. Reid, H. F. Tiedje, H. K. Haugen, and F. A. Hegmann, "Generation of 1.5 μJ single-cycle terahertz pulses by optical rectification from a large aperture ZnTe crystal," Opt. Express **15**, 13212–13220 (2007).
73. A. G. Stepanov, L. Bonacina, S. V. Chekalin, and J.-P. Wolf, "Generation of 30 μJ single-cycle terahertz pulses at 100 Hz repetition rate by optical rectification," Opt. Lett. **33**, 2497–2499 (2008).
74. H. Zhong, N. Karpowicz, and X.-C. Zhang, "Terahertz emission profile from laser-induced air plasma," Appl. Phys. Lett. **88**, 261103 1–3 (2006).
75. L. Bergé, S. Skupin, C. Köhler, I. Babushkin, and J. Herrmann, "3D Numerical Simulations of THz Generation by Two-Color Laser Filaments," Phys. Rev. Lett. **110**, 073901 (2013).

76. C. D'Amico, A. Houard, M. Franco, B. Prade, A. Mysyrowicz, A. Couairon, and V. T. Tikhonchuk, "Conical Forward THz Emission from Femtosecond-Laser-Beam Filamentation in Air," Phys. Rev. Lett. **98**, 235002 (2007).
77. I. Babushkin, S. Skupin, A. Husakou, C. Köhler, E. Cabrera-Granado, L. Bergé, and J. Herrmann, "Tailoring THz radiation by controlling tunnel photoionization events in gases," New J. Phys. **13** 123029 (2011).
78. B. Edlén, "The Refractive Index of Air," Metrologia **2**, 71–80 (1966).
79. C. Köhler, E. Cabrera-Granado, I. Babushkin, L. Bergé, J. Herrmann, and S. Skupin, "Directionality of terahertz emission from photoinduced gas plasmas," Opt. Lett. **36**, 3166–3168 (2011).
80. Y.-H. Chen, S. Varma, T. M. Antonsen, and H. M. Milchberg, "Direct Measurement of the Electron Density of Extended Femtosecond Laser Pulse-Induced Filaments," Phys. Rev. Lett. **105**, 215005 (2010).
81. K. Y. Kim, V. Kumarappan, and H. M. Milchberg, "Measurement of the average size and density of clusters in a gas jet," Appl. Phys. Lett. **83**, 3210–3212 (2003).
82. M. D. Thomson, V. Blank, and H. G. Roskos, "Terahertz white-light pulses from an air plasma photo-induced by incommensurate two-color optical fields," Opt. Express **18**, 23173 (2010).
83. R. W. Boyd, *Nonlinear Optics, Third Edition*, 3rd ed. (Academic Press, 2008).
84. Q. Wu and X.-C. Zhang, "Free-space electro-optic sampling of terahertz beams," Appl. Phys. Lett. **67**, 3523–3525 (1995).
85. J. Dai, X. Xie, and X.-C. Zhang, "Detection of Broadband Terahertz Waves with a Laser-Induced Plasma in Gases," Phys. Rev. Lett. **97**, 103903 (2006).
86. I.-C. Ho, X. Guo, and X.-C. Zhang, "Design and performance of reflective terahertz air-biased-coherent-detection for time-domain spectroscopy," Opt Express **18**, 2872–2883 (2010).
87. J. P. Palastro, T. M. Antonsen, and H. M. Milchberg, "Compression, spectral broadening, and collimation in multiple, femtosecond pulse filamentation in atmosphere," Phys. Rev. A **86**, 033834 (2012).

88. D. Zhang, Z. Lü, C. Meng, X. Du, Z. Zhou, Z. Zhao, and J. Yuan, "Synchronizing Terahertz Wave Generation with Attosecond Bursts," Phys. Rev. Lett. **109**, 243002 (2012).
89. W.-M. Wang, S. Kawata, Z.-M. Sheng, Y.-T. Li, L.-M. Chen, L.-J. Qian, and J. Zhang, "Efficient terahertz emission by mid-infrared laser pulses from gas targets," Opt. Lett. **36**, 2608–2610 (2011).
90. T. Harimoto, Y. Takeuchi, and M. Fujita, "Spectral properties of second-harmonic generation at 800 nm in a BiB3O6 crystal," Opt. Express **12**, 811–816 (2004).
91. J.-M. Manceau, A. Averchi, F. Bonaretti, D. Faccio, P. Di Trapani, A. Couairon, and S. Tzortzakis, "Terahertz pulse emission optimization from tailored femtosecond laser pulse filamentation in air," Opt. Lett. **34**, 2165–2167 (2009).
92. J.-C. Diels and W. Rudolph, *Ultrashort Laser Pulse Phenomena, Second Edition*, 2nd ed. (Academic Press, 2006).
93. R. Paschotta, *Encyclopedia of Laser Physics and Technology*, 1st ed. (Wiley-VCH, 2008).